FIRST-PRINCIPLES STUDY OF HYDROGEN EVOLUTION REACTION MECHANISMS IN WEYL SEMIMETALS

LAU TING WAI

PhD

The Hong Kong Polytechnic University

2025

The Hong Kong Polytechnic University

Department of Applied Physics

First-Principles Study of Hydrogen Evolution Reaction Mechanisms in Weyl Semimetals

LAU Ting Wai

A thesis submitted in partial fulfilment of the requirements

for the degree of Doctor of Philosophy

July 2025

Certificate of originality

I hereby declare that this thesis is my own work and that, to the best of my knowledge and belief, it reproduces no material previously published or written, nor material that has been accepted for the award of any other degree or diploma, except where due acknowledgement has been made in the text.

_____(Signed)

LAU, Ting Wai (Name of student)

Abstract

Hydrogen evolution reaction (HER) is a key electrochemical process that extracts hydrogen from a solvent, serving as a crucial pathway for renewable energy generation. Noble metals like platinum and palladium are currently the most efficient catalysts for HER. However, their high cost and scarcity pose significant challenges to large-scale commercial applications. Therefore, developing alternative catalysts with high HER performance and lower cost is essential for advancing efficient hydrogen production technologies. Topological semimetals, particularly Weyl semimetals, have emerged as promising candidates for HER catalysis due to their robust electronic surface states, which are protected by their topological features in momentum space. Despite this potential, the direct relationship between HER performance and these unique surface states remains unclear. In this thesis, density functional theory (DFT) is employed to systematically investigate the HER activity of Weyl semimetals across multiple facets. Four critical descriptors – Gibbs free energy change of hydrogen adsorption, energy barriers for water dissociation, water adsorption energy, and surface energy – are analyzed to provide a more comprehensive evaluation of catalytic performance. The findings reveal that while topological surface states indeed influence HER efficiency, the number of Fermi arcs has mini-

mal impact. Moreover, although Gibbs free energy change of hydrogen adsorption is highly correlated with HER performance, the underlying mechanisms governing the interaction between catalyst intrinsic properties and hydrogen adsorption remain largely unexplored. To deepen theoretical understanding and facilitate catalyst development, this study establishes a direct connection between electronic wavefunctions and hydrogen adsorption by deriving a mathematical formulation from first principles. Beginning with the many-body Schrödinger equation, an analytical model describing the interaction energy between catalyst wavefunctions and hydrogen adsorption is successfully developed. The predicted interaction energy is compared with DFT-obtained values, and the theory is further applied to topological semimetals to elucidate the correlation between topological surface states and hydrogen adsorption behavior. This research provides new insights into HER catalyst design from both an engineering and fundamental perspective. By bridging quantum mechanical principles with catalyst performance metrics, this work offers valuable guidance for selecting and developing next-generation electrocatalysts.

Acknowledgement

I would like to express my heartfelt gratitude to my supervisor Prof. J. Yin, my co-supervisor Prof. X. Zhang and my former supervisor Prof. K. H. Fung, for their invaluable guidance and insightful advice throughout the research study. I am also deeply thankful to my colleagues, research teammates and all those who have supported me during my postgraduate studies.

Contents

List of Figures

List of Tables

Chapter 1

Introduction

1.1 Overview and objectives

Since the dawn of the Industrial Revolution, fossil fuels like coal, oil and natural gas have powered human advancement. Their abundance once seemed like a limitless gift, fueling industries and transforming societies. However, with global energy demands surging-driven by rapid population growth, industrial development, and urban expansion-concerns have mounted over the sustainability of these resources and their environmental consequences. The emission of greenhouse gases and other air pollutants has significantly contributed to climate change and deteriorating air quality, sparking a growing interest in cleaner, renewable energy solutions, for examples, solar, wind or hydropower, etc. [1–5]. Among these alternatives, hydrogen stands out as a particularly promising candidate. Hydrogen offers vast availability and produces no harmful by-products. One of the most compelling methods for its production is the electrochemical hydrogen evolution reaction (HER), which

splits water molecules into hydrogen and oxygen, enabling a clean and renewable fuel source. However, due to the reaction's high energy barrier, efficient electrocatalysts are essential to accelerate the process and boost energy efficiency [6–10].

Noble metals such as platinum (Pt) and palladium (Pd) are regarded as the gold standard for HER catalysis currently, because of their exceptional performance [11–14]. Nevertheless, their scarcity and steep costs pose significant hurdles to widespread adoption. As a result, the hunt for cost-effective, high-performance alternatives has become a major focus of current research [14–18]. With encouraging results, scientists are exploring a wide range of non-precious materials such as metal sulphides [18–21], selenides [22–24], phosphides [25–28], nitrides [29–31] and carbides [32–35]. Despite this progress, matching the catalytic performance and durability of noble metals remains a significant challenge. The quest for affordable, efficient HER catalysts continues to drive innovation, making it one of the most dynamic and impactful areas of sustainable energy research.

Apart from the aforementioned materials, topological materials have emerged as potential candidates for HER catalysis owing to their unique electronic structures and robust surface states [36–38]. Topological materials constitute a unique class of quantum materials characterized by their nontrivial topological order, a concept first predicted in theory during the 20th century [39–41] and confirmed experimentally in the 2010s [42]. The emergence of novel quasiparticles – topological monopoles – in bulk reciprocal space gives rise to exotic electronic states and nontrivial topological phases [43–46]. These distinctive properties have attracted considerable interest in a range of fields, including electronics [47–50], spintronics [51–55] and photonics [56–59]. In condensed matter physics, topological materials are typically catego-

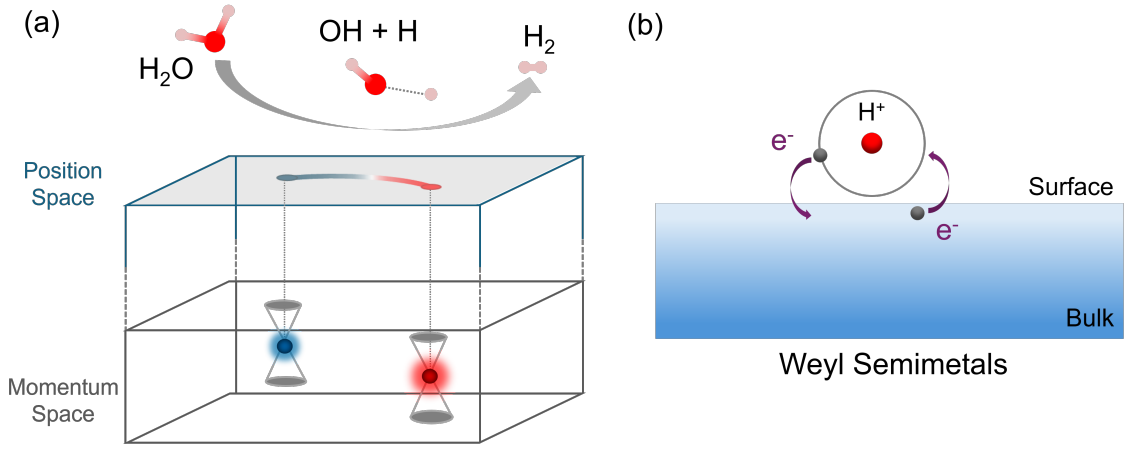

Figure 1.1: (a) Schematic illustrating the influence of topological surface states on water dissociation. The presence of topological monopoles with differing chirality in the bulk momentum space leads to topological phase transitions on the surface momentum space. This transition induces conductive surface electrons with metallic-like properties, thereby facilitating the hydrogen evolution reaction. (b) Schematic of hydrogen adsorption. Conductive electrons originating from topological surface states engage in electron exchange with the hydrogen atom, so do transition metals.

rized based on their electronic characteristics into topological insulators, semimetals, metals and superconductors. Due to the repetitive nature of transition and topological metals, as well as the reliance on external modulation in topological insulators, topological semimetals with their inherently robust surface states that require no external tuning have emerged as a focal point in catalysis research. Topologically protected surface states exhibit high carrier mobility and remarkable resilience to perturbations and structural defects [60–64], positioning them as potential candidates for catalytic applications [38, 65–68].

Topological semimetals fall into three primary categories: Weyl semimetals, Dirac semimetals, and nodal line semimetals. Theoretical research has identified several materials—such as Weyl/Dirac semimetals (e.g., $NbIrTe_4$ [69], NiSi [70], $PtSn_4$ [71]) and nodal line semimetals (e.g., MoP [72], Nb_2S_2C [73], the TiSi family [74], NaAlGe [75], Na_2CdSn [76], Cu_2Si [77])—that exhibit Gibbs free energy

changes for hydrogen adsorption approaching zero eV. This near-zero value is a key indicator of their strong catalytic potential for the HER. Moreover, experimental studies by Rajamathi *et al.* [67] have confirmed HER activity in members of the TaAs family of Weyl semimetals. These promising discoveries have fueled growing interest in utilizing topological semimetals as advanced catalytic materials for next-generation energy applications.

Recent discoveries have paved the way for the development of topological semimetals as alternative HER catalysts. However, optimizing their catalytic efficiency requires a deeper exploration of surface properties, such as facet orientation and termination. Even though topological theory ensures the presence of surface states on different facets, their charge density on various surfaces leads to distinct catalytic performances. Hydrogen adsorption is a key rate-determining step in HER [78–82], but additional factors such as the energy barrier for water dissociation, water adsorption energy and surface energy also provide significantly effect on the generation of hydrogen and their surface stability. To examine these effects, density functional theory (DFT) calculations were conducted to explore how the facet orientation impacts the catalytic HER activity of the TaAs family–the first experimentally confirmed topological Weyl semimetals. Among them, NbP will be used for illustration because the trailblazing experimental work conducted by Rajamathi *et al.* [67] showed NbP exhibiting better performance compared to its counterparts. Other members (TaAs, NbAs and TaP) were also evaluated. For each compound, four distinct facets–(001), (100), (110) and (111)–were systematically studied. Facets with multiple possible terminations were individually labeled and analysed for a relatively comprehensive assessment. The findings confirm that topo-

logical surface states persist across different facet orientations. To provide a robust evaluation of HER activity, four key theoretical descriptors were examined: Gibbs free energy change $\Delta G_{\mathrm{H}*}$, energy barrier of water dissociation E_b, water adsorption energy $\Delta E_{\mathrm{H_2O}*}$ and surface energy γ. These metrics assess the efficiency of hydrogen generation, water dissociation, water adsorption and surface stability respectively. With comparing to the benchmark catalyst Pt (111), most of the examined facets exhibit comparable $\Delta G_{\mathrm{H}*}$ and γ, while demonstrating substantial improvements in $\Delta E_{\mathrm{H_2O}*}$ and E_b. Four descriptors are treated with equal importance and visualized using radar charts. This approach facilitates an integrated evaluation of their combined impact on HER activity, allowing for direct comparisons across different facets and materials. The radar charts effectively highlight performance variations, helping to identify the most promising candidates for efficient hydrogen evolution.

Despite the significance of $\Delta E_{\mathrm{H_2O}*}$, E_b and γ in determining HER efficiency, $\Delta G_{\mathrm{H}*}$ remains a fundamental criterion for the initial selection. $\Delta G_{\mathrm{H}*}$ provides an essential first estimate of a material's potential catalytic activity, helping to screen viable candidates before further evaluation of additional influencing factors. However, beyond topological catalysts, the relationship between surface electronic properties of catalysts and adsorption energy remains poorly understood [78, 83, 84]. The predominant approach to identifying effective catalysts relies on descriptors, which are often derived from statistical correlations rather than a well-established theoretical foundation [85–87]. In many cases, these descriptors are restricted to specific datasets, making their applicability questionable. For instance, the d-band theory has been highly successful in predicting the HER performance of transition metals and alloys over the past 30 years. However, it fails to accurately predict catalytic

behavior in other materials, such as oxides, sulfides and topological semimetals. Similarly, surface density of states has been proposed as a descriptor for topological semimetallic catalysts [66], but its effectiveness remains uncertain, and the reasons causing the relation is still unclear.

To advance catalyst development, it is crucial to establish a fundamental theoretical framework derived from first principles, Schrödinger equation, to elucidate the underlying mechanisms governing the interaction between catalytic properties and hydrogen adsorption. In this study, beginning with the many-body Hamiltonian, the electromagnetic interaction between the catalyst and the adsorbate is treated as a perturbation term. By incorporating the intrinsic differences in atomic and structural characteristics, represented through many-body wavefunctions, the interaction energy between the wavefunctions of catalyst and the adsorbate. The model is then adapted to fit within the DFT framework, allowing for a direct theoretical explanation of interactions between catalysts and adsorbates. This theoretical approach provides a more consolidate foundation for designing and discovering novel HER catalysts. By offering deeper insight into the fundamental principles governing catalytic performance, it presents a valuable strategy for developing next-generation electrocatalysts with enhanced efficiency and stability.

This thesis is structured as follows. Chapter 1 provides an overview of the HER and the fundamental principles of topological semimetals. Additionally, the theoretical framework of DFT and the methodology for evaluating topological properties and HER performance are introduced. In Chapter 2, the topological surface states of various facets are analyzed. Four key descriptors for assessing the HER activity of topological semimetals across different facet orientations are examined.

Chapter 3 presents a newly derived theoretical model that establishes the correlation between the intrinsic properties of catalysts and hydrogen adsorption energy. Finally, Chapter 4 summarizes the findings of this study and discusses potential future research directions.

1.2 Reviews on hydrogen evolution reaction

1.2.1 Gibbs free energy of hydrogen adsorption

The abundance of water presents immense potential as a clean, sustainable and renewable source of electrical energy. For widespread commercialization, the development of noble-metal-free but efficient HER catalysts has become increasingly urgent [6–10]. While the mechanisms behind the hydrogen adsorption, a crucial step in HER, is not yet fully understood. Generally, it is believed that surface-rich delocalized electrons play a key role in enhancing hydrogen yield. Based on this criterion, recent studies have identified metal sulphides [18–21], selenides [22–24], phosphides [25–28], nitrides [29–31] and carbides [32–35] as promising candidates for HER catalysis. Beyond chemical composition, surface properties including atomic arrangement and structural characteristics strongly influence hydrogen adsorption strength, making them critical considerations in catalyst design. In computational studies, adsorption ability and surface stability are commonly used as key metrics for evaluating HER performance.

The HER is a key process in generating hydrogen as a sustainable energy resource by dissociating hydrogen from a solvent. Hydrogen production occurs through two main reaction steps: water dissociation and subsequent hydrogen molecule for-

mation via electron absorption, represented by:

$$H_2O \rightarrow H^+ + OH^-, \tag{1.1a}$$

$$H^+ + e^- \rightarrow \frac{1}{2}H_2. \tag{1.1b}$$

In HER, activation energy of water dissociation, Eq.(1.1a), is relatively high, necessitating the use of electrocatalysts to introduce intermediate states that lower the energy barrier and enhance reaction efficiency. A widely adopted approach to evaluating catalytic performance is analyzing the Gibbs free energy change of hydrogen adsorption for Eq. (1.1b), ΔG_{H*}, which is defined as

$$\Delta G_{H*} \equiv dG = dU + pdV - TdS, \tag{1.2}$$

where dU represents the change of internal energy, p is the pressure, dV denotes the change in volume, T is the absolute temperature and dS is the change of entropy. Eq. (1.2) reflects the strength of interaction between hydrogen molecules and the catalyst surface. If the adsorption energy is excessively strong ($\Delta G_{H*} \ll 0$ eV), hydrogen tends to adhere to the catalyst surface, hindering its release. Conversely, overly weak adsorption ($\Delta G_{H*} \gg 0$ eV) prevents hydrogen atoms from forming molecules on the catalsyt's surfaces. Thus, an optimal ΔG_{H*} value near zero eV is regarded as ideal for efficient HER beacuse of the balance of attractive and repulsive interactions. The relationship between ΔG_{H*} values for transition metals and their catalytic current density, plotted on a logarithmic scale, is illustrated in Fig. 1.2(a), where the data are adapted from Refs. [80]. Experimental current density measurements are compared with ΔG_{H*} values obtained from DFT calculations. The figure reveals a volcanic-shaped trend, where the peak at $\Delta G_H = 0$ eV signifies maximum catalytic efficiency. The figure distinctly establishes Pt as the benchmark catalyst,

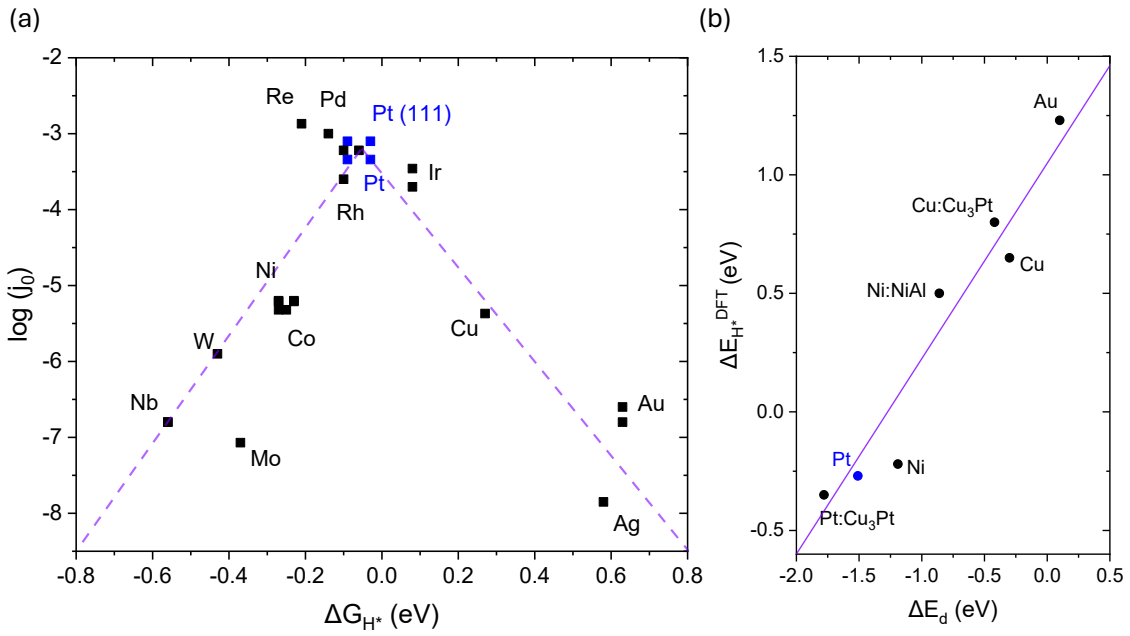

Figure 1.2: (a) Relationship between the computationally calculated Gibbs free energy change of hydrogen adsorption $\Delta G_{\mathrm{H}*}$ (eV) and the logarithm of the experimentally measured exchange current density j_0 (A/cm^2) for various transition metals. Data adapted from Ref. [80]. (b) Correlation between hydrogen adsorption energy predicted by the d-band model ΔE_d, as given in Eq.(1.4), and the adsorption energy obtained directly from computational calculations. Data adapted from Ref. [12].

consistently demonstrating superior HER performance in both computational predictions and experimental measurements. Although factors such as software choices, computational methods and pseudopotential selections may slightly influence ΔG_{H} values, the overall sequence and volcanic trend remain consistent. Building upon this volcanic trend, Nørskov *et al.* [80] applied advanced chemical techniques to formulate the following relationship:

$$j_0 = \begin{cases} -qk_0 \dfrac{1}{1+\exp(\Delta G_{\mathrm{H}*}/k_B T)}, & \text{if } \Delta G_{\mathrm{H}*} < 0 \\ -qk_0 \dfrac{\exp(\Delta G_{\mathrm{H}*}/k_B T)}{1+\exp(\Delta G_{\mathrm{H}*}/k_B T)}, & \text{if } \Delta G_{\mathrm{H}*} > 0 \end{cases}, \tag{1.3}$$

where q, k_0 and k_B are electron charge, reaction rate constant and the Boltzmann constant respectively. The strong correlation between $\Delta G_{\mathrm{H}*}$ and j_0 enables the prediction of HER performance for novel materials based on their $\Delta G_{\mathrm{H}*}$ values. To gain

deeper insights into the hydrogen adsorption mechanism and advance the discovery of efficient HER catalysts, researchers actively seek reliable descriptors capable of accurately predicting $\Delta G_{\mathrm{H}*}$ [12, 83–87]. Developing such predictive models is crucial for guiding the rational design of next-generation electrocatalysts.

The d-band theory is widely recognized as one of the most effective descriptors for predicting the HER performance of transition metals. Due to their highly delocalized nature, d-orbital electrons play a crucial role in electron transfer to the adsorbate. Hammer and Nørskov [12] mathematically demonstrated the relationship between hydrogen adsorption energy and the expected energy value of the d-band in transition metals. The theoretical foundation of the d-band model is rooted in the Newns-Anderson model [88], which involves intricate mathematical formulations. To maintain clarity and accessibility in this thesis, only the essential steps are highlighted. Assuming that the metallic surface consists of single-electron states, the binding energy for a spin-unpolarized system can be expressed as:

$$\Delta E_d = -2\frac{V^2}{\epsilon_{\sigma_u^*} - \epsilon_d} - 2(1-f)\frac{V^2}{\epsilon_d - \epsilon_{\sigma_g}} + \alpha V^2 \propto \beta_1 - \beta_2 \epsilon_d, \tag{1.4}$$

where $\epsilon_{\sigma_u^*}$ and ϵ_{σ_g} represent the energies of the antibonding and bonding states respectively, and ϵ_d denotes the d-band centre. The parameter f corresponds to half of the occupation number at each energy state, accounting for spin degeneracy, while $(1-f)$ reflects the degree of antibonding state occupancy. The matrix element V describes the coupling between the d-state and the adsorbate state, with α as a constant. In principle, V should be expressed as the coupling elements $\langle \mathrm{ads}|H_{\mathrm{bind}}|d\rangle$. However, Eq. (1.4) is simplified by assuming uniform coupling constants. The linear trend observed in Fig. 1.2(b) reinforces the validity of Eq. (1.4) and underscores the predictive power of the d-band model in describing adsorption behaviour. Given

that $V^2 \ll \epsilon_\sigma$, ΔE_d can be expanded using a Taylor series, retaining only the first two terms. This results in a linear relationship between binding energy and the d-band centre, where β represents a set of constants. Hence, the commonly cited linear correlation between hydrogen adsorption energy and the d-band centre, frequently emphasised in mainstream studies, represents merely a special case of Eq. (1.4). As the d-band model originally proposed already three decades ago, the foundational framework has undergone several refinements, including the incorporation of d-band shape [82] and spin degeneracy effects [81]. While d-band theory remains applicable primarily to transition metals, it continues to serve as a powerful index for identifying promising HER catalysts and developing new predictive descriptors.

1.2.2 Extra factors for HER

Beyond $\Delta G_{\mathrm{H}*}$, Eq. (1.1a) highlights the critical role of water adsorption and dissociation in determining the yields of protons and hydroxide ions. In this study, three key descriptors – the water adsorption energy $\Delta E_{\mathrm{H_2O}*}$, the energy barrier for water dissociation ΔE_b and surface stability γ – are also employed to evaluate these chemical processes. First, the water adsorption energy $\Delta E_{\mathrm{H_2O}*}$ represents the binding strength between water molecules and catalyst surfaces. A strong binding interaction is desirable as it stabilizes the water molecules, thereby facilitating their dissociation. Second, a high energy barrier for water dissociation ΔE_b reduces reaction rates and decreases hydrogen molecule yields. For optimal HER efficiency, the ideal value of ΔE_b should approach zero eV. In addition surface orientation and termination can significantly impact adsorption capability and dissociation energy barriers because of distinct local surface potential. Thus, identifying the most ef-

ficient facets and ensuring their structural stability are crucial in catalyst design. Third, surface stability is a critical factor in effective catalyst engineering. Although certain facets may demonstrate outstanding performance in terms of $\Delta G_{\mathrm{H}*}$, $\Delta E_{\mathrm{H_2O}*}$ and ΔE_b, their practical application remains challenging if the surfaces lack stability, making synthesis and long-term viability difficult. To systematically assess surface stability, surface energy γ has been incorporated as a key descriptor, providing a quantitative measure of structural robustness and durability in catalytic environments.

1.3 Reviews on topological theory in condensed matter

1.3.1 Chern numbers and topological insulators

The study of topology in condensed matter physics emerged in the 20th century [39–41], but it has undergone rapid advancements since the 2010s, particularly following the discovery of topological insulators [42]. Theoretical developments in topological condensed matter physics have predicted the existence of a new class of fermions in reciprocal space, capable of inducing non-trivial band structures. These give rise to remarkable physical phenomena such as spin-momentum locking, ultra-high carrier mobility, and the suppression of backscattering [60–64].

Inspired by the Aharonov-Bohm effect, physicists theoretically demonstrated that non-trivial Berry phases, denoted as γ_n, can arise within the band structures of periodic systems, significantly influencing electronic eigenstates. Specifically, the

Berry phase is defined as

$$\gamma_n = i \oint \langle \psi_n(\mathbf{k}) | \nabla_{\mathbf{k}} | \psi_n(\mathbf{k}) \rangle \cdot d\mathbf{k} = \int \nabla_{\mathbf{k}} \times \mathcal{A}_n(\mathbf{k}) \cdot d\mathbf{S} \equiv \int \mathbf{\Omega}_n(\mathbf{k}) \cdot d\mathbf{S}, \tag{1.5}$$

where $\mathcal{A}_n$ and $\mathbf{\Omega}_n$ are respectively known as the Berry connection and Berry curvature at nth band. The surface $\mathbf{S}$ is enclosed by the loop, corresponds to the Brillouin zone in 2D topology. If the Berry curvature $\mathbf{\Omega}_n$ behaves as a field in reciprocal space, the Berry phase γ_n can be interpreted as the flux of the Berry curvature through the Brillouin zone. Consequently, applying the divergence theorem and mapping it to the Gauss-Bonnet theorem, a new class of fermions in momentum space can be obtained as

$$C_n = \frac{1}{2\pi} \int_{\mathrm{BZ}} \mathbf{\Omega}_n(\mathbf{k}) \cdot d\mathbf{S} = 2(1-g), \tag{1.6}$$

where C_n is the Chern number and g is the genus. Since g is a topological invariant that characterizes the topology of a system, it remains unchanged under continuous deformations unless a topological phase transition occurs. Consequently, the Chern number is also a topological invariant, an integer that characterizes the topology of a band. The physical behavior can be understood by treating the Berry connection $\mathcal{A}_n$ as a gauge field in momentum space. The curl of $\mathcal{A}_n$, as expressed in Eq. (1.5), can be interpreted as the "magnetic field" in momentum space, represented by the Berry curvature $\mathbf{\Omega}_n$. Analogous to Gauss's law in electromagnetism, the flux through a closed surface $\mathbf{S}$ corresponds to the total charges or poles. As a result, this topological fermion is classified as a monopole rather than a charge owing to its fundamental definition via the Berry phase. In position space, the Lorentz force is given by

$$\dot{\mathbf{k}} = -\frac{q}{\hbar} \nabla_{\mathbf{r}} V(\mathbf{r}) + \frac{q}{\hbar} \mathbf{v} \times \mathbf{B}(\mathbf{r}), \tag{1.7}$$

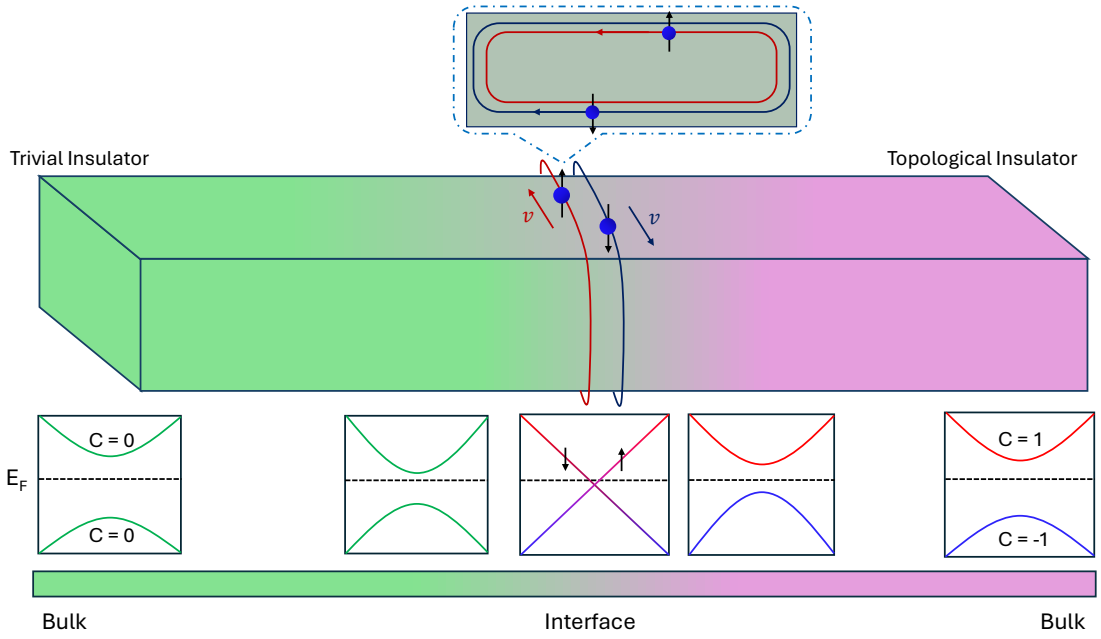

Figure 1.3: Schematic illustration of the quantum spin Hall effect at the interface between a topological and a trivial insulator. At the interface, the transition between the two insulators occurs through a gradual diffusion rather than an abrupt change. In their corresponding 2D band structures, the non-trivial bands progressively shift closer together as one moves from the topological insulator toward the trivial insulator. At a certain location within the interface region, the two bands merge, leading to a topological phase transition. Spin-up and spin-down electrons propagate in opposite directions along the interface, creating a conductive pathway. Eventually, the two bands separate again, but the Chern numbers are reduced to zero.

where q, V, $\mathbf{v}$, and $\mathbf{B}$ represent charge, electric potential, velocity, and magnetic field, respectively. Similarly, an analogous equation holds in momentum space:

$$\dot{\mathbf{r}}_n = \frac{1}{\hbar}\nabla_{\mathbf{k}} E_n(\mathbf{k}) + \dot{\mathbf{k}} \times \mathbf{\Omega}_n(\mathbf{k}). \tag{1.8}$$

Thus, the Chern number is not merely a mathematical construct but also has profound physical implications.

The quantum spin Hall effect (QSHE) is a unique phenomenon observed in topological insulators – materials characterized by non-trivial band structures. When a topological insulator comes into contact with another insulator of differing topology, the topological order must undergo a transition from material A to mate-

rial B, as illustrated in Fig. 1.3. Consequently, a topological phase transition occurs somewhere near the interface. In the electronic band structure at the interface, the conduction and valence bands become connected. This means although both materials are insulating, spin-up and spin-down electrons generate oppositely directed electric currents at the interface while obeying Eq. (1.8), leading to the emergence of a spin current across the boundary. Unlike the conventional spin Hall effect, the spin Hall conductivity in topological insulator is quantized by the Chern number, given by $\sigma_{xy} = Cq^2/h$. In 2007, König *et al.* [42] experimentally confirmed QSHE in HgTe/CdTe quantum wells, proving the theoretical prediction. This discovery not only paved the way for advancements in the study of topological insulators but also ignited substantial interest in exploring other types of topological materials.

1.3.2 Topological semimetals

Rather than considering a whole band across the entire two-dimensional Brillouin zone, topological fermions can emerge at degenerate points or lines within the three-dimensional bulk Brillouin zone. In such cases, it is unnecessary to analyze the entire Brillouin zone; instead, one can focus on an enclosed surface surrounding the degeneracy. This "3D topology" introduces distinct topological phenomena that differ from those observed in 2D topological insulators. Specifically, these topological monopoles are described by the Weyl equations [89]:

$$\sigma^\mu \partial_\mu \Psi_L = 0, \tag{1.9a}$$

$$\bar{\sigma}^\mu \partial_\mu \Psi_R = 0, \tag{1.9b}$$

where $\sigma^\mu = (I_2, \sigma^i)$ and $\bar{\sigma}^\mu = (I_2, -\sigma^i)$. The violation of either parity inversion symmetry $\mathcal{P}$ or time-reversal symmetry $\mathcal{T}$ leads to opposite Berry curvatures, re-

sulting in opposite chirality. The Berry curvature $\Omega(\mathbf{k})$ associated with Eq. (1.9a) in momentum space is $\pm\mathbf{k}/k^3$, with a corresponding Chern number of $+1$. In contrast, the Berry curvature and Chern number of Eq. (1.9b) are reversed. In addition, due to no allowance of net chirality of Weyl fermions in a crystal, Weyl points must be created and annihilated in pairs, ensuring the total Chern number remains zero. In principle, there is no fundamental limit on the number of degeneracies at a single point, meaning that Weyl points with opposite chirality is possible to coexist at the same location. Although the total Chern number enclosed within the enclosed surface becomes zero, the Weyl points themselves may not be annihilated. Consequently, locations where the Chern number vanishes but topological features persist are referred to as Dirac points [38].

This 3D topology gives rise to fundamentally distinct topological phenomena, with topological surface states being a key focus in surface science. In structures with finite periodicity, breaking periodicity along a specific axis transforms the bulk Brillouin zone into a surface Brillouin zone. However, due to the constraint that net chirality cannot exist, topological monopoles must remain connected to facilitate a topological transition, as illustrated in Fig. 1.4(a). On the equi-energy surface of the surface Brillouin zone, nontrivial lines emerge to connect Weyl points of opposite chirality. To complete a closed loop, these nontrivial lines appear on both sides of the surface Brillouin zone with mirrored shapes. Unlike conventional surface states, Fermi arcs are protected by the bulk topology, making them robust against external disturbances such as impurities, defects, and surface terminations. Meanwhile, topological fermions manifest at degeneracy points, observable through their bulk band structures. As shown in Fig. 1.4(b), Weyl points are situated at the intersections

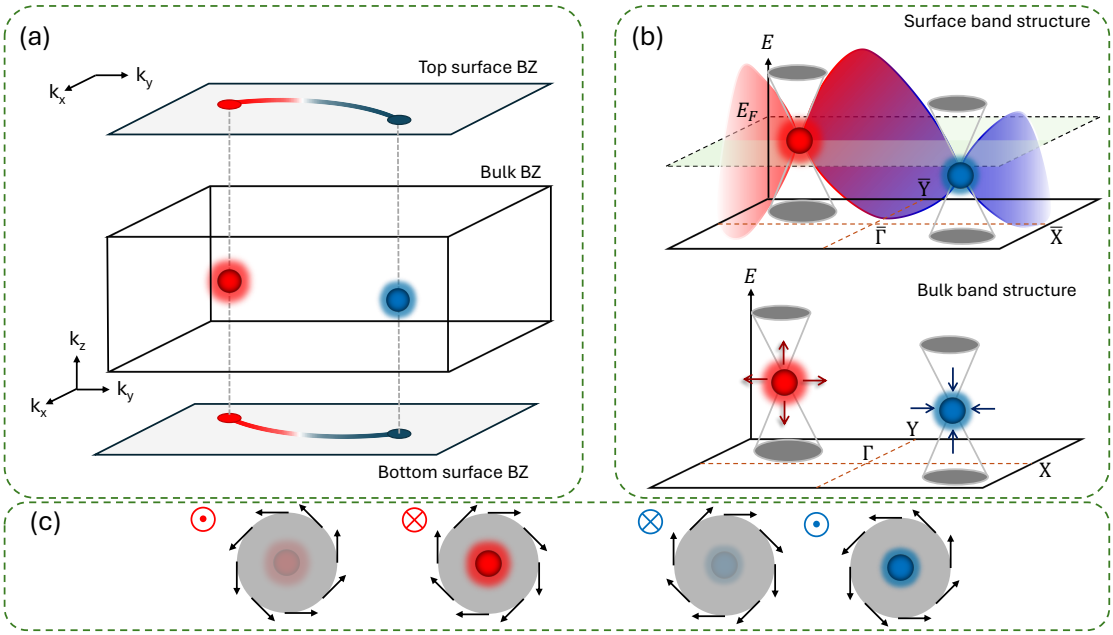

Figure 1.4: (a) Schematic of Weyl points within the three-dimensional Brillouin zone (BZ), alongside the corresponding Fermi arcs on the top and bottom surface BZs. The energy interval is supposed to be significantly small. The red and blue spheres indicate topological monopoles, characterized by Chern numbers $C = 1$ and $C = -1$ respectively. (b) Schematic of Weyl points in the 3D bulk band structure and surface band structures. The Dirac cones are depicted in gray, while the nontrivial surface bands are shown with a gradient colour, signifying the topological phase transition. The intersection lines of Fermi energy surface and surface band are named as Fermi arcs. (c) Schematic of the spin texture influenced by the Berry curvature.

of bulk bands, represented by gray lines and their corresponding Dirac cones. The Berry curvature associated with positive Weyl points points outward, while that of negative Weyl points points inward. As the system transitions from the bulk to the surface, the bulk band structure gradually evolves into a surface band structure, with nontrivial bands connecting Weyl points of opposite chirality. When Weyl points lie near the Fermi level E_F, surface bands may pass thorugh E_F, transitioning from valence to conduction bands, thereby inducing conductive properties on the surface. In other words, delocalized topological surface states emerge when the equi-energy surface at E_F intersects with surface bands, forming Fermi arcs – the intersecting nontrivial lines.

The Berry curvature originating from Weyl points can significantly influence eigenstates, as depicted in Fig. 1.4(c). Analogous to magnetic fields, Berry curvature induces eigenstate rotation in either a clockwise or counterclockwise direction, depending on Weyl point chirality. In 2015, Fermi arcs were experimentally observed in the Weyl semimetal TaAs using angle-resolved photoemission spectroscopy (ARPES) [90–92]. These discoveries marked a pivotal moment in the study of topological semimetals, inspiring extensive research into topological materials and surface science.

1.3.3 Topological semimetals in HER catalysis

The remarkable robustness of topological surface states in Weyl semimetals has garnered widespread interest across diverse branches of surface science. Their exceptional electrical conductivity, rich surface states, and ultrahigh carrier mobility present strong potential for catalytic applications. Rajamathi *et al.* [67] experimentally demonstrated that TaAs family (TaAs, TaP, NbP and NbAs) and T_d-$MoTe_2$ can act as catalysts for the HER. In their study, the dye Eosin Y served as an electron donor, promoting water dissociation and hydrogen generation. Their results show that all members of the TaAs family were able to exhibit HER activity. Although the catalytic performance of these materials was found to be suboptimal in that experiment, the successful demonstration of HER activity confirmed the feasibility of employing topological materials as HER catalysts. More recent computational studies have identified that additional Weyl/Dirac semimetals (e.g., $NbIrTe_4$, NiSi and $PtSn_4$) and nodal-line semimetals (e.g., MoP, Nb_2S_2C, the TiSi family, NaAlGe, Na_2CdSn and Cu_2Si) exhibit ΔG_{H*} values near zero eV, indicating

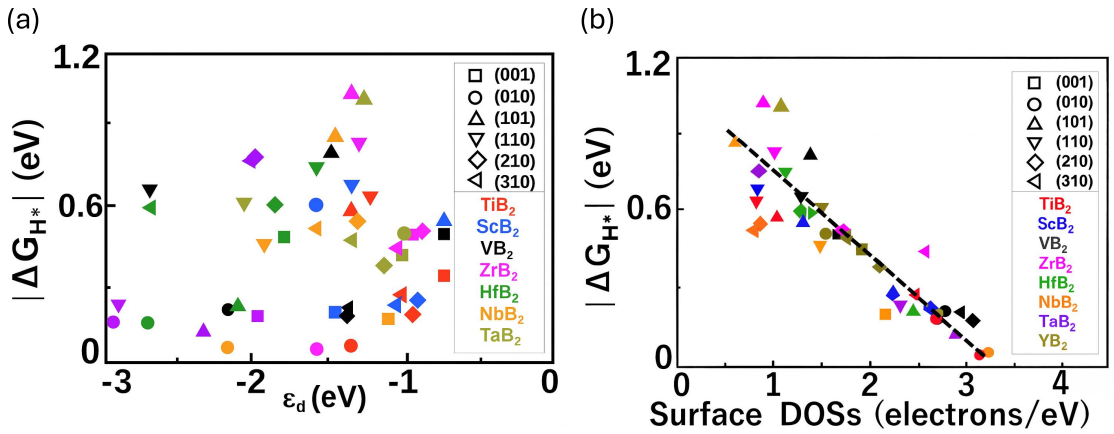

Figure 1.5: (a) The relation of $|\Delta G_{\mathrm{H}*}|$ and the d-band center ϵ_d for MB_2 (M = Ti, Sc, V, Zr, Hf, Nb, Ta, and Y). (b) The relationship between $|\Delta G_{\mathrm{H}*}|$ and the surface density of state for MB_2 with different facets. Figure is adapted from Ref. [66].

their strong potential as highly efficient HER catalysts.

Despite encouraging progress, the relationship between surface characteristics and the ΔG_{H} remains unclear, posing a challenge to the development of highly efficient HER catalysts. Most current research emphasizes the discovery of new HER-active materials, often focusing on surfaces along the axis lacking parity inversion symmetry. However, as illustrated in Fig. 1.4, Fermi arcs are not confined to a single orientation, meaning that they can emerge on various crystal facets depending on the positions of topological monopoles. Moreover, due to the principle of bulk-edge correspondence, different surface terminations yield varied atomic configurations, which in turn produce distinct Fermi arc patterns. Given that the strong correlation between Fermi arcs and surface charge density distributions, these variations can significantly influence hydrogen adsorption behavior. Therefore, a systematic investigation of the interplay between surface structure, topological surface states, and ΔG_{H} is essential for optimizing the catalytic performance of topological semimetals in HER.

To obtain deeper insight into the relationship between topological surface states and the ΔG_{H*}, descriptors related to the intrinsic properties of topological semimetals are being sought, so does *d*-band center theory in transition metals. For instance, the surface density of states has been proposed as a potential descriptor for such systems recently. As shown in Fig. 1.5 adapted from Ref. [66], the *d*-band center of various MB_2 compounds (M = Ti, Sc, V, Zr, Hf, Nb, Ta, and Y) shows no clear correlation with ΔG_{H*} across different facets, whereas their surface density of states appears to exhibit a linear dependence. This suggests that surface density of states may serve as a meaningful descriptor for topological semimetals. However, this descriptor has been derived purely through statistical fitting, lacking a rigorous theoretical underpinning. Moreover, crucial methodological details such as the precise definition of surface density of states and the computational algorithm remain inadequately disclosed. Consequently, the reliability of this descriptor and the nature of its correlation with ΔG_{H*} remain open to question.

Beyond the ΔG_{H*}, other key aspects influencing HER performance such as the surface stability of different facets and the water dissociation capability remain underexplored in topological semimetals. This study seeks to provide a more holistic evaluation of HER activity and to further elucidate the relationship between topological surface states and ΔG_{H*}. Because of the relatively simple topological features , members of the TaAs family, the first experimentally confirmed Weyl semimetals, have been selected for this study.

1.4 Computational methods

1.4.1 Density functional theory

Many-body problems involving more than three interacting particles are generally believed as unsolvable problems using analytical methods. Since 1964, density functional theory (DFT) has been developed as a numerical approach to address the many-body Schrödinger equation. This method is based on two theoretical pillars: the Hohenberg–Kohn theorem [93] and the Kohn–Sham equation [94]. The success of DFT was recognized with the 1998 Nobel Prize in Chemistry, which was awarded to physicist W. Kohn and chemist J. A. Pople. Today, DFT is a widely used and powerful computational tool across condensed matter physics, materials science and chemistry. In this thesis, only the fundamental principles of DFT is introduced. The Hamiltonian in Schrödinger equation of a time-independent many-body system can be expressed as

$$\begin{aligned} H &= T_e + T_N + V_{eN} + V_{ee} + V_{NN} \\ &\equiv -\sum_i \frac{\nabla_i^2}{2} - \sum_I \frac{\nabla_I^2}{2M_I} - \sum_{i,I} \frac{Z_I}{|\mathbf{r}_i - \mathbf{R}_I|} + \sum_{i<j} \frac{1}{|\mathbf{r}_i - \mathbf{r}_j|} + \sum_{I<J} \frac{Z_I Z_J}{|\mathbf{R}_I - \mathbf{R}_J|}, \end{aligned} \tag{1.10}$$

where $\mathbf{r}$ and $\mathbf{R}$ denote the position vectors of electrons and nuclei respectively, while Z, M and m are the nuclear charge, nuclear mass and electron mass. Uppercase and lowercase letters used in subscripts are representing the corresponding variables for nuclei and electrons. All quantities are expressed in atomic units, where $\hbar = m = q_e = 4\pi\varepsilon_0 = 1$. Given the comparatively large mass of nuclei, they can be considered nearly stationary, so that the nuclear kinetic energy operator T_N is assumed to have no contribution to the total wavefunction (i.e., $T_N|\Psi\rangle = 0$). Simultaneously, the ion–ion interaction energy V_{NN} is a constant, omitted from further calculations.

Hence, the total energy can be written as:

$$\langle\Psi|H|\Psi\rangle = \langle\Psi|(T_e + V_{eN} + V_{ee})|\Psi\rangle = E. \tag{1.11}$$

In many-body theory, the number density $n(\mathbf{r})$ is defined as the expectation value of the particle number operator at position $\mathbf{r}$, expressed as $n(\mathbf{r}) = \sum_{i=1}^{N}\langle\Psi|\delta^3(\mathbf{r}-\mathbf{r}_i)|\Psi\rangle$. When the wavefunction is properly normalised, the total number of electrons is conserved as $\int n(\mathbf{r})\, d^3\mathbf{r} = N$. Due to the singularity of the Coulomb potential at nuclear centres, DFT typically replaces it via pseudopotential functions, ensuring the potential remains finite at the origin. As a result, the electron–nucleus interaction potential, V_{eN}, is reformulated as a functional of the electron density $n(\mathbf{r})$:

$$\langle\Psi|V_{eN}|\Psi\rangle = -\int \sum_I \frac{Z_I}{|\mathbf{r}-\mathbf{R}_I|} n(\mathbf{r}) d^3\mathbf{r} \to \int V_{\text{ext}}(\mathbf{r}) n(\mathbf{r}) d^3\mathbf{r}, \tag{1.12}$$

It is important to note that there is no unique expression for the external pseudopotential $V_{\text{ext}}(\mathbf{r})$; various models such as metallic or dielectric spherical approximations may be employed. To balance computational efficiency with physical accuracy, the most widely adopted approaches in DFT are norm-conserving pseudopotentials [95] and ultrasoft pseudopotentials [96, 97].

The presence of electron-electron interactions, denoted as V_{ee}, poses significant challenges for the diagonalisation of the Hamiltonian, rendering Eq. (1.11) analytically intractable. Consequently, appropriate approximations must be introduced. Owing to the fermionic nature of electrons, the "initial guess" of many-body eigenstate $|\Psi\rangle$ is typically represented by a Slater determinant:

$$\begin{aligned}\sqrt{N!}|\Psi\rangle &= |\phi_1\rangle|\phi_2\rangle\cdots|\phi_{N-1}\rangle|\phi_N\rangle - |\phi_2\rangle|\phi_1\rangle\cdots|\phi_{N-1}\rangle|\phi_N\rangle \pm \cdots \\ &= \det\left[|\phi_1\rangle|\phi_2\rangle\cdots|\phi_N\rangle\right].\end{aligned} \tag{1.13}$$

The function $\phi_i(\mathbf{r}_j)$ refers to the spin-orbital wavefunction of the i-th electron evaluated at position $\mathbf{r}_j$. Its spatial component, $\psi_i(\mathbf{r})$, is constructed via the linear combination of atomic orbitals (LCAO) method with proper orthonormalisation:$\psi_i(\mathbf{r}) = \sum_j c_{ij}\varphi_j(\mathbf{r})$, where $\varphi_j(\mathbf{r})$ are atomic orbitals of isolated atoms. Each electron is additionally assigned a distinct spin state, e.g., $\sigma = \alpha$ (spin up) or β (spin down), so that the full single-particle wavefunction becomes $|\phi_i\rangle = |\psi_i, \sigma_i\rangle$. As a result, orthonormality is ensured through $\langle\phi_i|\phi_j\rangle = \langle\psi_i|\psi_j\rangle\langle\sigma_a|\sigma_b\rangle = \delta_{ij}\delta_{ab}$. By substituting Eq. (1.13) into Eq. (1.11) and applying the Slater–Condon rules, the total energy is obtained as

$$E = \sum_{i=1}^{N}\Big[-\frac{1}{2}\langle\phi_i|\nabla_i^2|\phi_i\rangle + \langle\phi_i|V_{\text{ext}}|\phi_i\rangle + \frac{1}{2}\sum_{j\neq i}^{N}\langle\phi_i\phi_j|\frac{1}{|\mathbf{r}_i - \mathbf{r}_j|}\big(|\phi_i\phi_j\rangle - |\phi_j\phi_i\rangle\big)\Big]. \quad (1.14)$$

The first two terms correspond to the kinetic energy and the electron-nucleus potential energy respectively. The third term, known as the Hartree energy, represents the classical Coulomb repulsion felt by an electron due to all other electrons. The final term accounts for the exchange interaction, an inherently quantum mechanical effect arising from the indistinguishability of electrons. Due to the orthonormality of spin–orbital wavefunctions, only electrons with parallel spins can contribute to the exchange term (i.e., $\langle\alpha|\beta\rangle = 0$). In the case of closed-shell configurations, this leads to a ratio of the coefficients between the Hartree and exchange contributions being 2:1.

The Slater determinant serves as an initial guess to the many-body wavefunction rather than an exact solution. Substituting Eq. (1.13) into Eq. (1.11) yields a mean-field description, which corresponds to the first-order term in perturbation theory. Thus, electron correlation effects are entirely neglected in this framework. Within perturbation theory, correlation effects emerge from higher-order contribu-

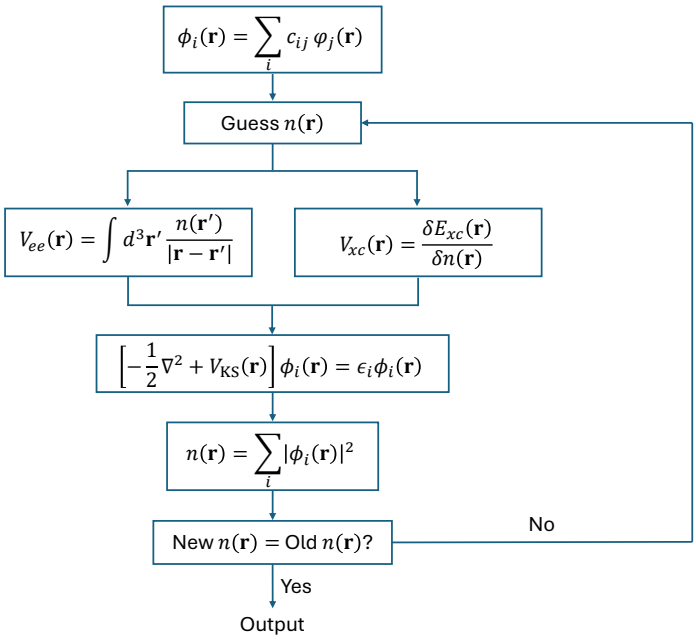

Figure 1.6: Workflow of the self-consistent calculation in Kohn Sham DFT.

tions; it is therefore customary to account for them by introducing a correlation energy term, denoted by E_c. With the inclusion of an appropriate approximation to the exchange interaction, the combined exchange-correlation potential can be incorporated into an effective potential, commonly referred to as the Kohn-Sham potential. The minimisation of the total energy functional can be performed using Lagrange multipliers. Consequently, Eq. (1.11) can be reformulated so that Eq. (1.11) diagonalised as:

$$\sum_i \langle \mathbf{r}|h_i|\phi_i\rangle = \sum_i \left[-\frac{1}{2}\nabla^2 + V_{\mathrm{KS}}(\mathbf{r})\right]\phi_i(\mathbf{r}) = \sum_i \epsilon_i\phi_i(\mathbf{r}), \tag{1.15}$$

where the Kohn-Sham potential V_{KS} is defined as defined as

$$V_{\mathrm{KS}}(\mathbf{r}) = V_{\mathrm{ext}}(\mathbf{r}) + \int \frac{n(\mathbf{r}')}{|\mathbf{r}-\mathbf{r}'|}d^3\mathbf{r}' + \frac{\delta E_{xc}[n]}{\delta n}. \tag{1.16}$$

The many-body problem is thereby reduced to an effective single-particle problem. The ground-state total energy can be obtained by achieving self-consistency between Eqs. (1.15) and (1.16), as illustrated schematically in Fig. 1.6. Exchange-correlation

functionals E_{xc} are typically classified into two main categories: the local density approximation (LDA) [94] and the generalized gradient approximation (GGA) [98]. The LDA is grounded in the physics of a uniform electron gas, whereas the GGA accounts for density inhomogeneities, resulting in functionals of the form:

$$E_{xc}^{\mathrm{LDA}}[n] = \int d^3\mathbf{r}\; n(\mathbf{r})\,\varepsilon(n), \quad E_{xc}^{\mathrm{GGA}}[n] = \int d^3\mathbf{r}\; f(n, \nabla_{\mathbf{r}} n), \tag{1.17}$$

where $\varepsilon(n)$ and $f(n, \nabla_{\mathbf{r}} n)$ are parametrised functions derived from reference systems. Both LDA and GGA have their respective limitations: LDA tends to underestimate lattice constants, while GGA typically overestimates them. Nevertheless, due to their balance between computational cost and acceptable accuracy, these approximations remain widely adopted in practical density functional theory calculations. Finally, due to the double counting of the Hartree energy present in Eq. (1.16), the necessity to incorporate the exchange-correlation correction, and the omission of the nuclear-nuclear interaction energy, the total energy of the system is

$$\begin{aligned} E[n] = \sum_i \epsilon_i - \frac{1}{2} \iint \frac{n(\mathbf{r}) n(\mathbf{r}')}{|\mathbf{r} - \mathbf{r}'|} d^3\mathbf{r}' d^3\mathbf{r} \\ + E_{xc}[n] - \int \frac{\delta E_{xc}[n]}{\delta n} n(\mathbf{r}) d^3\mathbf{r} + \sum_{I<J} \frac{Z_I Z_J}{|\mathbf{R}_I - \mathbf{R}_J|}. \end{aligned} \tag{1.18}$$

It should be noted that the total energy expressed in Eq. (1.18) represents only a general concept. In practice, various DFT software packages implement the total energy differently, often selecting distinct reference energies. As a result, the absolute total energy reported by a given DFT program lacks inherent physical meaning. Instead, the relative energy between two structurally similar systems carries significance, as it effectively cancels out the influence of reference energy choices.

1.4.2 Wannier function

In many condensed matter systems, not all electrons contribute to bonding interactions; a significant number remain effectively independent. Projecting the Kohn-Sham wavefunctions onto an orthonormal basis in position bases provides a more physically insightful representation of their characteristics. In periodic systems, Bloch wavefunctions possess non-zero Fourier components only at reciprocal lattice vectors $\mathbf{R}$. The Kohn-Sham states can be expressed in terms of a set of orthogonal functions ψ_n, as

$$\phi_{m\mathbf{k}}(\mathbf{r}) = \frac{1}{\sqrt{N}} \sum_{\mathbf{R}} e^{i\mathbf{k}\cdot\mathbf{R}} \psi_m(\mathbf{r} - \mathbf{R}). \tag{1.19}$$

These basis functions $\psi_m(\mathbf{r})$ are naturally associated with atomic orbitals. With the LCAO approximation, Wannier functions are approximated by linear combinations of unperturbed atomic orbitals:

$$\psi_m(\mathbf{r}) = \sum_j c_j(\mathbf{R}) \varphi_{m,j}(\mathbf{r} - \mathbf{R}), \tag{1.20}$$

where $\varphi_{m,j}(\mathbf{r})$ represents the atomic orbital and $c_j(\mathbf{R})$ is the coefficients associated weight at site j. In the tight-binding state, the nearest neighbors dominant the energy contribution. The orthonormality of the orbtials implies $\langle \psi_{m,j} | H | \phi_{m\mathbf{k}} \rangle$ with the following the relation:

$$\begin{aligned} c_j E_{m\mathbf{k}} = c_j \int d^3\mathbf{r}\, \varphi^*_{m,j}(\mathbf{r}) H[\varphi_{m,j}(\mathbf{r}) + \varphi_{m,j}(\mathbf{r} - \mathbf{R})] \\ + \sum_{j \neq i} c_i e^{-i\mathbf{k}\cdot\mathbf{R}} \int d^3\mathbf{r}\, \varphi^*_{m,i}(\mathbf{r}) H \varphi_{m,j}(\mathbf{r} - \mathbf{R}), \end{aligned} \tag{1.21}$$

Because the Hamiltonian acting on $\varphi_{m,j}(\mathbf{r} - \mathbf{R})$ are just the energy of the orbitals, it follows that the Kohn-Sham energy $E_{m\mathbf{k}}$ appears as the eigenvalue of the matrix on the right-hand side. Eq. (1.20) represents a foundational concept of the tight-binding

model in its wavefunction form; however, the second-quantised formulation is more commonly employed to describe electron hopping between orbitals. Tight-binding models and Wannier functions are intimately connected. Reformulating Kohn-Sham energy in terms of a tight-binding Hamiltonian provides a powerful framework for investigating topological properties of materials, including the Chern number, Berry curvature and topologically protected surface states. As a representative example, the Su-Schrieffer-Heeger (SSH) model serves as a minimal one-dimensional tight-binding model that captures key features of topological insulators [99]. Although simplified, the SSH model can successfully illustrate concepts such as the Berry phase and topological interface states, as depicted in Fig. 1.3, phenomena not directly evident from the Kohn-Sham wavefunctions alone.

1.5 Conclusion

This chapter has reviewed the fundamental concepts underpinning hydrogen evolution reaction (HER) catalysis and the topological theory relevant to topological semimetals. HER involves two primary steps, with hydrogen adsorption and desorption widely regarded as the rate-determining step. The Gibbs free energy change associated with hydrogen adsorption $\Delta G_{\mathrm{H}*}$ serves as a key descriptor for catalytic activity, owing to its linear correlation with HER performance. From a theoretical standpoint, the most efficient HER catalysts are those for which $\Delta G_{\mathrm{H}*}$ is close to zero. To establish a deeper connection between the intrinsic properties of catalysts and the hydrogen adsorption energy, the search for robust descriptors is ongoing. The widely used d-band centre model – rooted in the Newns-Anderson framework – has been reviewed. This model captures an approximately linear re-

lationship between the d-band centre and hydrogen adsorption energy in transition metals. Nevertheless, it is evident that this approach is insufficient to explain the HER activity of non-transition metal catalysts. In addition to $\Delta G_{\mathrm{H}*}$, other critical energy descriptors such as water adsorption energy $\Delta E_{\mathrm{H_2O}*}$, water dissociation barrier ΔE_b and surface energy γ have been proposed as key descriptors, as these quantities significantly influence hydrogen yield and surface stability.

The chapter also explores the topological theory of semimetals. Topological phases can emerge in momentum space when certain symmetries are broken, giving rise to at least a pair of topological monopoles having opposite chirality. Such phase transitions necessarily result in the formation of topological surface states and Fermi arcs. The robustness and high conductivity of these surface states offer considerable promise for enhancing HER performance. Similar to transition metals, the surface density of states in topological semimetals has been proposed as a potential descriptor for HER activity, aiming to correlate the strength of topological surface states with hydrogen adsorption. However, this approach is currently based purely on statistical fitting and lacks rigorous theoretical foundation, rendering its validity questionable.

This chapter has briefly revisited the foundational principles of DFT and Wannier functions. The computational tools employed, DFT software and Wannier-related packages, have been introduced, along with specific settings used in this study.

Chapter 2

Facet engineering of Weyl semimetals for HER

The design of efficient electrocatalysts for the hydrogen evolution reaction (HER) remains a critical challenge in the development of renewable energy technologies. Owing to the robustness of their topological surface states, Weyl semimetals have emerged as promising candidates for HER catalysis. In this section, the topological surface features of the TaAs family are examined. Notably, Fermi arcs persist even after cleaving along various crystallographic surfaces. To provide a more comprehensive evaluation of HER performance, four key descriptors are considered through DFT calculations: Gibbs free energy of hydrogen adsorption $\Delta G_{\mathrm{H}*}$, energy barrier for water dissociation E_b, water adsorption energy $\Delta E_{\mathrm{H_2O}*}$ and surface energy γ. Among the TaAs family, NbP is selected for detailed illustration due to the pioneering experimental work by Rajamathi *et al.* [67], which identified NbP as exhibiting superior catalytic performance compared to its counterparts. Nevertheless,

the remaining members of the family (TaAs, NbAs, and TaP) are also included in this study for comparative analysis.

2.1 Computational details

Density functional theory (DFT) calculations were carried out by the Vienna Ab initio Simulation Package (VASP). The generalised gradient approximation (GGA) in the form of the Perdew-Burke-Ernzerhof (PBE) functional [98] was chosen for the pseudopotentials and exchange-correlation energy. A plane-wave energy cutoff of 500 eV was adopted, and the Brillouin zone was sampled using a Γ-centred grid with a k-point density of $6 \times 6 \times 6$ for the crystal structures. The convergence thresholds were set to 10^{-6} eV for total energy and -0.01 eV/Å for forces. Topological characteristics were analysed via local Wannier functions as a post-*ab initio* step, using the Wannier90 [100] and WannierTools [101].

To investigate surface properties and catalytic activity for the HER using DFT, slab models were constructed by cleaving the crystal along various crystallographic directions. Vacuum layers ranging from 15 Å to 20 Å were applied, with slabs comprising more than five atomic layers for transition metals and at least eight atomic layers for Weyl semimetals. Supercells of size 2×2 were used for (001) surfaces, and 2×1 supercells were adopted for other facets. An energy cutoff of 450 eV or higher was employed, and the Brillouin zone was sampled using a Γ-centred grid with a k-point mesh of $4 \times 4 \times 1$ for the surface calculations. The convergence thresholds for total energy and forces were identical to those used for the bulk structures. The Gibbs free energy of hydrogen adsorption, $\Delta G_{\mathrm{H}*}$, as defined in Eq. (1.2),

was evaluated according to

$$\Delta G_{\mathrm{H}*} = E_{\mathrm{H}*} - E_* - \frac{1}{2}E_{\mathrm{H_2}} + \Delta E_{\mathrm{ZPE}} - T\Delta S, \tag{2.1}$$

where $E_{\mathrm{H}*}$ is the total energy of the slab with adsorbed hydrogen, E_* is the energy of the clean slab, and $E_{\mathrm{H_2}}$ is the energy of a hydrogen molecule. The term ΔE_{ZPE} accounts for the change in zero-point energy upon adsorption, and $T\Delta S$ reflects the entropy contribution at absolute temperature $T = 298.1$ K. Volume expansion and pressure effects were neglected. Since the slab's vibrational spectrum is expected to vary minimally after hydrogen adsorption, the zero-point energy correction ΔE_{ZPE} was approximated as the vibrational contribution from the adsorbed hydrogen atom: $\Delta E_{\mathrm{ZPE}} = \sum_{i=1}^{3} \hbar\omega_0^i/2$, where ω_0^i denotes the vibrational frequency along the ith degree of freedom. The reference energy E_* was calculated by removing the hydrogen atom without further structural relaxation so as to capture the interaction energy only. While some studies simply assume ΔE_{ZPE} as 0.2 eV, this approach overlooks variations in vibrational behaviour across different surfaces. In this study, ΔE_{ZPE} was explicitly computed using phonon perturbation theory without symmetry constraints, as implemented in VASP.

In addition to evaluating $\Delta G_{\mathrm{H}*}$, the energy barrier for water dissociation, ΔE_b, was investigated using the nudged elastic band (NEB) method to determine the minimum energy pathway of the reaction described in Eq. (1.1a). The energy cutoff, Brillouin zone sampling and convergence criteria were identical to those employed for structure optimisation of slabs. An ionic relaxation criterion of -0.05 eV/Å was applied, with the damped molecular dynamics scheme used for structural relaxation. Five intermediate images were generated by linear interpolation between the reactant and product states. If discontinuities such as atomic jumps were iden-

tified between these configurations, additional NEB calculations were performed.

2.2 Topological surface states in TaAs family

The TaAs family (TaAs, TaP, NbP and NbAs) was the first group of materials experimentally confirmed as Weyl semimetals. All members of this family crystallise in the same body-centred tetragonal structure, belonging to the non-centrosymmetric space group $I4_1md$. The crystal structure of NbP is illustrated in Fig. 2.1(a). TaAs, TaP or NbAs can be obtained by interchaning the metal atoms (Ta and Nb) or the halogen atoms (As and P). In all cases, both the metal and halogen atoms exhibit a coordination number of six. The lattice parameters for each member of the family are summarised in Table 2.1. The bulk and surface Brillouin zones are illustrated in Fig. 2.1(b). To enable comparison with the surface band structures, the bulk band structures with and without of spin-orbital coupling (SOC) are plotted along the high-symmetry path X–Γ–M–Y–Γ, as shown in Figs. 2.1(d) and (f) respectively. The complete bulk band structures for all TaAs family members are provided in Figs. S1 and S2 of the Supplementary. The absence of inversion symmetry along the c-axis leads to the emergence of Weyl points in momentum space. Only the Weyl points situated near the Fermi level are of particular interest, as their associated surface states arise from topological phase transitions

Table 2.1: Lattice parameters of TaAs family members used in this study.

	NbP	TaAs	NbAs	TaP
a (Å)	3.35	3.46	3.49	3.33
c (Å)	11.49	11.78	11.77	11.45

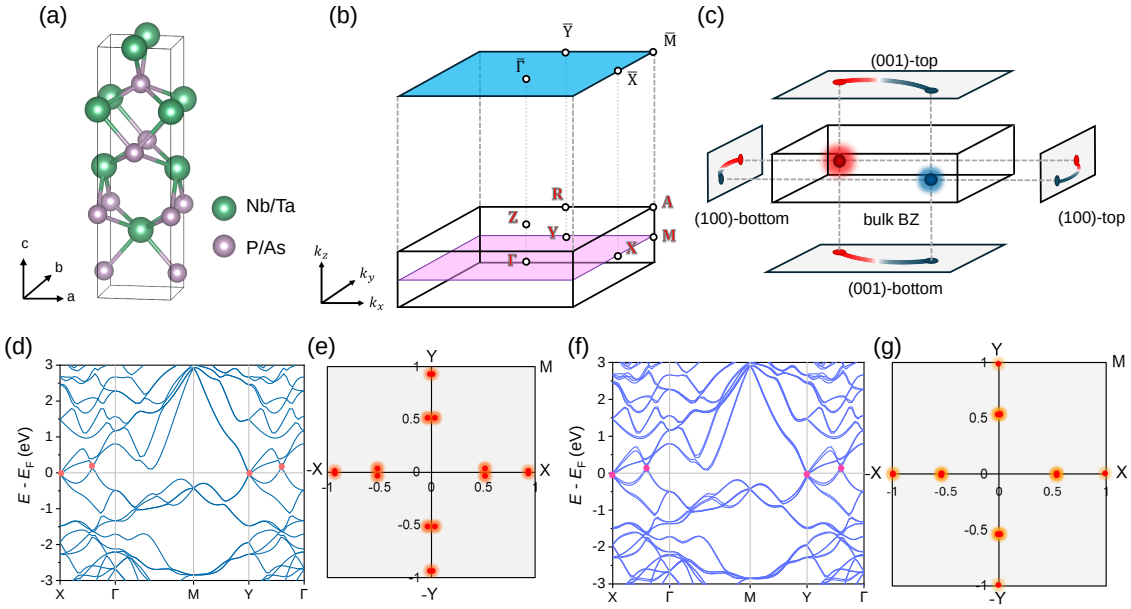

Figure 2.1: (a) Atomic configurations of the TaAs compound family. (b) Bulk and surface Brillouin zones of TaAs family. (c) Illustration of Fermi arcs across different surface Brillouin zones near the Fermi energy. In the bulk Brillouin zone, red and blue spheres represent positive and negative topological monopoles respectively. Their surface projections are connected by the Fermi arcs. (d) Electronic bulk band structure of NbP calculated by GGA/PBE methods. Weyl points are marks in red points. (e) Equi-energy surface arround Fermi energy ($E_F - \varepsilon < E < E_F + \varepsilon$ with a small ε), shown for the bulk crystal with infinite periodicity. Red dots indicate the locations of the Weyl points projected onto the X-Y plane. (f) Electronic bulk band structure of NbP with inclusion of SOC. (g) Equi-energy surface arround Fermi energy for NbP with inclusion of SOC.

and may exhibit conductive behaviour. In the TaAs family, these Weyl points are readily identifiable in the band structures due to their proximity to high-symmetry points, as shown in Fig. 2.1(e) and (g). They are located at the centres of Dirac-like cones, making their topological signatures especially prominent. The incorporation of spin-orbit coupling (SOC) leads to band splitting, yet the locations of the Weyl points are largely preserved.

As aforementioned in previous chapter, the system losses the periodicity when approching to the surface, and results in a transition from bulk to the surface Brillouin zone. Because of no allowance of topological chirality outside the crystal, the

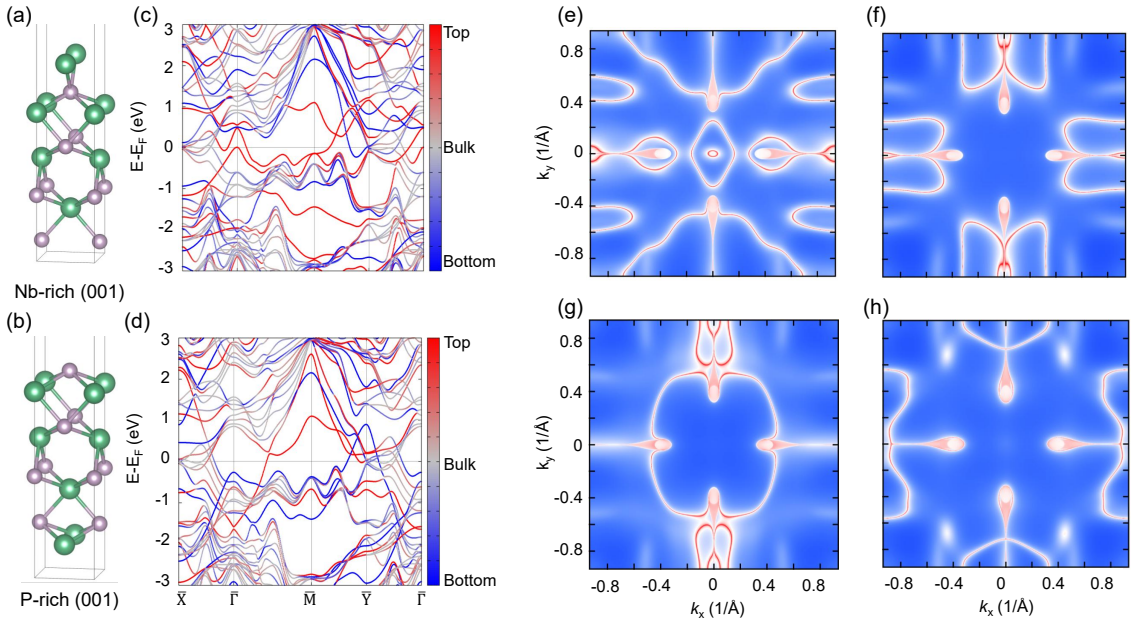

Figure 2.2: Crystal structures of NbP (001) slabs and corresponding Fermi arcs patterns without inclusion of SOC. (a) Nb-rich (001) and (b) P-rich (001). (c) Surface band structures without inclusion of SOC of Nb-rich top and P-rich bottom surfaces. (d) Surface band structure without inclusion of SOC of P-rich top and Nb-rich bottom surfaces. Panels (c) and (d) are calculated using a $1 \times 1 \times 6$ supercell via approach of tight-binding model. Fermi energy surfaces corresponding to: (e) Nb-rich top, (f) P-rich bottom, (g) P-rich top and (h) Nb-rich bottom surfaces of the NbP (001) slab.

topological phase transition occurs at the surface. Hence, Fermi arcs could appear on all surfaces even though the surfaces are not along the direction lacking inversion symmetry. The Schematic of Fermi arcs along different facets is shown in Fig. 2.1(c). Although the topological theory ensures the existence of Fermi arcs on various facets, the patterns of Fermi arcs are still influenced by the atomic arrangement of the surface, inducing different the surface charge density. This is a phenomenon broadly referred to as bulk-edge correspondence. Figs. 2.2(a) and (b) illustrate schematics of NbP (001) slab structures with different terminations: Nb-rich (001)-top and P-rich (001)-top surfaces respectively. Correspondingly, the bottom surfaces in (a) and (b) are defined as P-rich (001)-bottom and Nb-rich (001)-bottom respectively. For clarity, surfaces are classified as (001)-top when the coordination number of the surface

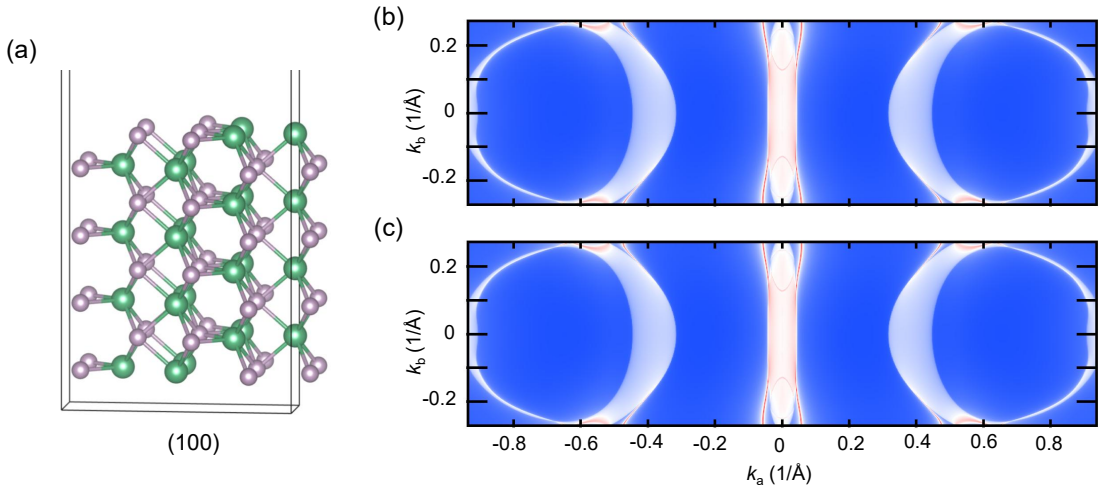

Figure 2.3: (a) Schematics of NbP (100) slab structures and corresponding surface properties. Fermi energy surfaces of NbP (100) of (a) top surface and (b) bottom surface.

Nb atom is 2 or the P atom is 4; otherwise, they are defined as (001)-bottom. This classification scheme is applied consistently across all members of the TaAs family. Figs. 2.2(c) and (d) reveal notable differences in the surface band structures between the two (001) terminations. In comparison with the bulk band structure shown in Fig. 2.1(c), the surface bands (highlighted in red and blue) clearly bridge the Weyl points. The corresponding Fermi surfaces, presented in Figs. 2.2(e)-(h), display not only bulk states but also additional "non-trivial" lines. These emergent patterns differ between the distinct (001) facets, further emphasising the influence of surface termination on the manifestation of Fermi arcs. The results obtained with the inclusion of SOC are presented in Fig. S3 of the Supplementary. Incorporating SOC results in the splitting of Fermi arcs, which induces distinct surface charge densities. This difference is expected to give rise to variations in catalytic performance. When the atomic arrangements of surface facets are identical, the corresponding surface band structures and Fermi arc patterns are expected to be the same. Although the TaAs family lacks inversion symmetry along the *c*-axis, this symmetry is preserved

along the (100) direction. Fig. 2.3(a) presents the schematic of an NbP (100) slab. Due to the translational symmetry across all atomic layers and the presence of inversion symmetry along the a and b axes, as illustrated in Fig. 2.1, the top and bottom surfaces of the slab are structurally identical. Figs. 2.3(c) and (d) display the Fermi surfaces corresponding to the top and bottom (100) surfaces respectively, confirming that their surface electronic states exhibit identical patterns.

These two scenarios provide compelling evidence for the principle of bulk-edge correspondence in Weyl semimetals and potentially in other topological semimetal systems. In this study, the (001), (100), (110), and (111) facets have been investigated. The (010) facet has been excluded as it is equivalent to the (100) facet. As with the (001) terminations, the (111)-top and -bottom surfaces exhibit distinct atomic configurations due to their orientation along a direction lacking inversion symmetry. Accordingly, eight unique surface terminations were constructed for each TaAs family member, resulting in a total of 32 slab models. Top and side views of each slab structure, along with the corresponding Fermi surfaces, are provided in the Supplementary. NbP, TaAs, NbAs and TaP are presented in Figs. S4-S7, S8-S11, S12-S15 and S16-S19 respectively. The results show that Fermi arcs appear on all examined surfaces, even those not aligned with the inversion-symmetry-breaking direction. Notably, although all members of the TaAs family share the same crystal structure and display similar bulk band characteristics, their Fermi arc patterns differ markedly. This suggests that the surface charge distribution varies among the compounds, potentially leading to differences in HER catalytic performance.

2.3 Gibbs free energy change

Weyl semimetals exhibit surface conductivity owing to symmetry-protected delocalised electronic states. Variations in the Fermi arc patterns lead to changes in surface charge density, which in turn influence hydrogen adsorption energies and vibrational modes. These effects result in distinct binding strengths and zero-point energy contributions at different sites. Since optimal HER catalysts are characterised by $\Delta G_{\mathrm{H}*}$ close to zero, the surface charge density plays a crucial role in determining catalytic performance.

In principle, the position-dependent surface potential causes $\Delta G_{\mathrm{H}*}$ to vary across different adsorption sites. These sites can exhibit substantial disparities in adsorption energy. Nonetheless, as described by Eq. (1.3), the catalytic current density j_0 depends exponentially on $\Delta G_{\mathrm{H}*}$. As a result, even slight deviations in $\Delta G_{\mathrm{H}*}$, particularly when it is near zero, can lead to significant differences in reaction rate. Consequently, the most active site is expected to dominate the overall HER process described in Eq. (1.1b). To identify these dominant sites, $\Delta G_{\mathrm{H}*}$ values were computed for all potential hydrogen adsorption locations. Fig. 2.4 presents the spatial distribution of adsorption sites on the NbP (001) surface, along with the corresponding $\Delta G_{\mathrm{H}*}$ values. Adsorption sites where a hydrogen atom was initially placed atop surface atoms such as on Nb or P are denoted as "atom sites" (e.g., "Nb site" or "P site"). In contrast, positions located in interstitial surface regions are labelled as "Hollow sites". Furthermore, structural distinctions such as coordination number or surrounding atomic arrangement led to the classification of multiple variants within the same site type. For example, "Hollow1" and "Hollow2" refer to distinct adsorption environments. Top and side views of the slab structures for various facets are

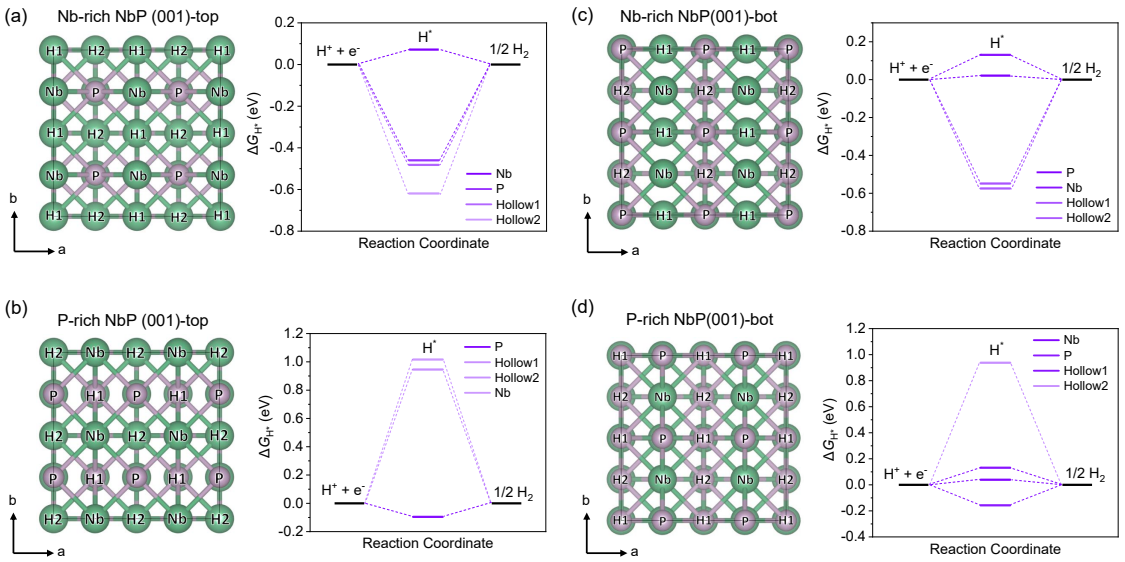

Figure 2.4: Top views of different NbP (001) surfaces and associated Gibbs free energy changes $\Delta G_{\mathrm{H}*}$ for hydrogen evolution reactions: (a) Nb-rich top, (b) P-rich top, (c) Nb-rich bottom and (d) P-rich bottom surfaces. Initial locations for hydrogen adsorption are marked as: Nb (atop a Nb atom), P (atop P atom), and H (hollow site), prior to structural optimization.

provided in Figs. S4-S19, and the computed $\Delta G_{\mathrm{H}*}$ values for each adsorption site across all facets are shown in Figs. S21-S28. Certain adsorption sites were omitted from the $\Delta G_{\mathrm{H}*}$ analysis as the hydrogen atoms either migrated to neighbouring locations or failed to stabilise following structural relaxation. Fig. 2.5(a) presents the calculated $\Delta G_{\mathrm{H}*}$ values for the most active hydrogen adsorption site on each facet with and without SOC, with the benchmark catalyst Pt (111) included for comparison. According to calculations, Pt (111) yields a $\Delta G_{\mathrm{H}*}$ of -0.062 eV. Notably, approximately half of the investigated facets outperform this benchmark in terms of hydrogen adsorption energetics. In the absence of SOC, NbP (100), TaAs (111)-top, Nb-rich NbAs (001)-bottom and TaP (100) exhibit remarkable $\Delta G_{\mathrm{H}*}$ values within their respective type. When SOC is included Nb-rich NbP (001)-top, TaAs (111)-bottom, Nb-rich NbAs (001)-bottom and TaP (100) emerge as the surfaces

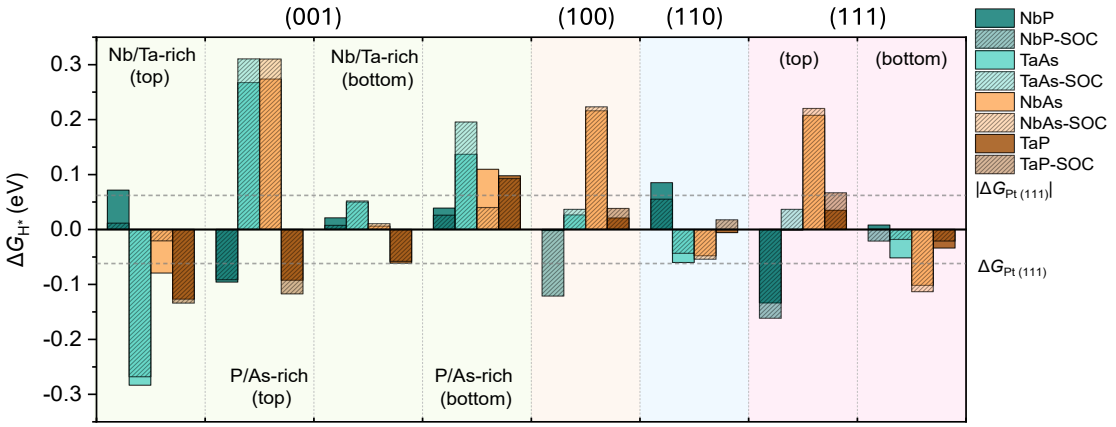

Figure 2.5: (a) Gibbs free energy changes for hydrogen adsorption ΔG_{H*} with and without SOC at the most active sites on various crystal facets of NbP, TaAs, NbAs and TaP. Pt (111) is included as a reference benchmark. Among their respective categories, NbP (100), TaAs (111)-top, Nb-rich NbAs (111)-bottom and TaP (100) demonstrate the most favorable catalytic activity when SOC is absence. Nb-rich NbP (001)-top, TaAs (111)-bottom, Nb-rich NbAs (001)-bottom and TaP (100) exhibit the most favorable catalytic activity when SOC is included.

with remarkable ΔG_{H*} values. These results offer compelling evidence for a strong correlation between ΔG_{H*} and the patterns of Fermi arcs. Moreover, although TaAs family shares the same structure, the optimal facets vary significantly across different materials, with ΔG_{H*} values ranging broadly from approximately -0.3 eV to +0.3 eV. To simplify the analysis, SOC is omitted in the following study, while the methods and results remain applicable.

Although hydrogen adsorption is known to correlate strongly with the presence of delocalised surface electrons, the number of Fermi arcs alone does not reliably indicate catalytic efficiency for the HER. For example, although the NbP (001) facets possess the highest number of Fermi arcs, owing to their alignment along a direction lacking inversion symmetry, they are not serving as optimal facets for the HER. Nonetheless, the NbP (100) facet consists of two Fermi arcs only, but exhibits the most favourable ΔG_{H*} value. The underlying physical mechanism governing

hydrogen adsorption remains an active area of investigation. To probe this relationship further, established descriptors discussed in Chapter 1 – the d-band theory and surface density of states – were employed to examine possible correlations between surface electronic structure and hydrogen adsorption behaviour. While the d-band centre theory provides a clear and well-defined framework, a clear definition of surface density of states was not provided in Ref. [66]. Therefore, this study considers the projected density of states (PDOS) of the surface atoms at the Fermi level, where unit cells have been considered. Unfortunately, as shown in Fig. S29, neither descriptor yields consistent or predictive trends across the studied structures.

A complete theoretical framework linking hydrogen adsorption to topological surface states remains elusive, but it is still possible to evaluate the structural effectiveness by examining the PDOS and charge transfer of surface atoms. Given that the hydrogen atom primarily interact with the surface layers, the PDOS of atoms within the top two layers was examined. Furthermore, since delocalised surface states largely originate from valence shell electrons, the analysis focused on the d-orbitals of metal atoms and the p-orbitals of halogen atoms. To isolate the interaction between the slab and the hydrogen atom, the PDOS was computed using slab structures in which the hydrogen atom was removed from the relaxed adsorption configuration without further structural re-optimisation. Fig. 2.6(a), (c) and (e) present representative PDOS for surface terminations exhibiting $\Delta G_{\mathrm{H}*} \ll 0$ eV, ~ 0 eV, and $\gg 0$ eV respectively. All energy levels are aligned to the Fermi energy of their corresponding systems. For the cases with $\Delta G_{\mathrm{H}*} \ll 0$ eV shown in Fig. 2.6(a), an obvious change in the PDOS of metal atoms near the Fermi level is observed upon hydrogen adsorption, indicating strong attractive interactions. In contrast,

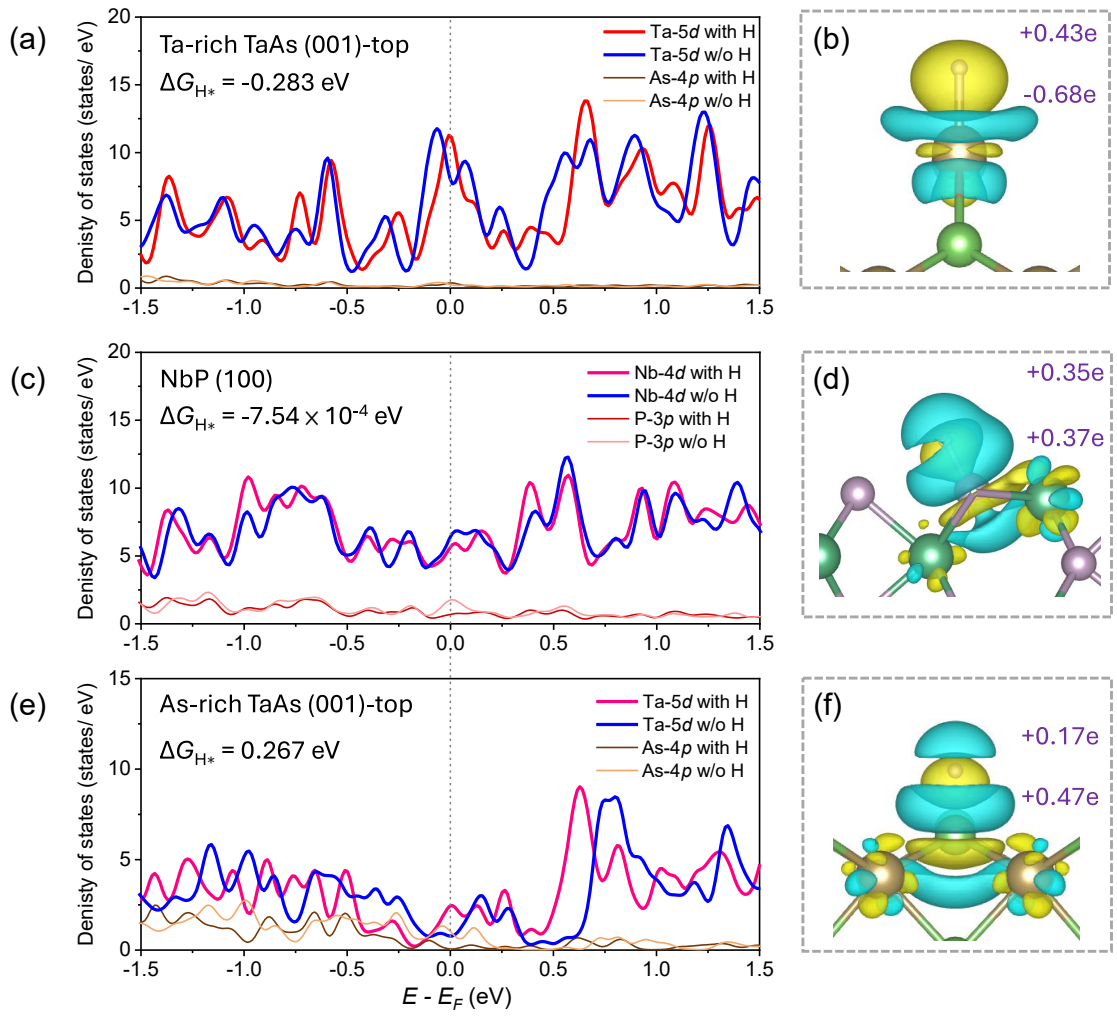

Figure 2.6: Projected density of states (PDOS) of the atoms in top two atomic layers and charge density differences before and after hydrogen adsorption when (a, b) $\Delta G_{H*} \ll 0$ eV, (c, d) $\Delta G_{H*} \sim 0$ eV and (e, f) $\Delta G_{H*} \gg 0$ eV respectively. The yellow and cyan shaded areas in (b), (d) and (f) represent charge accumulation and depletion respectively.

slabs with $\Delta G_{H*} \sim 0$ eV in Fig. 2.6(c) shows only subtle modifications in the *d*-orbital PDOS near the Fermi energy. This modest but optimal change suggests a balanced interaction strength that suppresses zero-point vibrational contributions, yielding nearly thermoneutral hydrogen adsorption. In the cases where $\Delta G_{H*} \gg 0$ eV shown in Fig. 2.6(e), significant deviations in the *d*-orbital PDOS reappear, possibly reflecting repulsive interactions that destabilise hydrogen binding.

To further investigate the origin of the PDOS variations, we employed charge

density difference and Bader charge analyses to evaluate electron gain and loss before and after hydrogen adsorption, as illustrated in Fig. 2.6(b), (d), and (f). In principle, calculating the electrostatic interaction energy arising from the charge redistribution due to hydrogen adsorption, $\Delta\rho(\mathbf{r})$, is nontrivial. For simplicity of discussion, the charge variation induced by hydrogen adsorption has be approximated as a uniform circular charge disc, assumed to be similar across all systems. Under this assumption, the resulting change in potential energy can be expressed as:

$$\Delta V_{\mathrm{H}*} \approx \frac{q_H q_s}{4\pi\varepsilon_0 h^2} - \frac{q_H(q_H+q_s)}{2\pi\varepsilon_0(R_1^2-R_0^2)}(\sqrt{R_1^2+h^2}-\sqrt{R_0^2+h^2}), \tag{2.2}$$

where q_H and q_s denote the charge gain or loss of the hydrogen atom and the surface atom at the adsorption site respectively; h is the vertical separation between the hydrogen atom and the surface atom; R_0 and R_1 represent the radius of the surface atom and the radius of the uniform circular charge disc, respectively; ε_0 is the permittivity of free space. The first term corresponds to the Coulomb interaction between the hydrogen atom and the surface atom at the adsorption site, whereas the second term describes the interaction between the hydrogen atom and the surrounding surface region. By assuming $R_1 = xh \gg R_0$, Eq. (2.2) can be simplified as:

$$\begin{aligned}\Delta V_{\mathrm{H}*} &\approx \frac{q_H q_s}{4\pi\varepsilon_0 h^2} - \frac{q_H(q_H+q_s)}{8\pi\varepsilon_0 h^2}\times\frac{4h}{x^2}(\sqrt{1+x^2}-1) \\ &\equiv \frac{1}{4\pi\varepsilon_0 h^2}\Big(q_H q_s - q_H\frac{q_H+q_s}{2}K\Big)\end{aligned}. \tag{2.3}$$

Since x varies between 4 and 5, the corresponding value of K lies in the range of approximately from 0.9 to 1.2. Therefore, the influence of K can be regarded as negligible in the analysis. When $\Delta G_{\mathrm{H}*} \ll 0$ eV (Fig. 2.6(b)),electron density concentrates around the hydrogen atom while the surface Ta atom undergoes elec-

tron depletion. This charge redistribution generates a dipole moment directed from hydrogen toward Ta atom, yielding $\Delta V_{H*} < 0$ and signifying strong attractive interaction. When $\Delta G_{H*} \sim 0$ eV (Fig. 2.6(d)), both the hydrogen and P atoms acquire comparable electron density. The resulting balanced charge transfer leads to $\Delta V_{H*} \sim 0$, indicative of an energetically favorable, near-optimal interaction. In contrast, when $\Delta G_{H*} \gg 0$ eV (Fig. 2.6(f)),, electrons accumulate on both the hydrogen and As atoms, but preferentially on As. This asymmetric distribution induces a dipole moment pointing away from hydrogen, resulting in $\Delta V_{H*} > 0$ and reflecting strong repulsion. Overall, these PDOS comparisons and Badar change analyses provide valuable insights into the nature of hydrogen adsorption and serve as a qualitative predictor of a surface's suitability for HER catalysis.

2.4 Water dissociation

Water dissociation, as described by Eq. (1.1a), is a critical process that provides the necessary protons to facilitate the HER. The efficiency and kinetics of this dissociation process directly impact the overall hydrogen production rate. Since surface potential is influenced by various factors, including compound type, atomic arrangement and facets, it is essential to investigate facet-dependent behaviour to optimise HER performance. In this study, the water dissociation rate is assessed by examining the energy barrier E_b associated with each facet. The analysis considers the most favourable site for hydrogen adsorption, while positioning the hydroxide ion at an adjacent adsorption site. The Nudged Elastic Band (NEB) method is employed for this purpose. Initially, five intermediate images were generated to model the transition pathway. However, because of the non-uniform atomic composition of

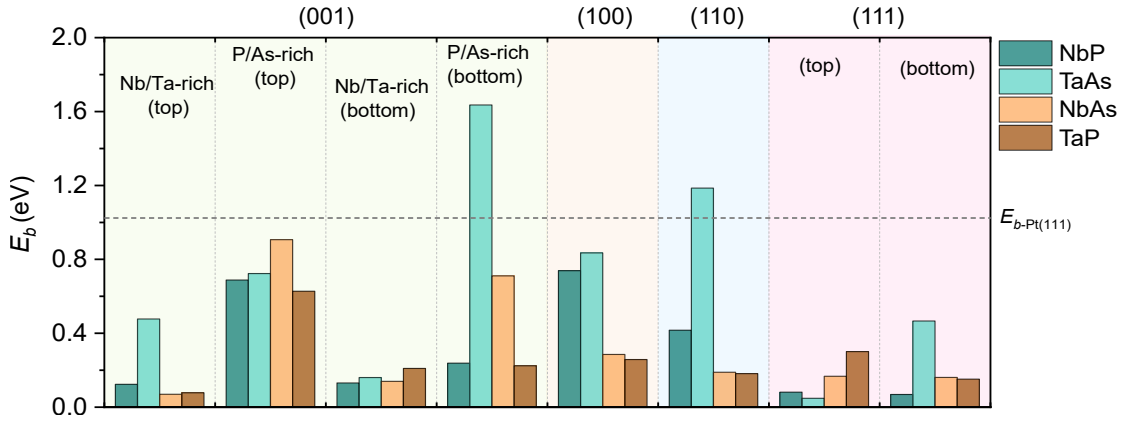

Figure 2.7: Energy barriers E_b for water dissociation reactions across different crystallographic facets of TaAs family. Pt (111) serves as the reference surface. Among all examined configurations, only the As-rich TaAs (001)-bottom and TaAs (110) surfaces require higher activation energy for water dissociation than Pt (111).

the surface, rapid structural fluctuations were observed. This complexity might result in atomic jumps during optimisation, thus additional images might be required to accurately capture the transition state. For benchmarking purposes, the Pt (111) surface was adopted as a reference catalyst.

The activation energies for water dissociation across various facets are presented in Fig. 2.7, with Pt (111) serving as the reference at 1.02 eV. The results show that only the As-rich TaAs (001)-bottom and TaAs (110) facets exhibit activation energies exceeding that of Pt (111). Among the studied surfaces, the NbP (111)-bottom, TaAs (111)-top, Nb-rich NbAs (001)-top and Ta-rich TaP (001)-top facets demonstrate the lowest energy barriers within their respective categories. Detailed results for each compound and facet are available in Fig. S30. The higher activation energies observed in certain slab structures can be attributed to the significant energy required to rearrange surface atoms. In contrast, the lower energy barriers seen in other structures are due to minimal atomic displacement. Fig. 2.8 illustrates the initial, transition and final states of the water-splitting process, showing the pro-

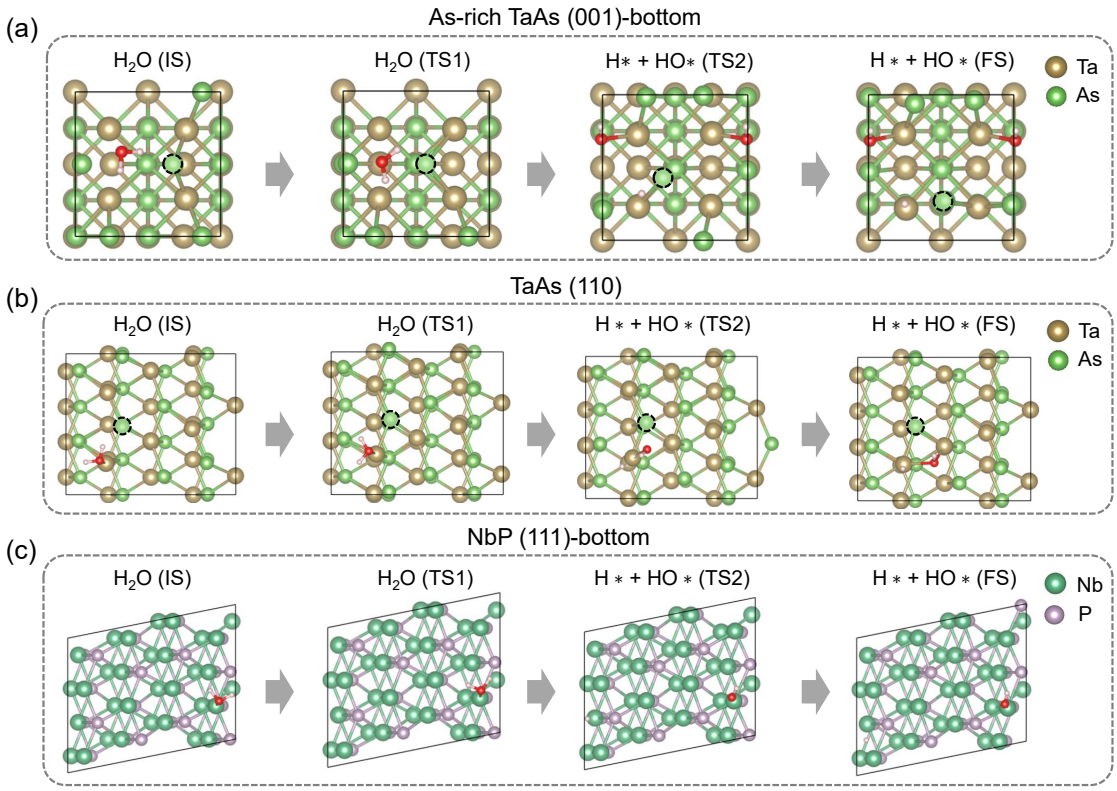

Figure 2.8: Water dissociation pathways for (a) As-rich TaAs (001)-bottom, (b) TaAs (110) and (c) NbP (111)-bottom surfaces. Each sequence illustrates the Initial State (IS), where a water molecule is stably adsorbed on the surface; Transition States 1 and 2 (TS1 and TS2), marking progressive decomposition of water into hydrogen and hydroxide; the Final State (FS), in which both fragments are stably bound to the surface. The energy barrier E_b represents the activation energy between intermediate stages. Black dashed circles highlight the motion of key surface atoms throughout the reaction process.

cesses of As-rich TaAs (001)-bottom and TaAs (110). NbP (111)-bottom is chosen as an example for demonstrating lower activation energetics. In Fig. 2.8(a), strong repulsion between the As atom and the hydroxide ion necessitates a significant shift in atomic configuration to reduce the energy of the system. The approaching hydroxide ion pushes the low-coordination As atom (coordination number = 2) out of its initial site, enabling considerable flexibility. A similar phenomenon is also observed in TaAs (110), shown in Fig. 2.8(b), where an As atom (indicated by a dashed circle) is repelled. However, with a higher coordination number of 4, this atom is more structurally stable and resists displacement, requiring more energy

to disrupt the configuration; hence, the activation barrier has been elevated even though the atomic movement is smaller compared with Fig. 2.8(a). Conversely, as illustrated in Fig. 2.8(c), the surface atoms on the NbP (111)-bottom facet exhibit minimal displacement. This suggests that the interaction energy at the transition state remains well within the tolerance of the four Nb-P bonds, negating the need for major structural rearrangement to lower the total energy. These results collectively indicate that Weyl semimetals can effectively facilitate water dissociation and may even outperform the benchmark catalyst Pt (111) in HER applications.

2.5 Water adsorption energy

The generation of protons and hydroxide ions via water splitting is influenced by the stability of water molecules adsorbed onto the surface. To quantify this stability, the water adsorption energy $\Delta E_{\mathrm{H_2O}*}$ of each slab surface has been calculated. This parameter is defined by the expression: $\Delta E_{\mathrm{H_2O}*} = E_{\mathrm{H_2O}*} - E_* - E_{\mathrm{H_2O}}$, where $E_{\mathrm{H_2O}*}$ is the total energy of the system with an adsorbed water molecule, E_* is the energy of the clean slab, and $E_{\mathrm{H_2O}}$ is the energy of an isolated water molecule. A more negative value of $\Delta E_{\mathrm{H_2O}*}$ reflects a stronger interaction between the water molecule and the catalyst surface, which is favourable for initiating water dissociation and enhancing reaction efficiency.

The overall water adsorption energies are presented in Fig. 2.9, with Pt (111) used as a benchmark for comparison. All examined structures exhibit negative values of $\Delta E_{\mathrm{H_2O}*}$, indicating attractive interactions between the water molecules and the catalyst surfaces. Notably, the calculated adsorption energy for Pt (111) is

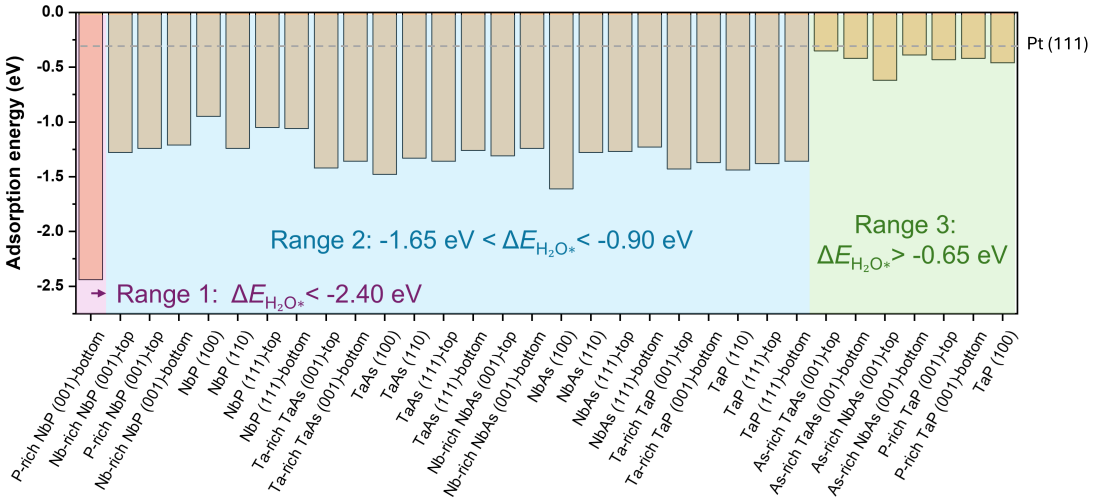

Figure 2.9: The calculated adsorption energies of water molecules, $\Delta E_{\mathrm{H_2O}*}$, on TaAs family surfaces. The results can be divided in 3 regimes: $\Delta E_{\mathrm{H_2O}*} < -2.40$ eV, -1.65 eV $< \Delta E_{\mathrm{H_2O}*} < -0.90$ eV and $\Delta E_{\mathrm{H_2O}*} > -0.65$ eV. All examined structures exhibit stronger water adsorption capability than the benchmark catalyst Pt (111).

-0.316 eV. Based on this value, all studied Weyl semimetal surfaces demonstrate stronger water adsorption capability than the benchmark catalyst. The values of $\Delta E_{\mathrm{H_2O}*}$ for the investigated facets cluster naturally into three distinct ranges: (i) Range 1: $\Delta E_{\mathrm{H_2O}*} < -2.40$ eV, (ii) Range 2: -1.65 eV $< \Delta E_{\mathrm{H_2O}*} < -0.90$ eV and (iii) Range 3: $\Delta E_{\mathrm{H_2O}*} > -0.65$ eV. This division can be rationalised by examining the PDOS of the surface atoms, revealing the interaction between water molecule and surface atoms varies across different structures. Similar to Fig. 2.6, the water adsorption energy is analysed by comparing the PDOS of the p- and d-orbitals of the surface atoms before and after water adsorption. To ensure the change is from the binding energy, the water molecule was removed from the optimised structure without re-optimisation, ensuring that the atomic arrangement of the slab remained unchanged for a consistent comparison. The schematic representations of the water adsorption energy and the corresponding PDOS are presented in Fig. 2.10. In each schematic, the left-hand side depicts the structure before structural relaxation, while

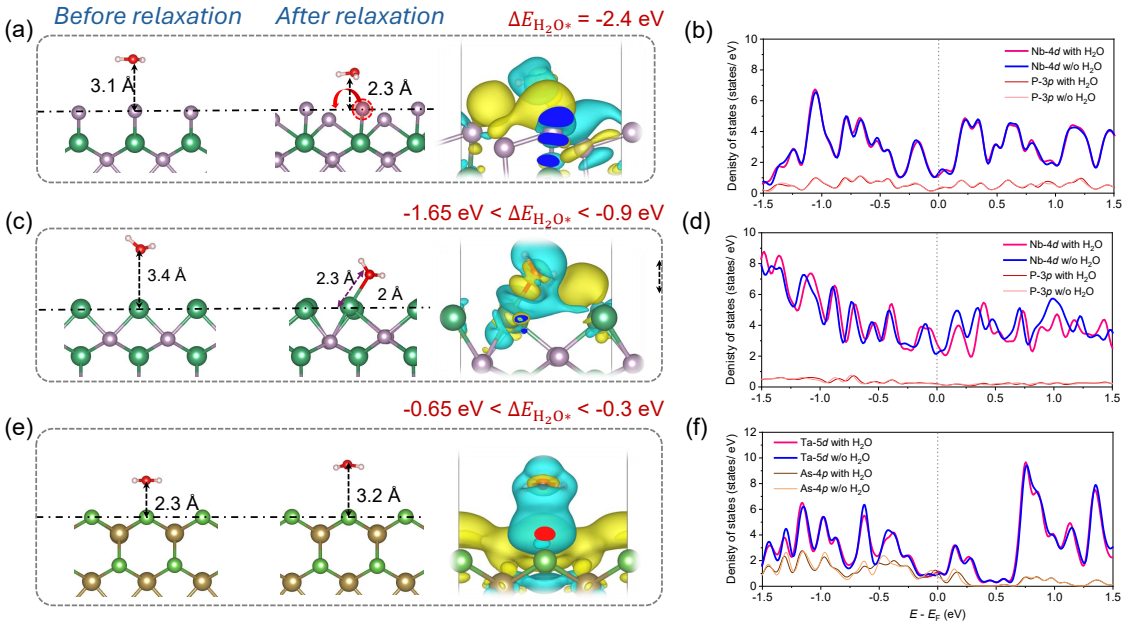

Figure 2.10: Schematic representations of water adsorption energy ΔE_{H_2O*} and the corresponding projected density of states (PDOS) for three energy regimes: (a, b) $\Delta E_{H_2O*} < -2.40$ eV, (c, d) -1.65 eV $< \Delta E_{H_2O*} < -0.90$ eV, and (e, f) $\Delta E_{H_2O*} > -0.65$ eV. For each panel, the structures before and after structural relaxation are shown on the left and right sides in the schematics respectively. The charge density difference maps after relaxation are shown, where the yellow (cyan) shaded area represents charge accumulation (depletion). The PDOS was calculated using atoms from the top two layers of the slab.

the right-hand side shows the configuration after relaxation.

In Fig. 2.10(a), only P-rich NbP (001)-bottom exhibits a water adsorption energy of $\Delta E_{H_2O*} < -2.40$ eV. Upon structural relaxation, the vertical distance between the oxygen atom and the top of the slab surface decreases from 3.1 Å to 2.3 Å. Simultaneously, the labelled P atom moves to a neighbouring site, and forms a new bond with a nearby Nb atom. This movement enhances the Nb-P interaction but not due to the interaction from the slab to the water molecule, thereby lowering the overall water adsorption energy. This inference is supported by the PDOS shown in Fig.2.10(b), where the PDOS profiles of the structure with and without water nearly overlap. These suggest negligible electron exchange and weak electronic cou-

pling between the water molecule and the surface. The charge density difference map further confirms that the electronic orbitals of the water molecule and the slab surface remain non-overlapping. Fig. 2.10(c) features Nb-rich NbP (001)-top as a representative structure in the range -1.65 eV $< \Delta E_{\mathrm{H_2O}*} < -0.90$ eV. Here, the vertical distance between the oxygen atom and the top atomic layer reduces from 3.4 Å to 2.0 Å after relaxation, indicating a more attractive interaction. Notably, this intermediate interaction range is observed only when the oxygen atom strongly interacts with the Nb or Ta surface atoms. This can be attributed to electronic delocalisation at the surface, where the metal atoms become partially cationic. Due to the high electronegativity of oxygen, electrostatic attraction arises between the anionic oxygen and the cationic metal atoms. The PDOS in Fig. 2.10(d) supports this explanation: the *d*-orbitals of Nb below the Fermi level shift towards higher energy upon water adsorption, indicating an electrostatic response. However, the states above the Fermi level do not align even after shifting, reflecting electron exchange and a consequent alteration in the surface electronic structure. The charge density difference map reveals orbital overlap between the water molecule and surface atoms, confirming substantial electronic coupling. For structures in the range $\Delta E_{\mathrm{H_2O}*} > -0.65$ eV, As-rich TaAs (001)-top serves as an example, as shown in Fig.2.10(e). After structural relaxation, the water molecule shifts upwards, suggesting a repulsive interaction. This upward displacement minimises short-range interactions, reducing the binding to weak van der Waals forces. This leads to a higher water adsorption energy. The corresponding PDOS in Fig.2.10(f) shows that the *d*-orbital distributions of Ta atoms remain largely unchanged before and after water adsorption, and the charge density difference map indicates the electronic or-

bitals of the adsorbate and surface remain spatially separated, confirming that the interaction is weak and that no significant electron exchange occurs.

Water adsorption is not considered as the rate-determining step in the HER; however, it remains a vital factor influencing overall catalytic performance. As with hydrogen adsorption, although the fundamental mechanism of water adsorption is still not fully understood, PDOS analysis offers valuable insights into the electronic interactions between water molecules and surface atoms. This approach provides useful clues for interpreting the nature and strength of the adsorption process, and for uncovering the underlying factors governing catalytic efficiency.

2.6 Surface stability

From an engineering perspective, beyond the fundamental processes of water adsorption, water splitting and hydrogen adsorption/desorption, the stability of crystal facets plays a pivotal role in determining the viability of catalysts. Thus, surface energy γ is also an essential parameter for assessing the stability of a cleaved surface. It is given by

$$\gamma = \frac{E_{slab} - N\epsilon_{bulk}}{2A}, \tag{2.4}$$

where E_{slab} is the total energy of the slab, N is the number of atoms in the slab, ϵ_{bulk} is the bulk energy per atom, and A represents the surface area of the slab. Eq. (2.4) assumes the top and bottom surfaces are identical; however, for the (001) and (111) facets, symmetry is broken due to the absence of inversion symmetry along the c-axis. For simplicity, the surface energy γ is taken as the average of the top and bottom surfaces for these facets in this study. Due to compression

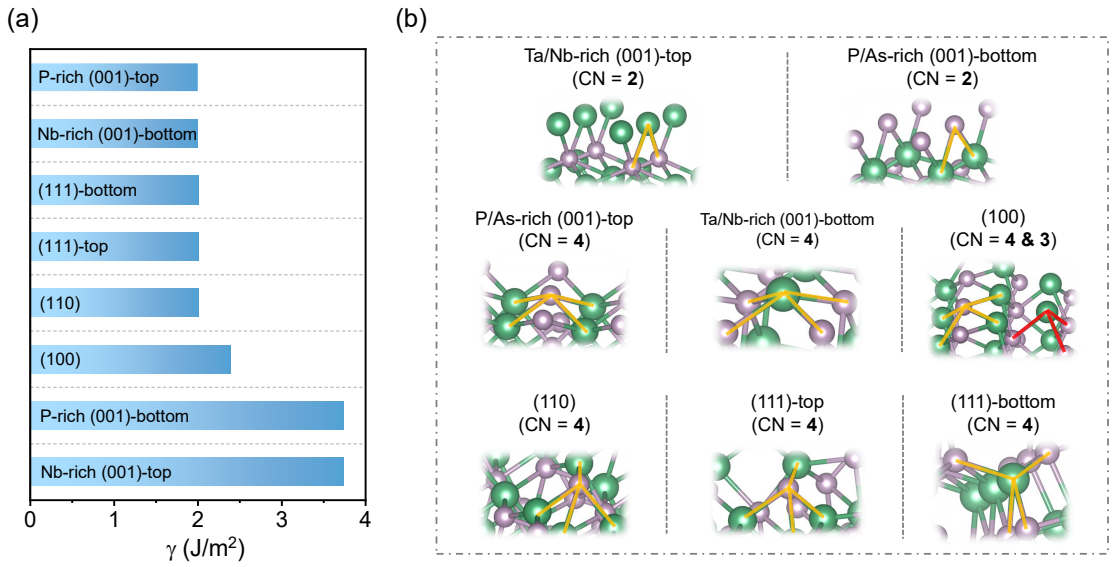

Figure 2.11: (a) Surface energy values of different NbP facets. (b) Atomic configurations of surface terminations, including Ta/Nb-rich (001)-top or P/As-rich (001)-bottom, P/As-rich (001)-top or Ta/Nb-rich (001)-bottom, (100), (110) and (111)-top/bottom facets. The coordination numbers (CN) of surface atoms are indicated by orange and red lines.

induced by vacuum, surface atoms tend to store higher potential energy, typically resulting in $E_{\text{slab}} > N\epsilon_{\text{bulk}}$. In general, higher surface energy correlates with lower thermodynamic stability. Fig. 2.11(a) illustrates the surface energies of various NbP facets, exhibiting the following trend: Nb-rich (001)-top or P-rich (001)-bottom > (100) > Nb-rich (001)-bottom or P-rich (001)-top ≈ (110) ≈ (111). This order is consistent across the TaAs family of compounds.

The relative stability of each facet is influenced by the mobility of surface atoms, as increased atomic flexibility tends to raise the surface energy. Owing to the similarity in crystal structure and lattice parameters across the family (see Table 2.1), the trend in surface energy can be largely attributed to the coordination number of surface atoms rather than detailed bond strength analyses. As shown in Fig. 2.1(a), each bulk atom is coordinated with six atoms of a different type, mean-

ing that six is the most stable configuration. Lower coordination numbers introduce greater atomic freedom, reducing stability. Schematics of different facets and their surface coordination numbers are depicted in Fig. 2.11(b). Although NbP is used here as the representative material, these findings are generally applicable to other members. Ta/Nb-rich (001)-top and P/As-rich (001)-bottom surfaces maintain similar structures through metal-halogen interchangeability, and P/As-rich (001)-top and (111) surfaces also share this structural resemblance. The surface atoms of Ta/Nb-rich (001)-bottom, P/As-rich (001)-top, (110) and (111) facets possess a coordination number of four—the highest among those studied—corresponding to the lowest surface energies and thus the greatest stability. In contrast, (100) facets exhibit coordination numbers of three and four, imparting slightly more atomic freedom and slightly reduced stability. The Nb/Ta-rich (001)-top and As/P-rich (001)-bottom facets, with coordination numbers of two, exhibit the highest degrees of atomic freedom, allowing atoms to lie flat on the surface. This results in the least stable configuration and the highest surface energy. From an engineering standpoint, the Ta/Nb-rich (001)-bottom, P/As-rich (001)-top, (110), and (111) facets are particularly desirable owing to their superior structural stability.

In this study, E_* in Eq. (2.1) is defined as the system energy after removing the hydrogen atom from its relaxed adsorption configuration, without further structural optimisation. This treatment isolates the adsorbate–slab interaction but excludes the additional energy change arising from surface atom rearrangement following hydrogen desorption. Such relaxation can affect the stability of hydrogen adsorption, and the corresponding energy variations for different facets are shown in Fig. S20. The results indicate that all facets–except the As-rich NbAs (001)-bottom

and P-rich NbP (001)-bottom surfaces–exhibit larger energy changes than Pt (111). Even so, all remain below 0.25 eV, suggesting that the impact of surface relaxation after desorption may be minor and does not significantly compromise the adsorption analysis.

2.7 Overall performance

In the preceding sections, four key descriptors—ΔG_{H*}, E_b, ΔE_{H_2O*} and γ—have been analysed individually. While ΔG_{H*} is widely adopted as the primary metric, given that hydrogen desorption is generally regarded as the rate-determining step in the HER, this study highlights that all four criteria significantly influence hydrogen production efficiency. Currently, no universally accepted engineering standard exists for evaluating overall catalytic performance. To address this gap, we propose an integrated assessment framework that assigns equal weight to four key energy descriptors. While the relative importance of these descriptors may vary depending on the specific application, equal weighting provides a neutral baseline for comparison. To facilitate a more holistic evaluation, the descriptors are visualized using radar charts and benchmarked against the reference catalyst Pt (111). Fig. 2.12 presents the radar plots of the most promising catalyst facets in each material group. Detailed radar charts for the individual facets of NbP, TaAs, NbAs and TaP are also provided in Figs. S31-S38.

The radar chart analysis exhibits strong agreement with the experimental trends reported in Ref. [67], where the HER activity was observed to follow the order NbP > TaP > TaAs ≈ NbAs. Notably, the experimental study did not

specify the crystal facets of the samples. If computational analysis considers only ΔG_{H*} and selects facets arbitrarily, the predicted trends deviate from experiment. For instance, metal-rich (001)-top facets yield the order NbP > NbAs > TaP > TaAs, which contradicts the experimental observation. By contrast, when all four energy descriptors are considered and the most stable, catalytically relevant facets are selected for each material, the radar chart analysis aligns well with experimental findings. First, metal-rich (001)-top and halogen-rich (001)-bottom facets can be excluded due to their instability. Second, the water dissociation energy barriers for NbP, NbAs and TaP are comparable and slightly lower than that of TaAs. Third, water adsorption energies for TaAs, TaP and NbAs are similar, while NbP demonstrates better adsorption capability. Finally, the ΔG_{H*} values follow the order NbP > TaP > NbAs $\approx$ TaAs. Taken together, this multi-descriptors' analysis provides a more comprehensive and experimentally consistent evaluation of HER performance.

The radar charts for each facet reveal that all exhibit strong performance in water adsorption, though their overall stability falls short of that of Pt (111). Despite sharing the same crystal structure, members of the TaAs family display considerable variation in $|\Delta G_{H*}|$, E_b, and ΔE_{H_2O*}. Notably, NbP (111)-bottom, TaAs (111)-top, Nb-rich NbAs (001)-bottom and TaP (111) emerge as the top-performing facets within their respective categories. These findings diverge from conclusions drawn solely from ΔG_{H*}. For instance, the As-rich TaAs (001)-bottom facet demonstrates outstanding ΔG_{H*} values, yet its poor performance in E_b, ΔE_{H_2O*} and γ disqualifies it as a viable HER catalyst. This underscores that even an ideal ΔG_{H*} does not guarantee a facet's effectiveness for HER. In this study, all four descriptors—ΔG_{H*},

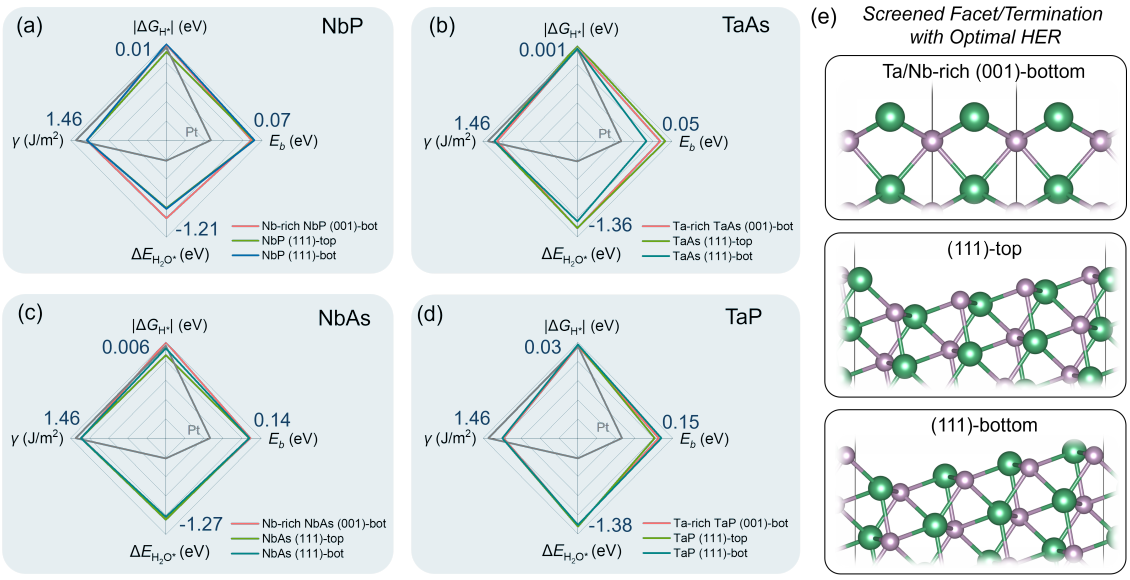

Figure 2.12: Radar charts for evaluation of the overall performance of (a) NbP, (b) TaAs, (c) NbAs and (d) TaP, highlighting the screened optimal surface facets for each material. The plotted parameters include the Gibbs free energy change for hydrogen adsorption $\Delta G_{\mathrm{H}*}$, the energy barrier for water dissociation E_b, the water adsorption energy $\Delta E_{\mathrm{H_2O}*}$ and the surface energy γ. The value for the most in each category is indicated. Panel (e) presents the identified high-activity HER facets or terminations across the TaAs family.

E_b, $\Delta E_{\mathrm{H_2O}*}$ and γ—are treated with equal importance. Consequently, although the P-rich NbP (001)-bottom facet exhibits excellent values in $\Delta G_{\mathrm{H}*}$, E_b and $\Delta E_{\mathrm{H_2O}*}$, its high surface energy renders it unsuitable as an optimal HER catalyst. Two overarching trends can be discerned: (i) metal-rich (001)-top facets perform exceptionally well in $|\Delta G_{\mathrm{H}*}|$, E_b and $\Delta E_{\mathrm{H_2O}*}$, but their high surface energy γ compromises their catalytic viability; (ii) by contrast, all metal-rich (001)-bottom and (111) facets exhibit strong performance across all four energy descriptors, making them particularly promising candidates for HER catalysis.

2.8 Conclusion

In this chapter, DFT calculations were employed to investigate the influence of different crystal facets on the electrocatalytic HER activity of TaAs family (TaAs,

NbP, NbAs and TaP). The results indicate that topological surface states (visualised through Fermi arcs) are preserved across various facets. Due to the principle of bulk-edge correspondence, the configurations of these Fermi arcs are intrinsically linked to the atomic arrangements of the respective surfaces. Although the number of Fermi arcs affects the surface charge density, its influence on HER activity appears to be minimal. Nevertheless, variations in the PDOS of surface atoms can be clearly observed, displaying a strong correlation with hydrogen adsorption. This makes the PDOS a valuable indicator for assessing HER activity.

To comprehensively assess HER performance, four descriptors were examined: the Gibbs free energy of hydrogen adsorption ($\Delta G_{\mathrm{H}*}$), the energy barrier for water dissociation E_b, the water adsorption energy $\Delta E_{\mathrm{H_2O}*}$, and the surface energy γ. Unlike conventional approaches that prioritize a single descriptor, this study evaluates all four on equal footing. Relative to the benchmark catalyst Pt (111), most investigated facets show comparable values for $\Delta G_{\mathrm{H}*}$ and γ, while achieving notable improvements in water dissociation and adsorption energetics. Integrated analysis using radar charts highlights the (111) facet and the metal-rich (001)-bottom facet as exhibiting balanced, favorable values across all descriptors, suggesting superior HER activity compared to Pt (111). These results provide new perspectives for identifying optimal HER catalysts and may guide the rational design of high-performance materials for practical applications.

Chapter 3

Theoretical illustrations on the relation of topological surface states and hydrogen adsorption

Catalytic performance correlates with the Gibbs free energy change of hydrogen adsorption $\Delta G_{\mathrm{H}*}$. In the previous chapter, the analysis of $\Delta G_{\mathrm{H}*}$ served as the basis for further investigations into water adsorption energy $\Delta E_{\mathrm{H_2O}*}$ and the activation barrier for water dissociation E_b. Although three additional descriptors were introduced and their relevance highlighted, hydrogen adsorption energy $\Delta E_{\mathrm{H}*}$ remains a fundamental parameter and the initial metric to assess. Topology in condensed matter physics is a theory driven by abstract principles, underpinned by rigorous mathematical foundations of topological surface states. Although it is well-known that hydrogen adsorption correlates with surface charge density, which was demonstrated through the PDOS of surface atoms, a comprehensive theoretical

and mathematical framework for this relationship has yet to be developed. This absence creates a gap between surface electronic properties and hydrogen adsorption behaviour, particularly in the context of topological surface states. To bridge this gap, it is essential to construct a more fundamental theoretical framework grounded in first principles of quantum mechanics.

The *d*-band model originates from the Newns-Anderson model developed in 1968. This framework employed a tight-binding approach within the formalism of second quantisation to describe the interaction between adsorbates and metal surfaces [88]. Initially, the development of the model was focusing on transition metals due to the lack of numerical methods for accurately predicting many-body wavefunctions. Today, it is widely acknowledged that the many-body Schrödinger equation cannot be solved analytically. Nonetheless, it remains possible to derive analytical expressions for interaction energies by incorporating numerically calculated many-body wavefunctions of the catalytic slab and the adsorbed hydrogen atom.

In this chapter, beginning with the many-body Schrödinger equation, the technique of perturbation theory is employed to derive a mathematical expression for hydrogen adsorption energy, offering insights into the interaction energies between catalyst wavefunctions and adsorbed hydrogen. This framework enhances our understanding of the electronic factors that govern catalytic activity. To validate the theoretical model, a comparative analysis is carried out using transition metals, assessing the agreement between predicted interaction energies and the DFT results. The theory is subsequently applied to the TaAs family, examining various crystallographic facets to explore the relationship between topological surface states and hydrogen adsorption behaviour.

3.1 Theoretical derivation for hydrogen adsorption in short range

According to Eq. (2.1), the hydrogen adsorption energy, or binding energy $\Delta E_{\mathrm{H}*}$, represents the interaction energy between the catalyst and the adsorbed hydrogen atom. This interaction comprises various contributions, including direct Coulombic forces, electron exchange interactions, correlation effects and van der Waals forces. However, within the framework of quantum physics, these contributions can be broadly classified under electrostatic interactions between cations and electrons. Suppose the subscripts of $a, b, c...$ and $i, j, k, ...$ are the indices of atoms and electrons respectively, while the subscripts H and e are used to emphasise the atom and electron belonging to the hydrogen atom. With this indexing scheme, the many-body Hamiltonian of the system can be partitioned into three components:

$$H = H_{\mathrm{slab}} + H_{\mathrm{ads}} + H_{\mathrm{int}}, \tag{3.1}$$

where H_{slab}, H_{ads} and H_{int} are the slab, adsorbate and interaction Hamiltonian. To be specific,

$$\begin{aligned} H_{\mathrm{slab}} = & -\frac{\hbar^2}{2m}\sum_i \nabla_i^2 + \frac{q^2}{4\pi\varepsilon_0}\Bigg(-\sum_i \frac{Z_a}{|\mathbf{R}_a - \mathbf{r}_i|} + \sum_{a<b}\frac{Z_a Z_b}{|\mathbf{R}_a - \mathbf{R}_b|} \\ & -\sum_{a<b}\frac{Z_a}{|\mathbf{R}_a - \mathbf{r}_i|} + \sum_{a<b}\sum_{i,j}\frac{1}{|\mathbf{r}_i - \mathbf{r}_j|}\Bigg), \end{aligned} \tag{3.2a}$$

$$H_{\mathrm{ads}} = -\frac{\hbar^2}{2m}\nabla_e^2 - \frac{q^2}{4\pi\varepsilon_0}\frac{Z_H}{|\mathbf{R}_H - \mathbf{r}_e|}, \tag{3.2b}$$

$$\begin{aligned} H_{\mathrm{int}} = & \frac{q^2}{4\pi\varepsilon_0}\Bigg(\sum_a \frac{Z_a Z_H}{|\mathbf{R}_a - \mathbf{R}_H|} - \sum_a \frac{Z_a}{|\mathbf{R}_a - \mathbf{r}_e|} - \sum_i \frac{Z_H}{|\mathbf{R}_H - \mathbf{r}_i|} \\ & + \sum_i \frac{1}{|\mathbf{r}_i - \mathbf{r}_e|}\Bigg), \end{aligned} \tag{3.2c}$$

where Z, q, m, $\mathbf{R}$, $\mathbf{r}$ and ε_0 are the atomic number, electron charge, position vector of ion, position vector of electrons and the dielectric permitivity in vacuum respectively.

The eigenvalues of Eqs. (3.2a) and (3.2b) correspond to the energies of the catalytic slab and the hydrogen atom respectively, and are assumed to be known quantities. The central objective of perturbation theory in this context is to approximate the eigenvalue of Eq.(3.1), which describes the combined system—by relying solely on the eigenvalues and eigenstates derived from Eqs. (3.2a) and (3.2b). i.e.,

$$E_0 = E_{\text{slab}}^{(0)} + E_{\text{ads}}^{(0)} + \langle \Psi_0^{(0)} | H_{\text{int}} | \Psi_0^{(0)} \rangle + \sum_{m \neq 0} \frac{|\langle \Psi_m^{(0)} | H_{\text{int}} | \Psi_0^{(0)} \rangle|^2}{E_0^{(0)} - E_m^{(0)}} + \cdots , \tag{3.3}$$

where the superscript (0) denotes the unperturbed system, while the subscript 0 emphasises the consideration of the ground state. In essence, the interaction energy arises starting from the third term of Eq. (3.3). It is evident that the first-order perturbation corresponds to the mean-field approximation, which effectively captures short-range interaction energies but offers a limited description of long-range interactions. In comparison, the second-order perturbation is capable of accounting for long-range effects such as van der Waals forces. These two perturbative contributions form the theoretical underpinning of the Lennard-Jones potential, which traditionally describes atom-atom interactions developed by a statistical framework. By contrast, Eq. (3.3) establishes a rigorous theoretical foundation for investigating interaction energies from first principles in many-body quantum mechanics. Given that short-range interactions are often associated with exchange interactions, it is reasonable to expect that the first-order perturbation term constitutes a generalised form of the exchange energy observed in hydrogen molecules, of which the interaction is typically expressed as:

$$E_{\text{ex}} = \frac{C \pm J}{1 \pm S^2}, \tag{3.4}$$

Here, C, J and S represent the Coulomb, exchange and overlap integrals respectively; the explicit expressions for each term are omitted here. The $\pm$ sign reflects the

symmetry of the spatial two-body wavefunction, where positive for the symmetric (parallel spin orientation) and negative for the anti-symmetric (orthogonal spin orientation) configuration. When two hydrogen atoms begin to overlap, the Coulomb integral transitions from zero to negative values, indicating a repulsive electrostatic interaction. Simultaneously, the exchange integral J initially rises from zero, contributing positively to the interaction energy; however, it eventually declines and can even become negative at certain interatomic separations. This behaviour captures the delicate interplay between attractive and repulsive forces arising purely from quantum exchange mechanisms. Owing to the fermionic nature of electrons, the "unperturbed" many-body wavefunction is appropriately represented using a Slater determinant, which ensures antisymmetry under exchange of identical particles and satisfies the Pauli exclusion principle

$$\Psi_0^{(0)}(\{\mathbf{r}_i\}) = \sum_{\sigma} \varepsilon_{\sigma_1\sigma_2\ldots\sigma_{N+1}} \prod_{i}^{N+1} \phi_{\sigma_i}(\mathbf{r}_i), \tag{3.5}$$

where $\sum_{\sigma} \varepsilon_{\sigma_i}$ represents the Levi-Civita symbol, accounting for all permutations necessary to construct the antisymmetric many-body wavefunction, while $\phi_{\sigma_i}(\mathbf{r}_i)$ denotes the spin-orbital wavefunctions of the i-th electron. The subscript 0 highlights the ground state configuration of the system. Among the $N+1$ electrons, the first N originate from the slab, and the final electron is associated with the hydrogen atom. Ideally, the single-particle wavefunctions of the slab satisfy orthonormality, i.e., $\langle\phi_i|\phi_j\rangle = \delta_{ij}$, but this condition cannot be held prior to perturbative treatment or self-consistent field convergence when combining two independent systems. Consequently, the normalisation factor deviates from the canonical form $\sqrt{(N+1)!}$. The first-order perturbation expression derived from Eq. (3.2c) is

$$E_0^{(1)} = \frac{\langle\Psi_0^{(0)}|H_{\text{int}}|\Psi_0^{(0)}\rangle}{\langle\Psi_0^{(0)}|\Psi_0^{(0)}\rangle} = \frac{q^2}{4\pi\varepsilon_0}(E_{\text{ion-ion}} - E_{\text{ion-e}} + E_{\text{e-e}}). \tag{3.6}$$

$E_{\text{ion-ion}}$, $E_{\text{ion-e}}$ and $E_{\text{e-e}}$ represent the interaction energies between ions, between ions and electrons, and between electrons respectively. The full derivation and explicit formulation of each term can be found in Appendix A. Although the expression of Eq. (3.6) is mathematically complicated, its validity can be verified by applying it to a hydrogen molecule, recovering Eq. (3.4). Therefore, Eq. (3.6) could be regarded as a generalised expression for the interaction energy between an isolated system and a hydrogen atom. In contrast to the approach adopted in the Hartree-Fock method discussed in Chapter 1, Eq. (3.6) emphasises that the individual electronic wavefunctions of the two isolated systems are treated independently, rather than assuming a linear combination of their orbitals.

To extend the theoretical model to periodic systems, the particle states of the slab must be reformulated as Bloch states, while the hydrogen atom continues to be treated as an isolated atom. Although density functional theory (DFT) is employed in this thesis, Eq. (3.6) remains applicable to a broader class of systems beyond DFT. Within the DFT framework, the Hilbert space is spanned by wavefunctions characterised by distinct crystal momentum vectors $\mathbf{k}$, each weighted by a factor $w_{\mathbf{k}}$: $\mathcal{H} = \mathcal{H}_{\mathbf{k}_1} \bigoplus \mathcal{H}_{\mathbf{k}_2} \bigoplus \cdots$. These subspaces $\mathcal{H}_{\mathbf{k}}$ are mutually independent in the absence of interactions that couple different $\mathbf{k}$ states, such as phonons. Since the Hamiltonian in Eq. (3.1) does not include such effects, the independence of the $\mathcal{H}_{\mathbf{k}}$ subspaces is preserved. Consequently, the total energy of the system, as computed by DFT, takes the form: $E_{\text{total}} = \sum_{m,\mathbf{k}} w_{\mathbf{k}} \left(f^{\uparrow}_{m\mathbf{k}} + f^{\downarrow}_{m\mathbf{k}} \right) E_{m\mathbf{k}}$, where $f^{\uparrow}_{m\mathbf{k}}$ and $f^{\downarrow}_{m\mathbf{k}}$ are the occupation numbers for spin-up and spin-down electrons, $w_{\mathbf{k}}$ is the weighting factor at each $\mathbf{k}$,and $E_{m\mathbf{k}}$ is the energy of the m-th band at momentum $\mathbf{k}$. The corresponding eigenstates could be normalised as $\sqrt{f_{m\mathbf{k}}}|\phi_{m\mathbf{k}}\rangle$ such that the total

number of electrons is $\sum_{m,\mathbf{k}} w_{\mathbf{k}} f_{m\mathbf{k}} \langle \phi_{m\mathbf{k}} | \phi_{m\mathbf{k}} \rangle$. While the fractional occupations $f_{m\mathbf{k}}$ are not directly compatible with the Slater determinant, they are retained in the modification of Eq. (3.6) to avoid an unmanageable expansion of the Hilbert space at each $\mathbf{k}$-point. Owing to the orthogonality of Kohn-Sham spin-orbital wavefunctions, exchange interaction energies for parallel and orthogonal spin alignments can be treated separately. Therefore, Eq. (3.6) can be systematically reformulated to accommodate periodic slab systems to be

$$\frac{4\pi\varepsilon_0}{q^2} E_0^{(1)} = \sum_a \frac{Z_a}{|\mathbf{R}_a - \mathbf{R}_H|} + \sum_{\mathbf{k}} w_{\mathbf{k}} \Big(\frac{C_{\mathbf{k}}^{\parallel} - J_{\mathbf{k}}^{\parallel}}{\det(\mathbf{S}_{\mathbf{k}})} + \frac{C_{\mathbf{k}}^{\perp} + J_{\mathbf{k}}^{\perp}}{\mathrm{perm}(\mathbf{S}_{\mathbf{k}})} \Big), \tag{3.7}$$

where the symbols $\parallel$ and $\perp$ denote parallel and orthogonal spin configurations respectively. $\det(\mathbf{S}_{\mathbf{k}})$ and $\mathrm{perm}(\mathbf{S}_{\mathbf{k}})$ correspond to the determinant and permanent of the effectively overlap matrix $\mathbf{S}_{\mathbf{k}}$. The terms $E_{\text{ion-e}}$ and $E_{\text{e-e}}$ from Eq. (3.6) have been reformulated in terms of Coulomb integral C and exchange integrals J, reflecting the physical interpretation of the interaction energies. Assuming a hydrogen nuclear charge of $Z_H = 1$, the integrals are

$$\begin{aligned} C_{\mathbf{k}}^{\parallel} = & -\frac{1}{2} \langle \phi_H | V_{\mathbf{k}}^{\text{slab}}(\mathbf{r}_e) | \phi_H \rangle \\ & + \sum_m \frac{f_{m\mathbf{k}}}{2} \left[\det(\mathbf{S}_{\mathbf{k}}) + \frac{f_{m\mathbf{k}}}{2} |\langle \phi_{m\mathbf{k}} | \phi_H \rangle|^2 \right] \Bigg[\langle \phi_{m\mathbf{k}} | V^H(\mathbf{r}_{m\mathbf{k}}) | \phi_{m\mathbf{k}} \rangle \\ & - \iint d^3\mathbf{r} d^3\mathbf{r}_e \frac{n_H(\mathbf{r}_e) n_{m\mathbf{k}}(\mathbf{r})}{|\mathbf{r} - \mathbf{r}_e|} \Bigg], \end{aligned} \tag{3.8a}$$

$$\begin{aligned} 2J_{\mathbf{k}}^{\parallel} = & -\sum_m \frac{f_{m\mathbf{k}}}{2} \Bigg\{ \langle \phi_H | \phi_{m\mathbf{k}} \rangle \langle \phi_{m\mathbf{k}} | V_{\mathbf{k}}^{\text{slab}}(\mathbf{r}_e) | \phi_H \rangle \\ & + \langle \phi_H | V^H(\mathbf{r}_{m\mathbf{k}}) | \phi_{m\mathbf{k}} \rangle \langle \phi_{m\mathbf{k}} | \phi_H \rangle - \left[\det(\mathbf{S}_{\mathbf{k}}) + \frac{f_{m\mathbf{k}}}{2} |\langle \phi_{m\mathbf{k}} | \phi_H \rangle|^2 \right] \\ & \times \iint d^3\mathbf{r} d^3\mathbf{r}_e \frac{\phi_{m\mathbf{k}}^*(\mathbf{r}) \phi_H(\mathbf{r}) \phi_H^*(\mathbf{r}_e) \phi_{m\mathbf{k}}(\mathbf{r}_e)}{|\mathbf{r} - \mathbf{r}_e|} \Bigg\}. \end{aligned} \tag{3.8b}$$

The Coulomb and exchange integrals corresponding to orthogonal spin configurations can be obtained by substituting the determinant of the overlap matrix, $\det(\mathbf{S}_{\mathbf{k}})$,

with its permanent, perm($\mathbf{S}_\mathbf{k}$). For simplicity, this thesis focuses exclusively on the spin-unpolarised case, where the occupation numbers for spin-up and spin-down states are equal, i.e., $f^{\uparrow}_{m\mathbf{k}} = f^{\downarrow}_{m\mathbf{k}}$. The ion-electron interaction potential is denoted by V. The appearance of the subscript $\mathbf{k}$ arises due to the normalisation of electronic charge at each $\mathbf{k}$ point. Further details regarding these considerations are provided in Appendix B. During the self-consistent procedure in DFT, the total electronic charge of the slab may slightly deviate from neutrality due to the variational principle. To address this, a normalisation factor is introduced such that the total charge is renormalised to match the total number of slab electrons, scaled by the ratio $\sum_m f_{m\mathbf{k}} / \sum_a Z_a$. The factor of 2 preceding the exchange integral J in Eq. (3.8b) accounts for the fact that the electron from the hydrogen atom may participate in exchange interactions with both parallel and orthogonal spin configurations. Given the spin-unpolarised assumption, the occupation numbers of spin-up and spin-down states are equal, leading to an averaged expectation value of one-half for each exchange contribution. In spin-polarised systems, however, the exchange contributions are weighted according to the occupation numbers of the respective spin channels, of which the mathematical details are omitted in this thesis because the spin-polarised systems are not the focus of this work. Furthermore, to address the singularity at the ionic core, the electron-ion interaction potential is revised using a smoothed functional form that emulates a pseudopotential, expressed as follows:

$$\frac{1}{|\mathbf{R}_a - \mathbf{r}_i|} \rightarrow \frac{6|\mathbf{R}_a - \mathbf{r}_i|^3}{7(e^{2|\mathbf{R}_a - \mathbf{r}_i|^2} + 1)} + \frac{1.03}{|\mathbf{R}_a - \mathbf{r}_i| + 0.01} e^{-\frac{0.2}{|\mathbf{R}_a - \mathbf{r}_i|^2 + 0.01}}. \tag{3.9}$$

In principle, there is no unique definition of a pseudopotential; the expression employed here is a numerical fitting with limited direct physical significance. As illustrated in Fig. 3.1, the potential decreases towards zero when the distance is less

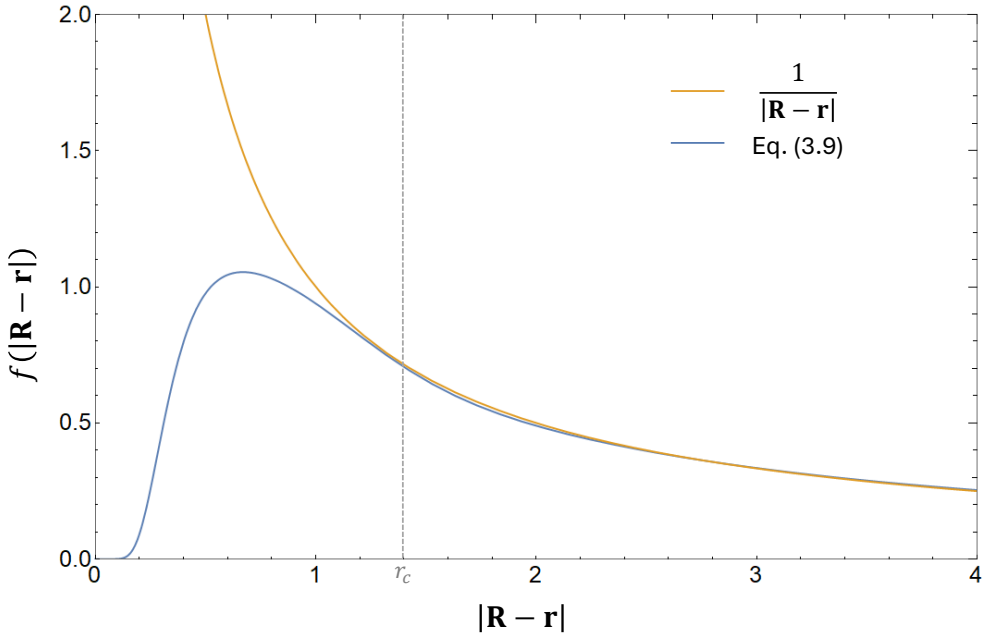

Figure 3.1: Comparison between the smoothed functions given by Eq. (3.9) for ion-electron interactions and the inverse law. The smoothed function aligns with the inverse law at distances exceeding the cutoff radius r_c, whereas it diminishes towards zero for separations less than r_c.

than the core radius, while beyond this radius it asymptotically follows the inverse-distance (Coulombic) behaviour. The incorporation of the occupation numbers $f_{m\mathbf{k}}$ in Eq. (3.7) functions as an "effective" hybridisation factor at each energy state, reflecting their contribution in a manner conceptually akin to Fock space weighting. Eq. (3.7) thus marks a successful extension from isolated system models to the DFT framework. Importantly, the formulation not only yields a quantitative measure of interaction energy but also reveals the underlying physical interpretations embedded in its constituent parameters.

In contrast to Eq. (3.4), the orbital overlaps, $1 \pm S^2$, have been generalised to the permanent and determinant of the overlapping matrix $\mathbf{S_k}$, taking the form $1 \pm \sum_m f_{m\mathbf{k}} |\langle \phi_{m\mathbf{k}} | \phi_H \rangle|^2 / 2$. Here, $\langle \phi_{m\mathbf{k}} | \phi_H \rangle$ denotes the overlapping integral between the original slab's Bloch state at band m and wavevector $\mathbf{k}$ and the electronic wave-

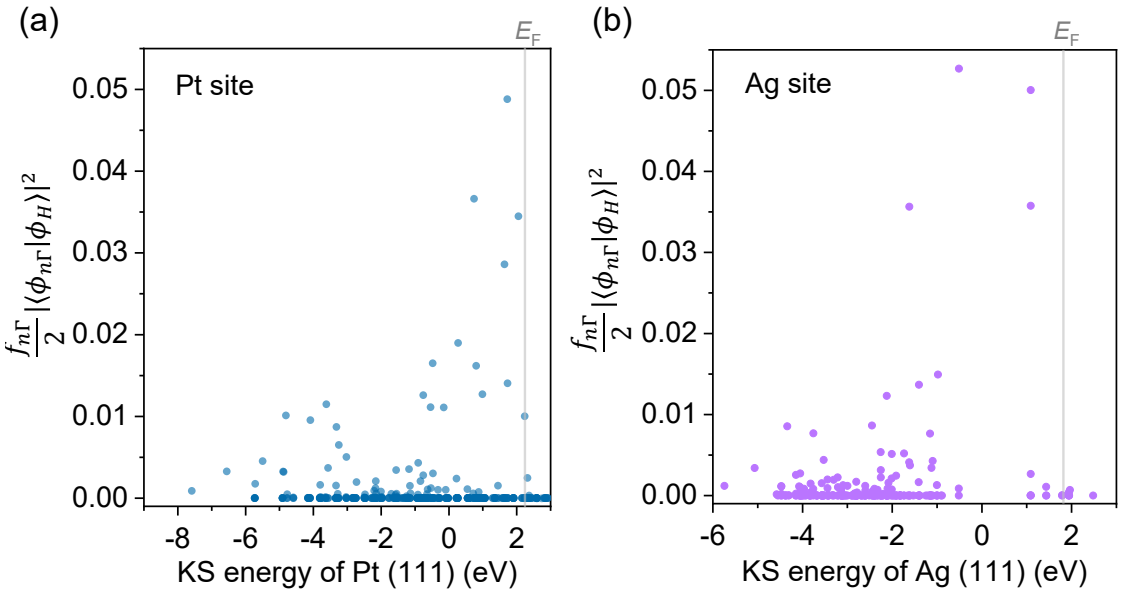

Figure 3.2: The effective overlapping integrals at each Kohn-Sham energy state of the atom sites of (a) Pt (111) and (b) Ag (111). $2 \times 2 \times 5$ atomic layers' supercells were considered. Γ points are chosen for explaination.

function of an isolated hydrogen atom. Not all electronic states contribute equally to the exchange interaction, which can be identified by the corresponding effective overlapping integrals. Fig. 3.2(a) illustrates the distribution of these integrals across the energy spectrum of Pt (111), with the Γ point selected for reference. It is well established that the surface states of Pt (111) originate predominantly from d-orbitals; thus, the magnitude of the overlapping integrals serves to quantify the contribution of d states to the overall interaction energy. The trend reveals that overlapping integrals increase as the energy approaches the Fermi level E_F, indicating that higher energy, more delocalised electrons contribute more significantly to the interaction. In contrast, Fig. 3.2(b) shows the corresponding overlap distribution for Ag (111), which has a high hydrogen adsorption free energy ($\Delta G_{\mathrm{H}*} = 1.05$ eV). Unlike Pt (111), the overlapping integrals in Ag (111) are more concentrated at lower energy levels, with only a few high-energy states contributing appreciably. The overlapping

from lower energy electrons induces higher energy is required to excite surface electrons to the Fermi level, which leads to less electron escape from the slab and lower chance in exchnaging electrons. The overlapping integrals also expose a limitation of the perturbative approach in Eq. (3.7): when $f_{m\mathbf{k}}|\langle\phi_{m\mathbf{k}}|\phi_H\rangle|^2/2 \approx 1$, the overlapping becomes too high, indicating significant electronic correlation effect. In such regimes, perturbation theory may no longer be valid, consistent with the description in Newns-Anderson model [88].

In principle, Eq. (3.7) already offers a comprehensive description of short-range interaction energy. However, accurately representing the interaction between a periodic system and an isolated one necessitates a substantially large slab size to approximate periodicity. To strike a balance between computational efficiency and accuracy, the following techniques have been considered: (*i*) To ensure the slab surface could fully adsorb the hydrogen atom, the slab dimensions were constrained to supercell sizes comparable to those used in the previous chapter's DFT calculations. (*ii*) The supercell is slightly extended to encompass the edge atoms, ensuring that the net Coulombic forces arising from the ions are balanced in both the x and y directions. Similarly, the hydrogen atoms are constrained to remain at the centre, with the slabs adjusted accordingly to maintain this positioning. (*iii*) Including cations from neighbouring cells introduces additional Coulombic contributions. To preserve charge neutrality within the supercell, external charges are disregarded by assuming that their cationic and electronic components cancel each other out. Meanwhile, the contribution of edge cations within the supercell is scaled by their packing fraction, given by $\alpha/2\pi$, where α represents the angle spanned in the xy-plane within the supercell.

3.2 Long range interaction for hydrogen adsorption

The first-order perturbation term accounts for the short-range interaction energy arising from the overlapping between the wavefunctions of the hydrogen atom and the slab. While Eq. (3.8) offers a reasonably comprehensive description of the exchange interaction, the mean-field approximation inherent in first-order perturbation theory fails to capture interaction energy stemming from local charge dispersion such as van der Waals forces caused by dipole-dipole attraction. Consequently, the second-order perturbation term, as expressed in Eq. (3.3), is required to incorporate long-range interactions and partial correlation effects. Although a complete formulation of the second-order perturbation would theoretically include band interactions with the excited states of the slab, this can be simplified by treating the contribution as a purely long-range effect, since the first-order term predominantly governs the short-range interactions.

In principle, the second-order perturbation should follow similar procedures to those outlined in the previous section. Thanks to the long-range approximation, the long-range interaction can be incorporated by modifying Eq. (3.7), setting the overlap integral to unity to reflect the non-local nature of the interaction. Under this approximation, the many-body eigenstate is reduced to the eigenstate of the hydrogen atom, $|\phi_m^H\rangle$, and the Hamiltonian for second order perturbation is accordingly reformulated as follows:

$$\begin{aligned}\frac{4\pi\varepsilon_0}{q^2}H_{\text{int}}^{(2)} = \sum_a \tilde{Z}_a\Big(\frac{1}{|\mathbf{R}_a-\mathbf{R}_H|}-\frac{1}{|\mathbf{R}_a-\mathbf{r}_e|}\Big)\\ -\int n(\mathbf{r})\Big(\frac{1}{|\mathbf{r}-\mathbf{R}_H|}-\frac{1}{|\mathbf{r}-\mathbf{r}_e|}\Big)d^3\mathbf{r},\end{aligned} \tag{3.10}$$

where $\tilde{Z}_a$ denotes the revised charge, and $n(\mathbf{r})$ represents the ground-state electron charge density of the slab, composed of $\sum_{m,\mathbf{k}} w_{\mathbf{k}} f_{m\mathbf{k}} |\langle \mathbf{r}|\phi_{m\mathbf{k}}\rangle|^2$. A detailed derivation is also provided in Appendix C. Under the long-range approximation, the second-order perturbation term becomes dependent solely on the eigenstates of the hydrogen atom, with the cationic and electronic charges of the slab effectively acting as an external electric field. Since the interaction energy of the two bodies are symmetric, the energy obtained from Eq. (3.10) also corresponds to the energy change of the slab, despite only the hydrogen atom's eigenstates being considered. Although Eq. (3.10) does not account for many-body correlation effects, the long-range approximation offers a theoretical foundation for describing physisorption. By applying a multipole expansion and incorporating multiple energy states, the second-order perturbation term can be further simplified as:

$$E_0^{(2)} \approx q^2 \sum_{m\neq 0} \frac{|\langle \phi_m^H | \mathbf{r}_{eH} \cos\theta | \phi_0^H \rangle|^2}{E_0^H - E_m^H} \Big| \frac{1}{4\pi\varepsilon_0} \nabla_{\mathbf{R}_H} \int \frac{\rho(\mathbf{r})}{|\mathbf{R}_H - \mathbf{r}|} d^3\mathbf{r} \Big|^2. \tag{3.11}$$

Here, $\rho(\mathbf{r})$ denotes the total charge density of the slab, comprising both electronic and normalised cationic contributions, expressed as $q\sum_a \tilde{Z}_a \delta^3(\mathbf{R}_a - \mathbf{r}) - qn(\mathbf{r})$. The vector $\mathbf{r}_{eH}$ represents the position of the hydrogen electron relative to the nucleus, defined by $\mathbf{R}_H - \mathbf{r}_e$, while θ denotes the angle between $\langle \phi_m^H | \mathbf{r}_{eH} | \phi_0^H \rangle$ and the vector within the modulus squared term. A detailed derivation is provided in Appendix C. The energy denominator, representing the difference between excited and ground state energies, is always negative, which indicates that this second order interaction term is inherently attractive. The integral within the modulus squared captures the electrostatic potential arising from the slab, and applying the gradient operator yields the corresponding electric field at the hydrogen nucleus position $\mathbf{R}_H$. This highlights that, although the slab remains overall charge-neutral, spatial deviations

in charge distribution give rise to a local electric field near the surface, inducing a long-range interaction. Interestingly, Eq. (3.11) shows that the electric field experienced by the hydrogen atom depends only on the position of its nucleus, not the electron.

Summing over all excited states of a hydrogen atom is computationally demanding and offers limited physical insight; hence, appropriate approximations is applied to constrain the solution to a manageable range. One such approach involves decoupling the numerator and denominator as follows [102]:

$$\begin{aligned}\sum_{m\neq 0}\frac{|\langle\psi_m^{(0)}|\mathbf{r}|\phi_0^{(0)}\rangle|^2}{E_0^{(0)}-E_m^{(0)}} &\sim \sum_{\text{all } m}|\langle\psi_m^{(0)}|\mathbf{r}|\phi_0^{(0)}\rangle|^2\sum_{m\neq 0}\frac{1}{E_0^{(0)}-E_m^{(0)}}\\ &=\sum_{m\neq 0}\frac{\langle\psi_0^{(0)}|r^2|\psi_0^{(0)}\rangle}{E_0^{(0)}-E_m^{(0)}}\leq\frac{\langle\psi_0^{(0)}|r^2|\psi_0^{(0)}\rangle}{E_0^{(0)}-E_1^{(0)}}.\end{aligned} \tag{3.12}$$

Exploiting the negative definiteness of the second-order perturbation term, the expression can be bounded by considering only its first excited state. This approximation is commonly employed in estimating the hydrogen atom's polarisability, α_H, in the context of the Stark effect. Consequently, Eq. (3.11) further simplifies to

$$E_0^{(2)}\approx q^2\frac{\langle\phi_0^H|r_{eH}^2\cos^2\theta|\phi_0^H\rangle}{E_0^H-E_1^H}\left|\frac{1}{4\pi\varepsilon_0}\nabla_{\mathbf{R}_H}\int\frac{\rho(\mathbf{r})}{|\mathbf{R}_H-\mathbf{r}|}d^3\mathbf{r}\right|^2=-\frac{1}{2}\alpha_H|\mathbf{E}|^2. \tag{3.13}$$

Thus, the polarisability α_H is governed by the square of the expectation value of the hydrogen atom's dipole moment. This implies that a local electric field induces polarisation within the hydrogen atom, resulting in an induced dipole. In this approximation, the energy denominator considers only the ground and first excited states of the hydrogen atom, with the energy difference evaluated as -6.27 eV, based on DFT calculations. The derivative of the integral results in a distance dependence of the power of -3, and the sqaure of the electric field leads to an overall interaction energy scaling with the power of -6. This behaviour is consistent with the

long-range characteristics of the Lennard-Jones potential. Accordingly, Eq. (3.13) can be interpreted as a generalised form of long-range interaction, extending from atom-atom coupling to the interaction between a periodic system and an isolated hydrogen atom. The total interaction energy associated with hydrogen adsorption is given by the combined contributions of Eq. (3.7) and Eq. (3.13).

3.3 Theoretical relations of hydrogen adsorption and surface states

Theoretical models for hydrogen adsorption have been formulated using perturbation theory, establishing a foundational linkage between the intrinsic electronic properties of the slab and the resulting interaction energy. These expressions exhibit consistency with the Lennard-Jones potential at the piecewise scale and extend the concept to describe interactions between periodic systems and isolated entities. Notably, the derived models are founded entirely on first-principles calculations, in contrast to the empirical fitting methods employed in the conventional Lennard-Jones approach. If the theoretical model could be validated, it is expected that the interaction between the hydrogen atom and the (topological) surface states can be rigorously characterised through mathematical analysis. A deeper understanding of hydrogen adsorption, derived from its intrinsic wave-like properties, offers a compelling avenue for bridging topological theory and even surface science frameworks with adsorption phenomena. This connection could provide valuable insights into the role of quantum states in governing surface interactions.

To assess the validity of the proposed model, the interaction energies com-

puted from Eq.(3.7) and Eq.(3.13) are compared against results obtained via DFT. However, the total energy of a system in DFT framework does not equate to a simple summation of the Kohn-Sham eigenvalues. Corrections and adjustments such as those involving exchange-correlation energies and the double-counting correction in projector augmented-wave (PAW) methods contribute significantly to the final energy value. Nonetheless, quantities derived from the Kohn-Sham eigenvalues, including the density of states, spin textures and band structures, remain essential for understanding the coupling mechanisms between the hydrogen atom and the slab. As illustrated in Eq. (1.18), variations in the Kohn-Sham eigenvalues are closely correlated with changes in the system's total energy, and thus, with the binding energy of the adsorbed hydrogen.

The total eigenvalues of the Kohn-Sham wavefunctions for the ground state are calculated using the expression $E^{\mathrm{KS}} = \sum_{m\mathbf{k}} w_{\mathbf{k}} f_{m\mathbf{k}} E_m^{\mathrm{KS}}$, without aligning the energy levels to the Fermi energy. The difference in Kohn-Sham eigenvalues is determined by

$$\Delta E^{\mathrm{KS}} = E_{\mathrm{H}*}^{\mathrm{KS}} - E_{*}^{\mathrm{KS}} - E_{\mathrm{H}}^{\mathrm{KS}}. \tag{3.14}$$

This result remains effective even when $E_{\mathrm{H_2}}^{\mathrm{KS}}/2$ is used in place of $E_{\mathrm{H}}^{\mathrm{KS}}$, because the hydrogen atom is isolated and its eigenvalue contribution is only a fixed constant. In DFT analysis, emphasis is placed on the trend and correlation between the eigenvalue differences obtained directly from simulations and the predictions of the theoretical model, rather than on the absolute numerical values. Consequently, the precise eigenvalue of the hydrogen atom is not critical to the qualitative agreement between theory and simulation. Fig. 3.3 illustrates the correlation between the Kohn-Sham energy changes ΔE^{KS} and the interaction energies derived from the

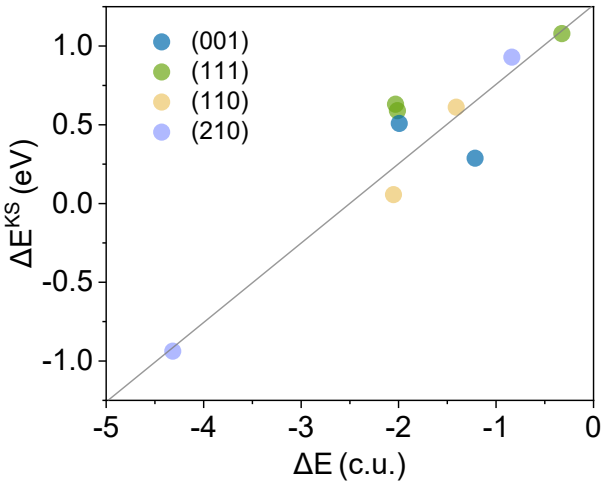

Figure 3.3: Correlation between the Kohn-Sham energy change, calculated via Eq.(3.14), and the theoretical interaction energy obtained from the sum of Eq.(3.7) and Eq. (3.13) for the benchmark catalyst Pt, across various facets and adsorption sites. The unit "c.u." refers to the conventional energy unit used in this section, where 1 [c.u.] = 14.4 [eV].

theoretical model, specifically the combined contributions of Eqs. (3.7) and (3.13), for the benchmark catalyst Pt across various crystallographic facets and adsorption sites. The results demonstrate a linear relationship, thereby supporting the validity of the theoretical model. Nonetheless, limitations remain evident. Despite the linear trend, the interaction energies predicted by the model are consistently larger than the corresponding values of ΔE^{KS}; also, the connection between the theoretical interaction energy and the actual hydrogen adsorption energy requires further investigation and clarification.

To facilitate a deeper understanding of the relationship between topological surface states and hydrogen adsorption, the theoretical model has been applied to the TaAs family of compounds. Particular emphasis is placed on the (001) facets, as these surfaces lie along crystallographic directions lacking parity inversion symmetry, resulting in a high density of Fermi arcs and a pronounced presence of topological surface states. Notably, the conductive topological surface states are typically

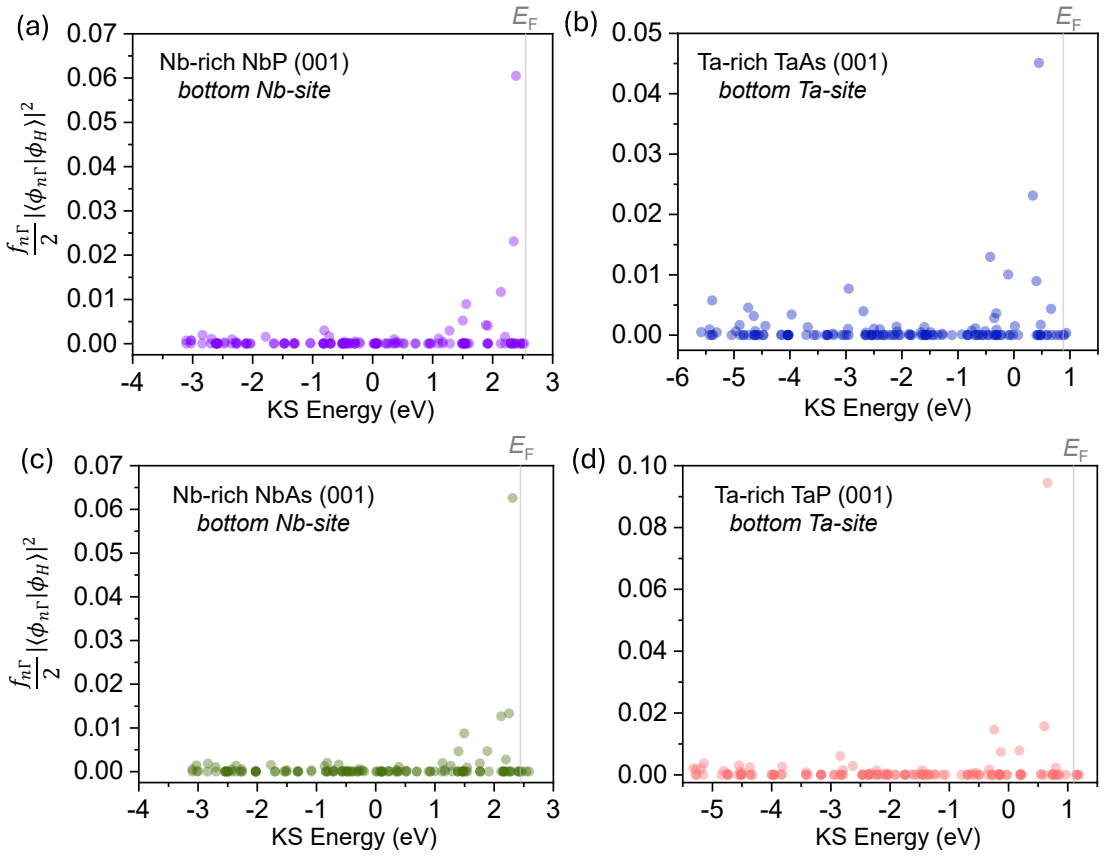

Figure 3.4: Effective overlap integrals corresponding to each Kohn-Sham energy state for the metal-rich (001)-bottom facets of (a) NbP, (b) TaAs, (c) NbAs and (d) TaP. The hydrogen adsorption sites are positioned atop the metallic atoms, with the Γ point selected for illustrative perspective. $3 \times 3 \times 8$ atomic layers' supercells were considered.

located near the Fermi level, making them prime candidates for interaction analysis. To evaluate their influence, effective overlap integrals of each Kohn-Sham state have been calculated. As discussed in the previous chapter, the metal-rich (001)-bottom facets have shown potential as efficient catalysts; therefore, these surfaces were selected as examples, with the Γ point used for illustrative purposes. The corresponding results are presented in Fig. 3.4. Across all four studied structures, significant overlap contributions are observed only for bands near the Fermi energy, highlighting the role of topological surface states in facilitating hydrogen adsorption. In contrast to transition metals, where a broad range of delocalised states contribute to surface interactions, topological surface states are more limited in

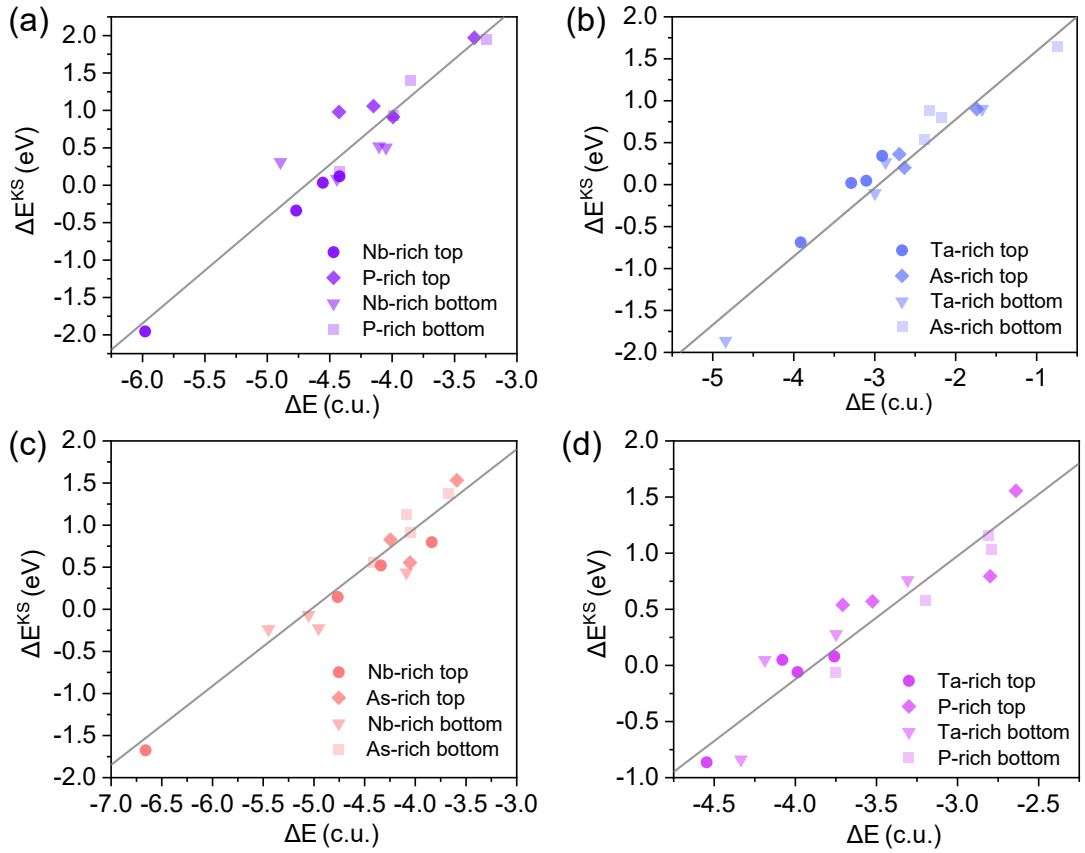

Figure 3.5: Correlation between the Kohn-Sham energy change, calculated via Eq.(3.14), and the theoretical interaction energy obtained from the sum of Eq.(3.7) and Eq. (3.13) for the (001)-bottom facets of (a) NbP, (b) TaAs, (c) NbAs and (d) TaP. $3 \times 3 \times 8$ atomic layers' supercells were considered. The unit "c.u." refers to the conventional energy unit used in this section, where 1 [c.u.] = 14.4 [eV].

number. However, this does not imply diminished catalytic performance. According to the Newns-Anderson model [88] and the theoretical framework underpinning the *d*-band centre theory [12], the interaction energy is primarily governed by single-electron exchange processes. Therefore, the presence of significant overlap integrals near the Fermi level is sufficient to induce meaningful interaction energy and suggests optimal local potential. This effective overlapping integrals give an edvidence that the emergence of topological surface states could still give rise to non-trivial Kohn-Sham eigenstates $|\phi_{m\mathbf{k}}\rangle$ near the surface, which substantially influence the Coulomb and exchange integrals defined in Eqs. (3.8a) and (3.8b).

Fig. 3.5 presents the correlation between the Kohn-Sham energy change ΔE^{KS} and the interaction energies predicted by the theoretical model obtained from the combined contributions of Eqs. (3.7) and (3.13) across the (001) facets of the TaAs family of compounds. The results demonstrate a nearly linear relationship, offering further support for the validity of the proposed model. However, minor discrepancies are evident upon closer comparison. In addition to the issue of predicted interaction energies consistently exceeding the computed ΔE^{KS}, the slopes of the linear trends vary notably across different materials. Furthermore, since the derivation was based on spin-unpolarised systems, the interaction contributions from parallel and orthogonal spin configurations would differ if spin polarisation or spin-orbit coupling were taken into account. These highlight the need for further refinement and investigation of the theoretical framework.

Despite these constraints, the model remains compelling. It establishes a direct mathematical relationship between the slab's intrinsic electronic characteristics and the Kohn-Sham energy variation ΔE^{KS}, which is expected to correlate closely with the hydrogen adsorption energy $\Delta E_{\mathrm{H}*}$. Current descriptors typically rely on empirical approximations or statistical correlations to infer the interaction energy at active sites. In contrast, this theoretical framework is derived rigorously from the first-principle, offering a direct and approximation-free depiction of how the slab's electronic structure governs its interaction with hydrogen. As such, the model is applicable across a broad range of materials in principle, though further validation is necessary to establish its generality. Moreover, due to the spatial dependence of the wavefunctions, the model imposes no constraints on adsorption geometry, enabling the analysis of site-specific adsorption effects as illustrated in Figs. 3.3 and 3.5. This

framework holds strong potential to accelerate catalyst discovery and design through predictive mathematical analysis, reducing reliance on empirical trial-and-error approaches.

3.4 Conclusion

Although several statistical models have been proposed to elucidate the relationship between the intrinsic catalytic properties and the hydrogen adsorption free energy $\Delta G_{\mathrm{H}*}$, many are constrained by dataset-specific assumptions and lack a robust theoretical foundation. This limits their capacity to fully explain the adsorption mechanism, particularly in relation to surface properties such as topological surface states. To resolve this gap, a theoretical model for hydrogen adsorption has been developed from first principles – the many-body Schrödinger equation. Using perturbation theory, the first-order perturbation term describes short-range interactions arising from electron exchange Beyond the conventional Slater determinant framework, this approach incorporates occupation numbers and "effective" hybridisation, yielding expressions that align with the exchange interaction energy found in hydrogen molecules, but generalised for interactions between periodic systems and isolated species. However, the mean-field approximation used in the first-order perturbation fails to account for interactions originating from charge dislocations. To overcome this limitation, a second-order perturbation term is introduced. By applying a long-range approximation, the formulation is simplified while retaining its physical relevance. This second-order term reveals that the interaction arises from the local electric field generated by displaced charges, which subsequently polarises the hydrogen atom, producing a dipole-dipole interaction.

The mathematical framework offers supplementary insights, such as identifying the specific electronic bands contributing to coupling and bonding states by observing through overlap integrals. The validity of the theoretical model has been confirmed by comparing its predicted interaction energies with the Kohn-Sham eigenvalue differences derived from DFT calculations. This model has been applied to the (001) facets of TaAs family compounds across various adsorption sites, revealing a tangible contribution from topological surface states to hydrogen adsorption. It is, however, acknowledged that Kohn-Sham eigenstates do not represent the true many-body eigenstates. Therefore, the energies predicted from the combined expressions of Eq. (3.13) are comparable only with the sum of Kohn-Sham eigenvalues rather than the exact total energy. Despite this limitation, Eq. (1.18) suggests a close relationship between the Kohn-Sham eigenvalue difference ΔE^{KS} and the hydrogen adsorption energy $\Delta E_{\mathrm{H}*}$. Accordingly, the theoretical model is anticipated to offer a quantitative estimation of $\Delta E_{\mathrm{H}*}$, thereby opening a new gateway for mathematically investigating the relationship between surface properties and hydrogen adsorption. This framework not only enhances predictive capabilities, but also bridges quantum surface science with adsorption phenomena, paving the way for deeper insights into material design and catalytic performance.

Chapter 4

Summary

The hydrogen evolution reaction (HER) represents a promising avenue for clean and sustainable energy generation. Owing to the high energy barrier inherent to this reaction, the development of efficient electrocatalysts remains an urgent research priority. Although noble metals such as platinum and palladium have demonstrated exceptional catalytic performance in HER, their scarcity and high cost pose significant obstacles to large-scale commercial deployment. As a result, topological semimetals have emerged as potential alternatives, owing to their robust electronic surface states. Recent theoretical and experimental studies have indicated the feasibility of employing topological materials as HER catalysts. However, the majority of investigations have concentrated on surface facets oriented along directions lacking parity inversion symmetry, with performance assessed primarily via the Gibbs free energy change associated with hydrogen adsorption.

In this thesis, multiple facets of TaAs family compounds have been examined to evaluate the influence of surface characteristics on HER activity. In addi-

tion to Gibbs free energy, alternative descriptors are introduced to enable a more comprehensive assessment of catalytic performance. Nonetheless, the fundamental relationship between surface electronic states and hydrogen adsorption energy remains poorly understood, impeding the rational design of topological catalysts. To bridge this gap, a mathematical model has been derived from first principles, aiming to establish a quantitative connection between topological surface states and the hydrogen binding energy.

In chapter 1, the overarching context of the HER, the fundamental principles of topological semimetals and the theoretical methodologies employed in this thesis are introduced. Given the volcano-shaped relationship between catalytic current density and the Gibbs free energy of hydrogen adsorption, the latter emerges as an effective descriptor for assessing catalytic performance. To better predict this descriptor, the *d*-band theory and its underlying framework are briefly reviewed. Additional parameters – water adsorption energy, the energy barrier for water dissociation and surface energy – are proposed as complementary descriptors in evaluating HER activity. Subsequently, the core concepts related to topological semimetals and recent advances in topological catalysts are reviewed. Unlike the conventional *d*-band theory, the "surface density of states" has been suggested as a potential descriptor for HER effectiveness in topological materials. However, its lack of a clear theoretical foundation renders its reliability uncertain. Finally, the theoretical approaches used throughout this thesis – density functional theory and the Wannier functions – are outlined. The selected software packages and corresponding computational parameters are also detailed.

In Chapter 2, the topological surface states across multiple facets of TaAs

family compounds are systematically examined, and their HER catalytic performance is evaluated using four key descriptors. The findings reveal that topological surface states can emerge on various crystallographic facets, even those not oriented along directions that lack parity inversion symmetry. When all four descriptors are put in equal importance and compared against the benchmark catalyst Pt (111), many facets exhibit comparable or even superior HER performance, as evidenced by their radar chart profiles. Notably, the metal-rich (001)-bottom and (111) facets display optimal energy values across all four descriptors, highlighting their potential as promising candidates for efficient HER catalysis.

In chapter 3, a first-principles theoretical framework for hydrogen adsorption energy has been established, aimed at elucidating the relationship between topological surface states and adsorption behaviour. Beginning with the many-body Schrödinger equation and employing perturbation theory, the model distinguishes short-range interaction energies—captured through the first-order perturbation term—from long-range interactions, addressed by the second-order term. The "effective" overlap integrals quantify the electron exchange capability between the (topological) surface states and the hydrogen electron. In TaAs family compounds, these overlap contributions predominantly appear near the Fermi energy, suggesting that topological surface states may facilitate electron exchange with hydrogen adsorbates. The derived mathematical model is applied across TaAs compounds. Although Kohn-Sham eigenstates are not the true eigenstates of the many-body Schrödinger equation, the corresponding Kohn-Sham energy variations are used for comparison. The near-linear correlation observed between the predicted interaction energies and the Kohn-Sham energy changes supports the validity.

Appendix A

First order perturbation in hydrogen adsorption

As illustrated in Fig. 1.1(b), the interaction energy between the catalyst and the adsorbed hydrogen arises primarily from electron exchange processes. Mathematically, this interaction is incorporated into the system via a modified Hamiltonian, denoted as Eq. (3.1). In particular, Eq. (3.2c) represents the interaction Hamiltonian, capturing the coupling between the electronic states of the hydrogen atom and those of the catalyst surface:

$$H_{\text{int}} = \frac{q^2}{4\pi\varepsilon_0}\left(\sum_a \frac{Z_a Z_H}{|\mathbf{R}_a - \mathbf{R}_H|} - \sum_a \frac{Z_a}{|\mathbf{R}_a - \mathbf{r}_e|} - \sum_i \frac{Z_H}{|\mathbf{R}_H - \mathbf{r}_i|} + \sum_i \frac{1}{|\mathbf{r}_i - \mathbf{r}_e|}\right), \tag{A.1}$$

which will be tackled using perturbation theory. Assuming that the individual solutions to the many-body Hamiltonians of the slab and the hydrogen atom – Eqs. (3.2a) and (3.2b) – are known, the composite system can be treated perturbatively. Owing to the antisymmetric nature of many-body wavefunctions, the "unperturbed"

wavefunction of the combined system can be constructed as a Slater determinant:

$$\Psi_0^{(0)}(\{\mathbf{r}_i\}) = \sum_{\sigma} \varepsilon_{\sigma_1\sigma_2\ldots\sigma_{N+1}} \prod_{i}^{N+1} \phi_{\sigma_i}(\mathbf{r}_i), \tag{A.2}$$

where ε used here denotes the Levi-Civita symbol. The first N one-body spin-orbital wavefunctions $\phi_{\sigma_i}(\mathbf{r}_i)$ correspond to the eigenfunctions derived from the slab Hamiltonian, while the final wavefunction represents that of a hydrogen atom. It is important to note that the eigenstates of the slab and the hydrogen atom are treated as isolated systems. In other words, the linear combination of atomic orbitals (LCAO) method is not employed between the eigenstates of the slab and those of the hydrogen atom. This is a deliberate choice, aimed at pursuing an analytical expression for the interaction energy, which would be obscured by the complexities introduced by LCAO. Although the slab's single-electron eigenstates are known to be orthonormal amongst themselves, this orthonormality does not extend to the eigenstates of the slab and hydrogen atom taken together. Therefore, a normalisation factor is introduced:

$$\begin{aligned}
\langle\Psi_0^{(0)}|\Psi_0^{(0)}\rangle &= \left(\prod_{i=1}^{N+1}\int d^3\mathbf{r}_i\right)\left[\sum_{\tau}\varepsilon_{\tau_1\tau_2\ldots\tau_{N+1}}\prod_{i}^{N+1}\phi_{\tau_i}(\mathbf{r}_i)\right]\left[\sum_{\sigma}\varepsilon_{\sigma_1\sigma_2\ldots\sigma_{N+1}}\prod_{i}^{N+1}\phi_{\sigma_i}(\mathbf{r}_i)\right] \\
&= \sum_{\tau,\sigma}\varepsilon_{\tau_1\tau_2\ldots\tau_{N+1}}\varepsilon_{\sigma_1\sigma_2\ldots\sigma_{N+1}}\prod_{i=1}^{N+1}\langle\phi_{\tau_i}|\phi_{\sigma_i}\rangle \\
&= (N+1)!\,\det(\mathbf{S}),
\end{aligned}$$

where $\mathbf{S}$ denotes the overlap matrix, and the summations over τ and σ represent summing over all permutations. In this particular scenario, the elements of $\mathbf{S} = [\langle\phi_i|\phi_j\rangle]$ take the value of 1 when $i = j$, and 0 when $i \neq j$ for all $i, j \leqslant N$. For cases where either i or j equals $N+1$, the elements correspond to $\langle\phi_i|\phi_H\rangle$ or $\langle\phi_H|\phi_j\rangle$. As a result, the determinant of the overlap matrix is given by $\det(\mathbf{S}) = 1 - \sum_i |\langle\phi_H|\phi_i\rangle|^2$. Importantly, Eq. (A.2) guarantees that the zeroth-order term in the perturbation

expansion equals the sum of the individual energies of the slab and the hydrogen atom. Given that the original eigenvalues and eigenstates are assumed to be known, this equality can be readily verified by assuming that the slab Hamiltonian can be expressed as a direct sum of the Hamiltonians of the slab and the hydrogen atom:

$$\begin{aligned}\sum_{i}^{N+1}\frac{\langle\Psi_0^{(0)}|h_i|\Psi_0^{(0)}\rangle}{\langle\Psi_0^{(0)}|\Psi_0^{(0)}\rangle} &= \frac{1}{(N+1)!\,\det(\mathbf{S})}\sum_{\tau,\sigma}\varepsilon_{\tau_1\ldots\tau_{N+1}}\varepsilon_{\sigma_1\ldots\sigma_{N+1}}\prod_{i=1}^{N+1}\langle\phi_{\tau_i}|h_{\sigma_i}\phi_{\sigma_i}\rangle \\ &= \sum_{i}^{N+1}\epsilon_i \\ &= E_{\text{slab}} + E_{\text{ads}},\end{aligned} \tag{A.3}$$

where h_i is the decomposed Hamiltonian. Once the zeroth order term is verified to correspond with the total energy of the slab and the hydrogen atom, attention may be turned to the first order perturbation. This term is equivalent to the mean-field approximation:

$$\begin{aligned}\langle\Psi_0^{(0)}|H_{\text{int}}|\Psi_0^{(0)}\rangle = \frac{q^2}{4\pi\varepsilon_0}\langle\Psi_0^{(0)}|\sum_a\left(\frac{Z_aZ_H}{|\mathbf{R}_a-\mathbf{R}_H|}-\frac{Z_a}{|\mathbf{R}_a-\mathbf{r}_e|}\right) \\ +\sum_i^N\left(-\frac{Z_H}{|\mathbf{R}_H-\mathbf{r}_i|}+\frac{1}{|\mathbf{r}_i-\mathbf{r}_e|}\right)|\Psi_0^{(0)}\rangle\end{aligned}, \tag{A.4}$$

where q, ε_0 and Z are the electron charge, vacuum permittivity and atomic number respectively. Here, the subscripts $a, b, c, \ldots$ and $i, j, k, \ldots$ denote indices for atoms and electrons respectively, while the symbols H and e are used to explicitly refer to the hydrogen atom and its associated electron. The position vectors of atoms and electrons are represented by $\mathbf{R}$ and $\mathbf{r}$ respectively. The first term in the expression may be disregarded as it constitutes a constant. The second and third terms, however, correspond to the interaction energies between the ions and electrons of the two isolated systems. By applying a procedure analogous to that used in Eq. (A.3), and employing the same assumptions regarding the elements of the overlap matrix

S, the second and third terms can be expressed as follows:

$$\sum_a \langle \Psi_0^{(0)} | \frac{Z_a}{|\mathbf{R}_a - \mathbf{r}_e|} | \Psi_0^{(0)} \rangle = (N+1)! \sum_a \left(\langle \phi_H | \frac{Z_a}{|\mathbf{R}_a - \mathbf{r}_e|} | \phi_H \rangle - \sum_i^N \langle \phi_H | \phi_i \rangle \langle \phi_i | \frac{Z_a}{|\mathbf{R}_a - \mathbf{r}_e|} | \phi_H \rangle \right),$$

$$\sum_i^N \langle \Psi_0^{(0)} | \frac{Z_H}{|\mathbf{R}_H - \mathbf{r}_i|} | \Psi_0^{(0)} \rangle = (N+1)! \sum_i^N \left\{ \langle \phi_i | \frac{Z_H}{|\mathbf{R}_H - \mathbf{r}_i|} | \phi_i \rangle \left[\det(\mathbf{S}) + |\langle \phi_i | \phi_H \rangle|^2 \right] - \langle \phi_H | \frac{Z_H}{|\mathbf{R}_H - \mathbf{r}_i|} | \phi_i \rangle \langle \phi_i | \phi_H \rangle \right\}.$$

Here, the step-by-step derivation is omitted for brevity. The fourth term presents a subtle challenge, as it represents the interaction energy between electrons originating from the slab and those from the hydrogen atom. In principle, two cofactors should be incorporated to account for the mixed contributions from these distinct subsystems. However, due to the structure of the overlap matrix, the cofactor corresponding to $[\mathbf{S}]_{N+1,N+1}$ evaluates to unity. As a result, the fourth term is:

$$\sum_i^N \langle \Psi_0^{(0)} | \frac{1}{|\mathbf{r}_i - \mathbf{r}_e|} | \Psi_0^{(0)} \rangle = (N+1)! \sum_i^N \iint d^3\mathbf{r}_i d^3\mathbf{r}_e \left[\det(\mathbf{S}) + |\langle \phi_i | \phi_H \rangle|^2 \right] \times \left[\frac{n_H(\mathbf{r}_e) n_i(\mathbf{r}_i)}{|\mathbf{r}_i - \mathbf{r}_e|} - \frac{\phi_i^*(\mathbf{r}_i) \phi_i(\mathbf{r}_e) \phi_H^*(\mathbf{r}_e) \phi_H(\mathbf{r}_i)}{|\mathbf{r}_i - \mathbf{r}_e|} \right].$$

Therefore, applying the appropriate normalisation condition, the first-order perturbation can be formulated as shown in Eq. (3.6), where each term is:

$$E_{\text{ion-ion}} = \sum_a \frac{Z_a Z_H}{|\mathbf{R}_a - \mathbf{R}_H|} \tag{A.5a}$$

$$E_{\text{ion-e}} = \frac{1}{\det(\mathbf{S})} \left\{ \langle \phi_H | \sum_a \frac{Z_a}{|\mathbf{R}_a - \mathbf{r}_e|} | \phi_H \rangle - \sum_i^N \langle \phi_H | \phi_i \rangle \langle \phi_i | \sum_a \frac{Z_a}{|\mathbf{R}_a - \mathbf{r}_e|} | \phi_H \rangle + \sum_i^N \langle \phi_i | \frac{Z_H}{|\mathbf{R}_H - \mathbf{r}_i|} | \phi_i \rangle \left[\det(\mathbf{S}) + |\langle \phi_i | \phi_H \rangle|^2 \right] - \sum_i^N \langle \phi_H | \frac{Z_H}{|\mathbf{R}_H - \mathbf{r}_i|} | \phi_i \rangle \langle \phi_i | \phi_H \rangle \right\} \tag{A.5b}$$

$$E_{\text{e-e}} = \frac{1}{\det(\mathbf{S})} \sum_{i}^{N} \iint d^3\mathbf{r}_i d^3\mathbf{r}_e \left[\det(\mathbf{S}) + |\langle\phi_i|\phi_H\rangle|^2\right] \times \left[\frac{n_H(\mathbf{r}_e) n_i(\mathbf{r}_i)}{|\mathbf{r}_i - \mathbf{r}_e|} - \frac{\phi_i^*(\mathbf{r}_i)\phi_i(\mathbf{r}_e)\phi_H^*(\mathbf{r}_e)\phi_H(\mathbf{r}_i)}{|\mathbf{r}_i - \mathbf{r}_e|}\right] \tag{A.5c}$$

Appendix B

Hydrogen adsorption model in DFT

Eq. (3.6) presents the general formulation of hydrogen adsorption derived via perturbation theory. To validate the accuracy of this theoretical model, its predictions must be compared against computational results. In this thesis, density functional theory (DFT) has been adopted for this purpose. The fundamental premise of Eq. (3.6) is that the wavefunctions of the isolated systems are already known, whether in analytical or numerical form. In the context of Kohn-Sham DFT, the Kohn-Sham orbitals obtained from the DFT calculations serve as inputs to the perturbative framework. As mentioned in the main text, Kohn-Sham DFT partitions the Hilbert space into multiple subspaces according to the wave vector $\mathbf{k}$, such that $\mathcal{H} = \mathcal{H}_{\mathbf{k}_1} \bigoplus \mathcal{H}_{\mathbf{k}_2} \bigoplus \cdots$. These subspaces are characterised by differing weightings and are not necessarily orthogonal to one another. Nevertheless, since the perturbative Hamiltonian does not explicitly depend on momentum, the individual Hilbert

subspaces can be treated independently. Accordingly, the total Kohn-Sham energy for a spin-unpolarised system is given by $E = \sum_{m,\mathbf{k}} w_{\mathbf{k}} f_{m\mathbf{k}} E_{m\mathbf{k}}$, where $w_{\mathbf{k}}$ denotes the weighting factor associated with each $\mathbf{k}$-point, and $f_{m\mathbf{k}}$ is the occupation number of the m-th Kohn-Sham wavefunction at $\mathbf{k}$.

A key divergence between the theoretical model and DFT lies in the treatment of occupation numbers. Within the framework of the Slater determinant, each orthonormal single-electron spin-orbital wavefunction has a strictly binary occupation (either 0 or 1). By contrast, DFT allows for fractional occupation numbers. To accommodate this discrepancy, occupation numbers are incorporated into the model after the formulation of Eq. (3.6), rather than being embedded from the beginning. Despite the system being spin-unpolarised overall, spin coupling still needs to be accounted, similar to the presence of a single electron in the hydrogen atom. This electron can couple either with parallel or orthogonal spin to the electrons occupying each energy state in the slab. For simplicity, the many-body wavefunctions are considered separately for each coupling case. In the scenario of parallel spin coupling, the spin component of the wavefunction is symmetric, which necessitates an antisymmetric spatial component to preserve the overall fermionic antisymmetry. Accordingly, the "unperturbed" total wavefunction for parallel spin coupling is given by:

$$\Psi_{\mathbf{k}}^{(0)}(\{\mathbf{r}_i\}) = \sum_{\sigma} \varepsilon_{\sigma_1 \ldots \sigma_M \sigma_{M+1}} \prod_{i}^{N+1} \phi_{\sigma_i}(\mathbf{r}_i). \tag{B.1}$$

Here, M represents the total number of occupied energy states in the slab, and the final component corresponds to the hydrogen atom's wavefunction. The normalisation factor is given by $(M+1)!\,\det(\mathbf{S})$, which accounts for the combined system of $M+1$ electrons. In the case of orthogonal spin coupling, the situation requires

more careful consideration. Although the slab's orbital wavefunction is antisymmetric with respect to its own electrons, each individual electron wavefunction must be symmetrised with that of the hydrogen atom to preserve the correct spin configuration. This reflects the fact that the spin part of the wavefunction is antisymmetric, necessitating a symmetric orbital component to maintain the overall fermionic antisymmetry. As a result, the total "unperturbed" wavefunction for orthogonal spin coupling is given by:

$$\Psi_{\mathbf{k}}^{(0)}(\{\mathbf{r}_i\}) = \sum_{\sigma} \varepsilon_{\sigma_1 \ldots \sigma_M} \prod_{i}^{M} \phi_{\sigma_i}(\mathbf{r}_i)\phi_{M+1}(\mathbf{r}_{M+1}) + \sum_{j}^{N} \left[\sum_{\sigma} \varepsilon_{\sigma_1 \ldots \sigma_j \ldots \sigma_M} \prod_{i \neq j}^{M} \phi_{\sigma_i}(\mathbf{r}_i)\phi_{\sigma_j}(\mathbf{r}_{M+1}) \right] \phi_{M+1}(\mathbf{r}_j) \quad . \tag{B.2}$$

The corresponding normalisation factor is $(M+1)!\ \mathrm{perm}(\mathbf{S})$, where $\mathrm{perm}(\mathbf{S})$ denotes the permanent of the overlap matrix $\mathbf{S}$. By systematically rearranging the terms in Eq. (A.5) and incorporating the occupation numbers, Eq. (3.8) is obtained. It is worth noting that only half of the total Coulomb and exchange interactions are captured in Eq. (3.8). This is due to the symmetric treatment of parallel and orthogonal spin coupling: each exchange configuration contributes equally, resulting in an effective halving of the interaction energy in the final expression.

Appendix C

Long range approximation of hydrogen adsorption

The first-order perturbative term provides a mean-field approximation that effectively captures the dominant short-range interactions. However, that treatment cannot account for interactions arising from charge deviation, such as multipole effects, which plays a significant role in the long-range regime. As a result, the inclusion of the second-order perturbation term becomes essential for a more complete description of the interaction energy. In principle, the second-order perturbation must incorporate the band structure of the slab, as these contributions are relevant to the long-range coupling between the slab and the hydrogen atom. Given the extended nature of this interaction, the full Hamiltonian may be approximated by the expression given in Eq.(3.10). Consequently, the second-order perturbative energy is formulated as shown in Eq.(3.11). The full derivation supporting this approximation is presented in detail in this appendix.

In the long-range limit, the probability of the hydrogen atom's electron being found within the spatial region of the slab becomes negligibly small, and the same applies to slab electrons occupying the vicinity of the hydrogen atom. Owing to this spatial separation, the "unperturbed" many-body wavefunction described in Eq. (3.5) can be simplified to be the form of Hartree product:

$$\Psi_0^{(0)}(\{\mathbf{r}_i\}) = \sum_{\sigma} \varepsilon_{\sigma_1\sigma_2\ldots\sigma_N} \prod_{i}^{N} \phi_{\sigma_i}(\mathbf{r}_i)\phi_H(\mathbf{r}_e). \tag{C.1}$$

Since the hydrogen atom and the slab share the same interaction energy, the band interaction embodied in the second-order perturbation term may be interpreted as the excitation energy of the hydrogen atom transitioning from its ground state to its first excited state, while the slab's energy is treated as unchanged. Accordingly, the second-order perturbative energy takes the following form:

$$\sum_{m\neq 0} \frac{|\langle \Psi_m^{(0)}|H_{\text{int}}|\Psi_0^{(0)}\rangle|^2}{E_m - E_0} = \sum_{m\neq 0} \frac{|\langle \phi_m^H|H_{\text{int}}|\phi_0^H\rangle|^2}{E_m^H - E_0^H}, \tag{C.2}$$

where the superscript H indicates quantities associated with the hydrogen atom. Under the long-range approximation, the interaction Hamiltonian may be simplified by revisiting and modifying Eq. (3.6). As the system transitions from the short-range to the long-range regime, the overlap between wavefunctions of the slab and those of the hydrogen atom becomes negligible. i.e., $\langle\phi_i|\phi_H\rangle \to 0$ for all i. This assumption allows the first-order perturbation term becomes:

$$\begin{aligned}\frac{4\pi\varepsilon_0}{q^2}E^{(1)} =& \sum_a \frac{Z_a}{|\mathbf{R}_a - \mathbf{R}_H|} - \langle\phi_H|\sum_a \frac{Z_a}{|\mathbf{R}_a - \mathbf{r}_e|}|\phi_H\rangle - \sum_i^N \langle\phi_i|\frac{1}{|\mathbf{R}_H - \mathbf{r}_i|}\phi_i\rangle \\ &+ \sum_i^N \iint d^3\mathbf{r}_i\, d^3\mathbf{r}_e \frac{n_H(\mathbf{r}_e)n_i(\mathbf{r}_i)}{|\mathbf{r}_i - \mathbf{r}_e|}\end{aligned}.$$

Since the exchange interaction between electrons belonging to the slab and those from the hydrogen atom is absent in the long-range regime, the individual electron

charge densities $n_i(\mathbf{r}_i)$ of the slab could be consolidated into a total charge density $n(\mathbf{r})$. Using the identity $\langle\phi_H|\phi_H\rangle = 1$ and defining the total charge distribution as $\rho(\mathbf{r}) = q\sum_a Z_a\delta^3(\mathbf{R}_a - \mathbf{r}) - qn(\mathbf{r})$. The first-order perturbation term simplifies to

$$E^{(1)} = \frac{q}{4\pi\varepsilon_0}\langle\phi_H| \int d^3\mathbf{r}\ \rho(\mathbf{r}) \left(\frac{1}{|\mathbf{R}_H - \mathbf{r}|} - \frac{1}{|\mathbf{r}_e - \mathbf{r}|}\right) |\phi_H\rangle. \tag{C.3}$$

The numerator of the second-order perturbation term is derived by substituting $\langle\phi_H|with\langle\phi_m^H|$. Accordingly, the interaction Hamiltonian H_{int} corresponding to the second-order perturbation is given by

$$H_{\text{int}}^{(2)} = \frac{q}{4\pi\varepsilon_0} \int d^3\mathbf{r}\ \rho(\mathbf{r}) \left(\frac{1}{|\mathbf{R}_H - \mathbf{r}|} + \frac{1}{|\mathbf{r}_e - \mathbf{r}|}\right). \tag{C.4}$$

Define $\mathbf{r}_{eH} = \mathbf{r}_e - \mathbf{R}_H$, where $\mathbf{r}_{eH}$ denotes the vector pointing from the hydrogen atom to the electron. The bracketed terms can then be expressed as

$$\begin{aligned}\frac{1}{|\mathbf{R}_H - \mathbf{r}|} - \frac{1}{|\mathbf{r}_e - \mathbf{r}|} &= \frac{1}{|\mathbf{R}_H - \mathbf{r}|} - \sum_{l=0}^{\infty} \frac{(r_{eH})^l}{|\mathbf{R}_H - \mathbf{r}|^{l+1}} P_l\left[\frac{-\mathbf{r}_{eH}\cdot(\mathbf{R}_H - \mathbf{r})}{r_{eH}|\mathbf{R}_H - \mathbf{r}|}\right] \\ &= \frac{\mathbf{r}_{eH}\cdot(\mathbf{R}_H - \mathbf{r})}{|\mathbf{R}_H - \mathbf{r}|^3} + \cdots,\end{aligned}$$

where $P_l(*)$ denotes the Legendre polynomial, with the first term representing the leading-order contribution. Consequently, the second-order perturbation term is given by:

$$\begin{aligned}&\sum_{m\neq 0} \frac{|\langle\Psi_m^{(0)}|H_{\text{int}}|\Psi_0^{(0)}\rangle|^2}{E_m - E_0} \\ &\quad\approx \left(\frac{q}{4\pi\varepsilon_0}\right)^2 \sum_{m\neq 0} \frac{1}{E_m^H - E_0^H} \left| \int d^3\mathbf{r}\ \rho(\mathbf{r}) \frac{\langle\phi_m^H|\mathbf{r}_{eH}|\phi_0^H\rangle\cdot(\mathbf{R}_H - \mathbf{r})}{|\mathbf{R}_H - \mathbf{r}|^3}\right|^2 \\ &\quad= q^2 \sum_{m\neq 0} \frac{|\langle\phi_m^H|r_{eH}^2\cos\theta|\phi_0^H\rangle|^2}{E_m^H - E_0^H} \left|\frac{1}{4\pi\varepsilon_0}\nabla_{\mathbf{R}_H} \int \frac{\rho(\mathbf{r})}{|\mathbf{R}_H - \mathbf{r}|}\right|^2,\end{aligned} \tag{C.5}$$

where θ denotes the angle between the vector $\mathbf{r}_{eH}$ and the electric field produced by charge deviations within the slab.

Supplementary

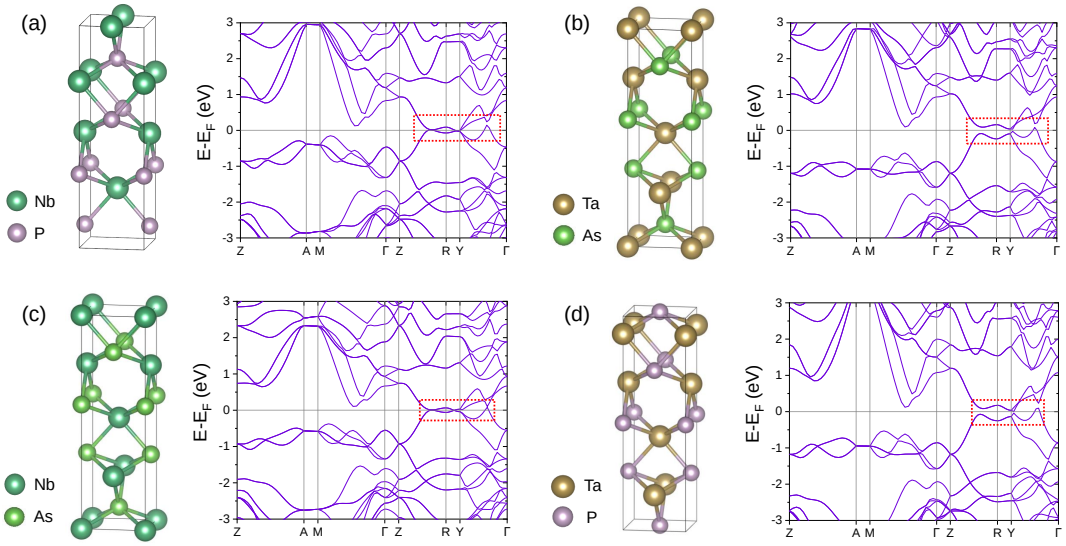

Figure S1: Bulk crystal structures and the corresponding electronic bulk band structures of (a) NbP, (b) TaAs, (c) NbAs and (d) TaP without inclusion of SOC. The DFT calculation were performed at GGA/PBE level. The dashed red boxes highlight the locations of Weyl points.

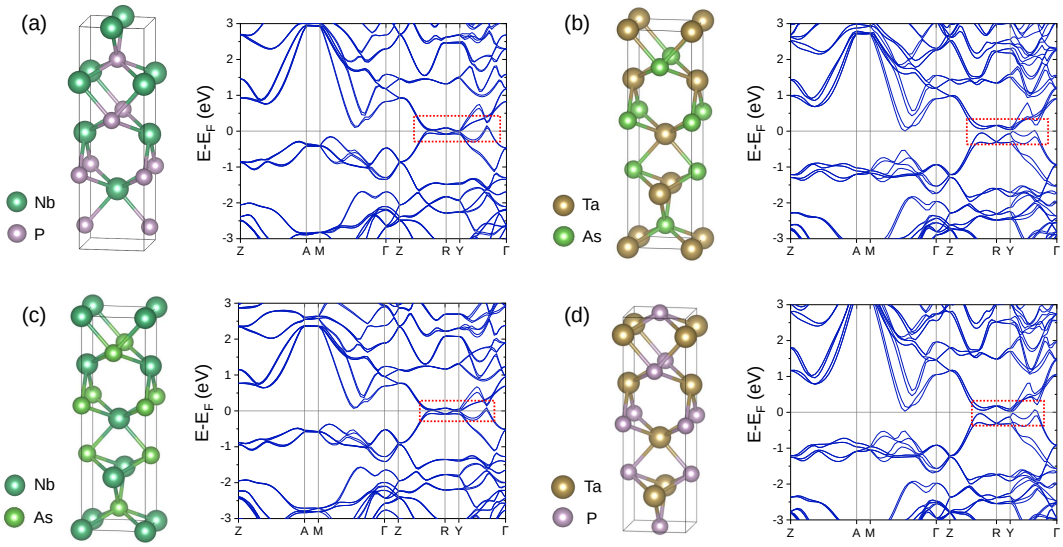

Figure S2: Bulk crystal structures and the corresponding electronic bulk band structures of (a) NbP, (b) TaAs, (c) NbAs and (d) TaP with inclusion of SOC. The DFT calculation were performed at GGA/PBE level. The dashed red boxes highlight the locations of Weyl points.

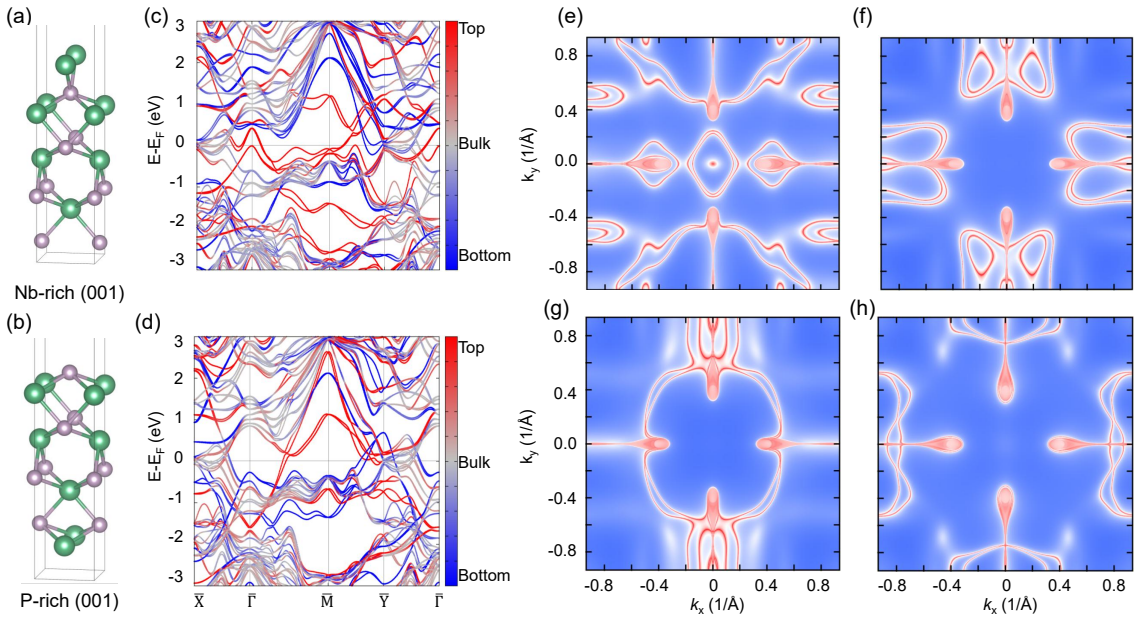

Figure S3: Schematics of NbP (001) slab structures and corresponding Fermi arcs patterns with inclusion of SOC. (a) Nb-rich (001) and (b) P-rich (001). (c) Surface band structure of a slab with Nb-rich top and P-rich bottom surfaces. (d) Surface band structure of a slab with P-rich top and Nb-rich bottom surfaces. Panels (c) and (d) are calculated using a $1 \times 1 \times 6$ supercell via approach of tight-binding model. Fermi energy surfaces corresponding to: (e) Nb-rich top, (f) P-rich bottom, (g) P-rich top and (h) Nb-rich bottom surfaces of the NbP (001) slab.

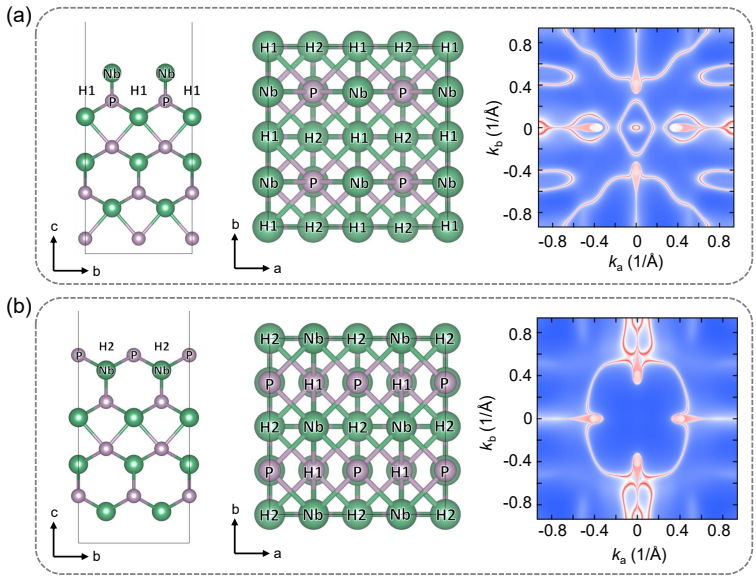

Figure S4: Top- and side-view of the slab structures, together with first surface Brillouin zone of the examined equi-energy surface at E_F for (a) Nb-rich NbP (001)-top and (b) P-rich NbP (001)-top. The identified hydrogen absorption sites are indicated.

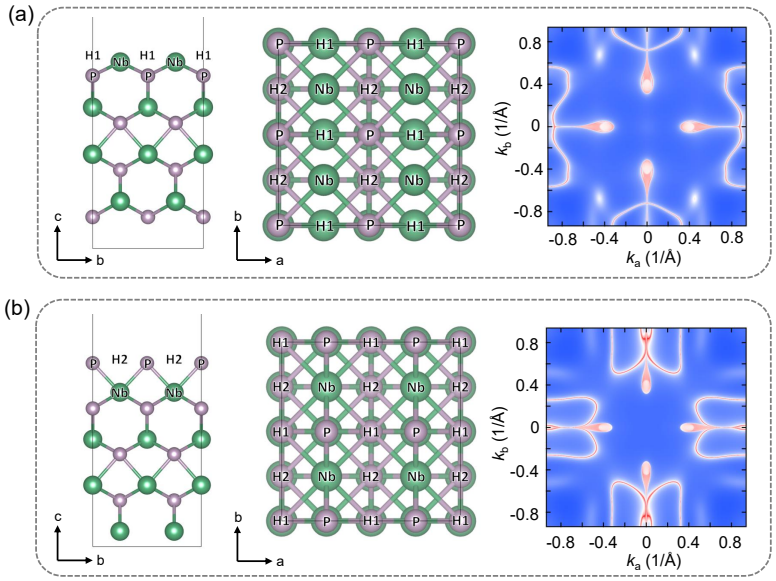

Figure S5: Top- and side-view of the slab structures, together with first surface Brillouin zone of the examined equi-energy surface at E_F for (a) Nb-rich NbP (001)-bottom and (b) P-rich NbP (001)-bottom. The identified hydrogen absorption sites are indicated.

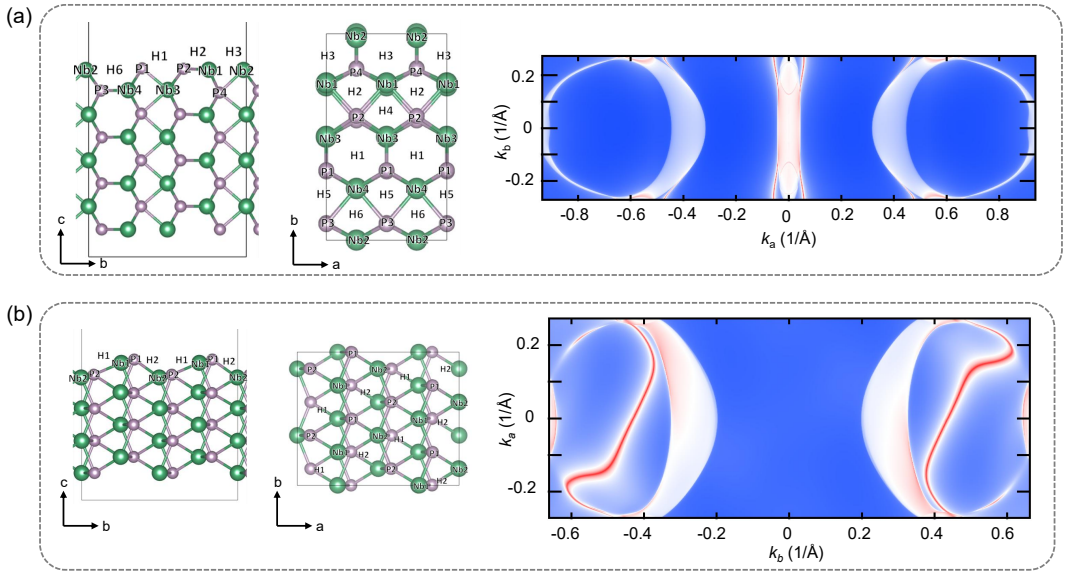

Figure S6: Top- and side-view of the slab structures, together with first surface Brillouin zone of the examined equi-energy surface at E_F for (a) NbP (100) and (b) NbP (110). The identified hydrogen absorption sites are indicated.

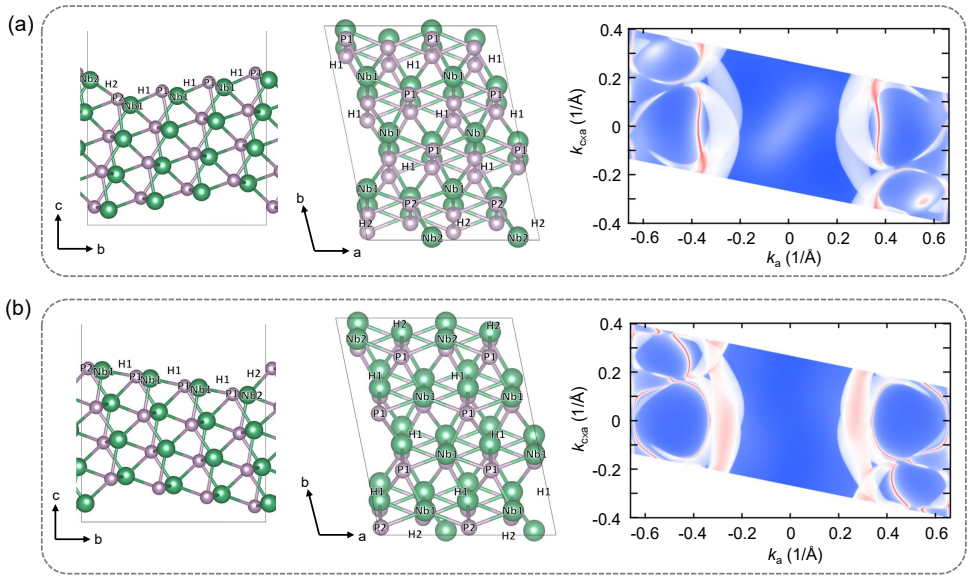

Figure S7: Top- and side-view of the slab structures, together with first surface Brillouin zone of the examined equi-energy surface at E_F for (a) NbP (111)-top and (b) NbP (111)-bottom. The identified hydrogen absorption sites are indicated.

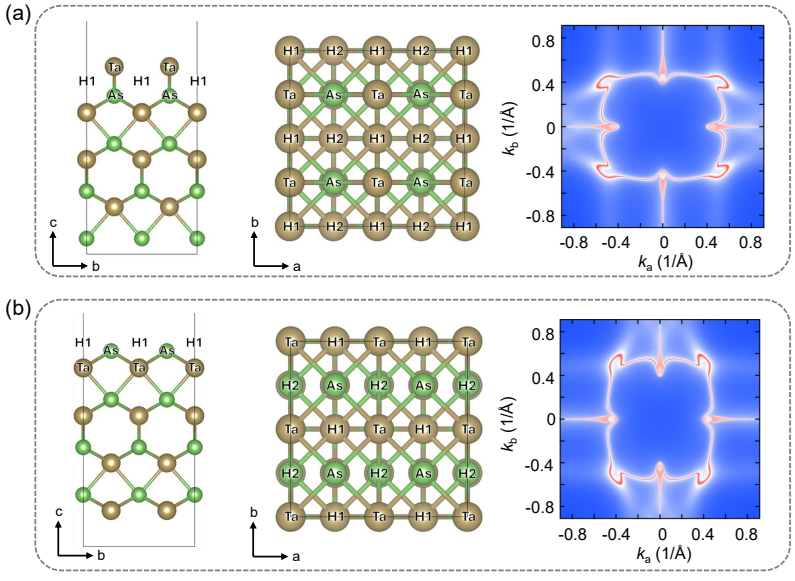

Figure S8: Top- and side-view of the slab structures, together with first surface Brillouin zone of the examined equi-energy surface at E_F for (a) Ta-rich TaAs (001)-top and (b) As-rich TaAs (001)-top. The identified hydrogen absorption sites are indicated.

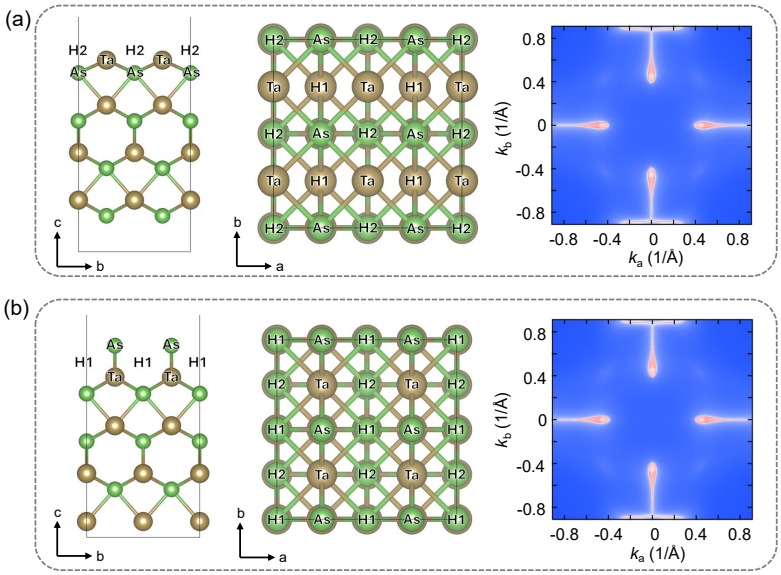

Figure S9: Top- and side-view of the slab structures, together with first surface Brillouin zone of the examined equi-energy surface at E_F for (a) Ta-rich TaAs (001)-bottom and (b) As-rich TaAs (001)-bottom. The identified hydrogen absorption sites are indicated.

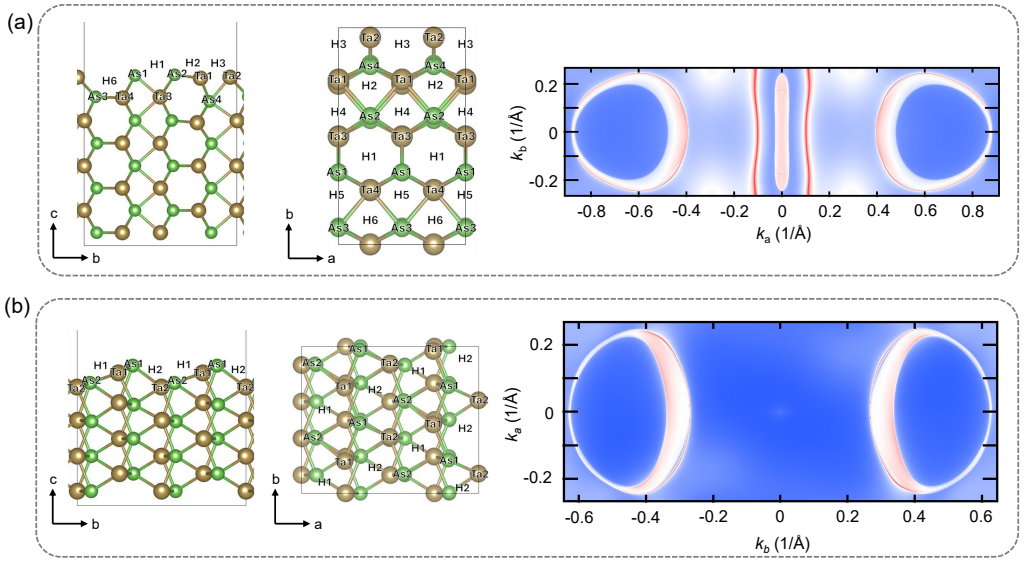

Figure S10: Top- and side-view of the slab structures, together with first surface Brillouin zone of the examined equi-energy surface at E_F for (a) TaAs (100) and (b) TaAs (110). The identified hydrogen absorption sites are indicated.

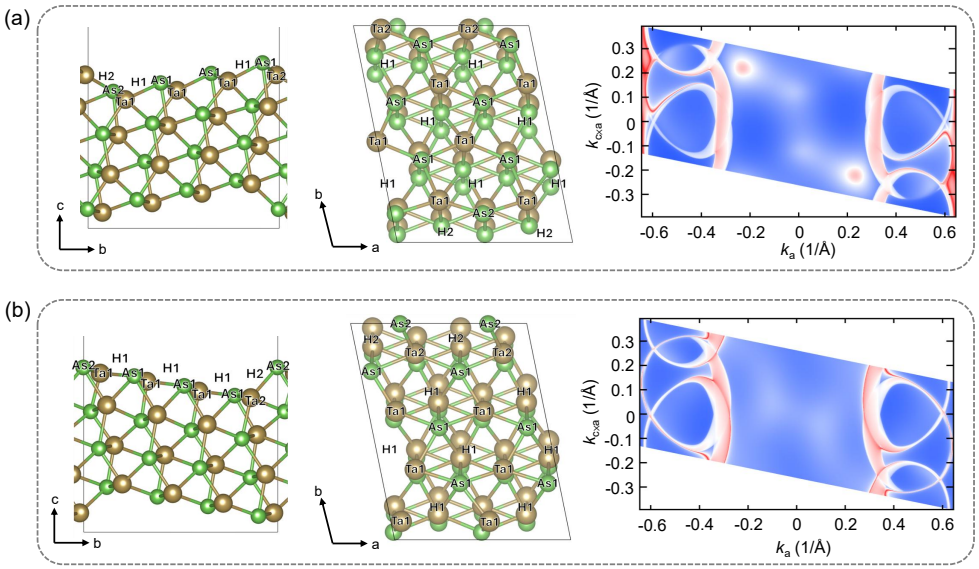

Figure S11: Top- and side-view of the slab structures, together with first surface Brillouin zone of the examined equi-energy surface at E_F for (a) TaAs (111)-top and (b) TaAs (111)-bottom. The identified hydrogen absorption sites are indicated.

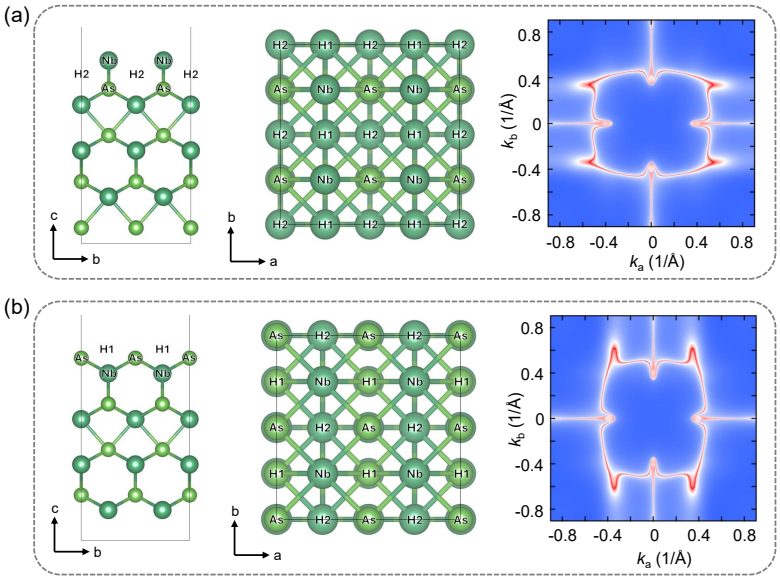

Figure S12: Top- and side-view of the slab structures, together with first surface Brillouin zone of the examined equi-energy surface at E_F for (a) Nb-rich NbAs (001)-top and (b) As-rich NbAs (001)-top. The identified hydrogen absorption sites are indicated.

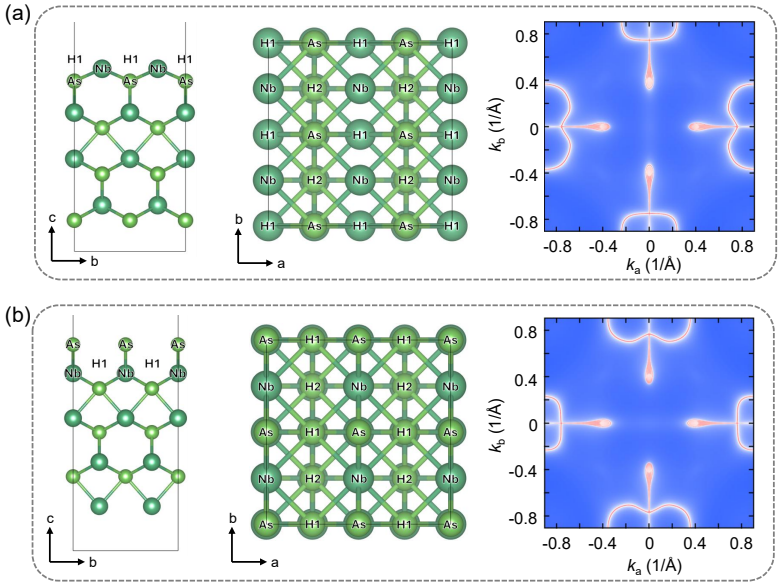

Figure S13: Top- and side-view of the slab structures, together with first surface Brillouin zone of the examined equi-energy surface at E_F for (a) Nb-rich NbAs (001)-bottom and (b) As-rich NbAs (001)-bottom. The identified hydrogen absorption sites are indicated.

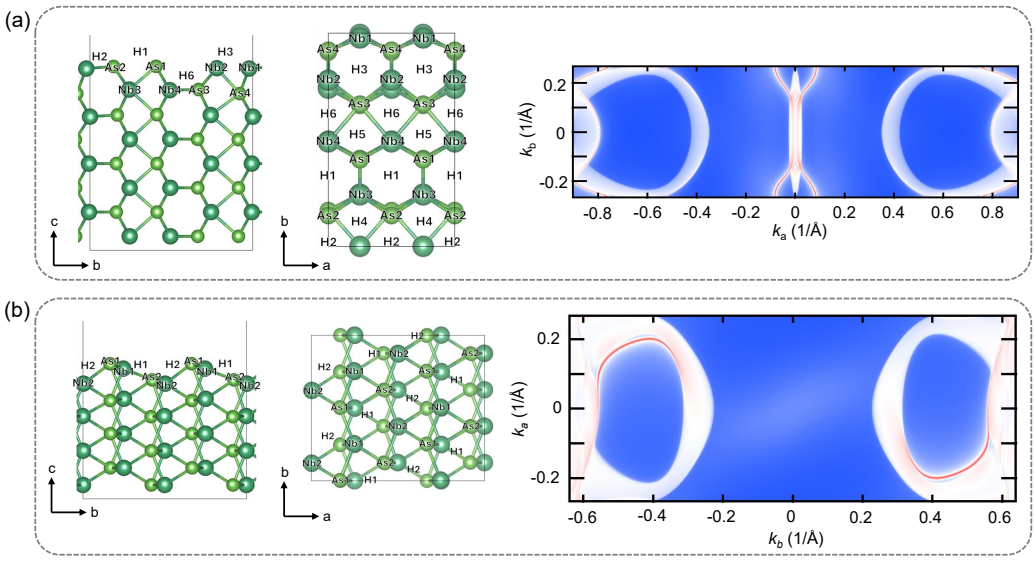

Figure S14: Top- and side-view of the slab structures, together with first surface Brillouin zone of the examined equi-energy surface at E_F for (a) NbAs(100) and (b) NbAs (110). The identified hydrogen absorption sites are indicated.

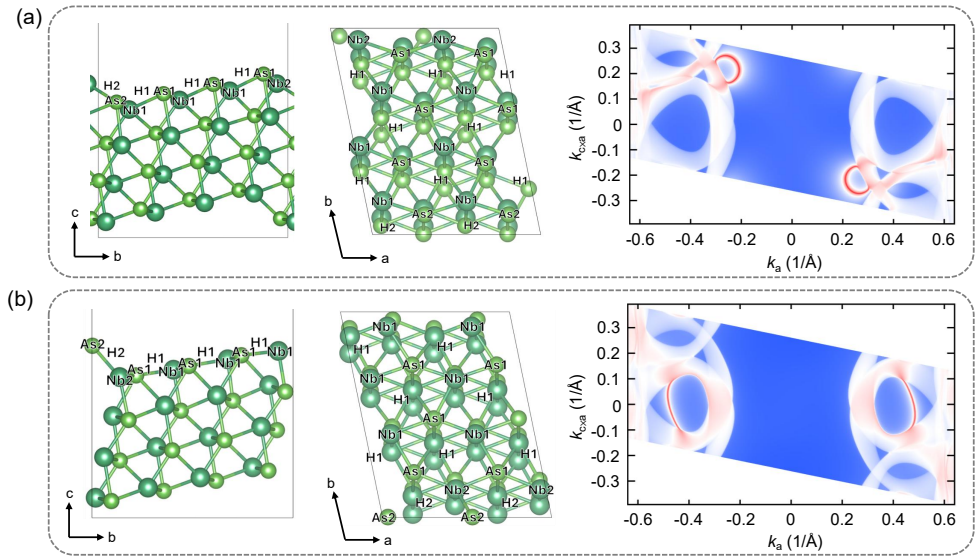

Figure S15: Top- and side-view of the slab structures, together with first surface Brillouin zone of the examined equi-energy surface at E_F for (a) NbAs (111)-top and (b) NbAs (111)-bottom. The identified hydrogen absorption sites are indicated.

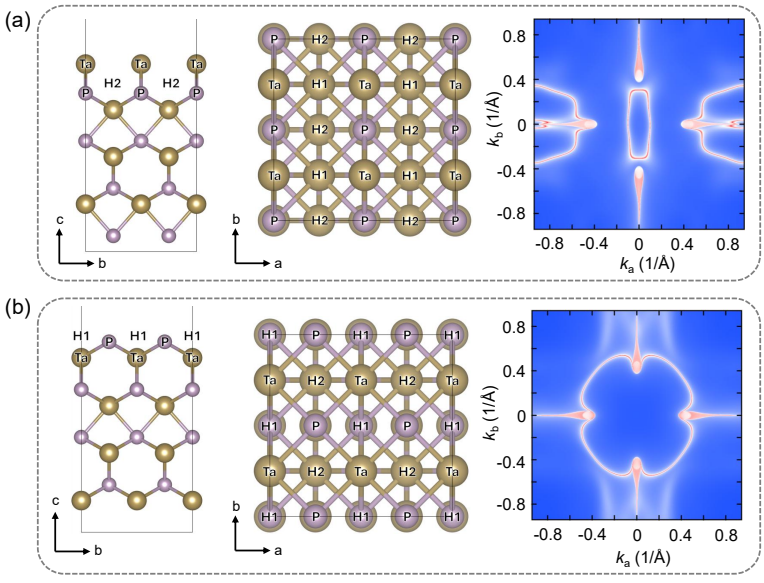

Figure S16: Top- and side-view of the slab structures, together with first surface Brillouin zone of the examined equi-energy surface at E_F for (a) Ta-rich TaP (001)-top and (b) P-rich TaP (001)-top. The identified hydrogen absorption sites are indicated.

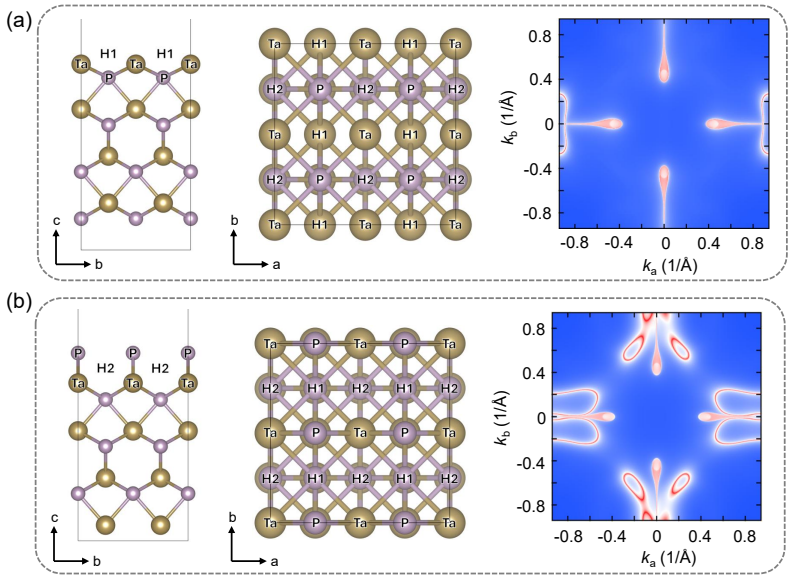

Figure S17: Top- and side-view of the slab structures, together with first surface Brillouin zone of the examined equi-energy surface at E_F for (a) Ta-rich TaP (001)-bottom and (b) P-rich TaP (001)-bottom. The identified hydrogen absorption sites are indicated.

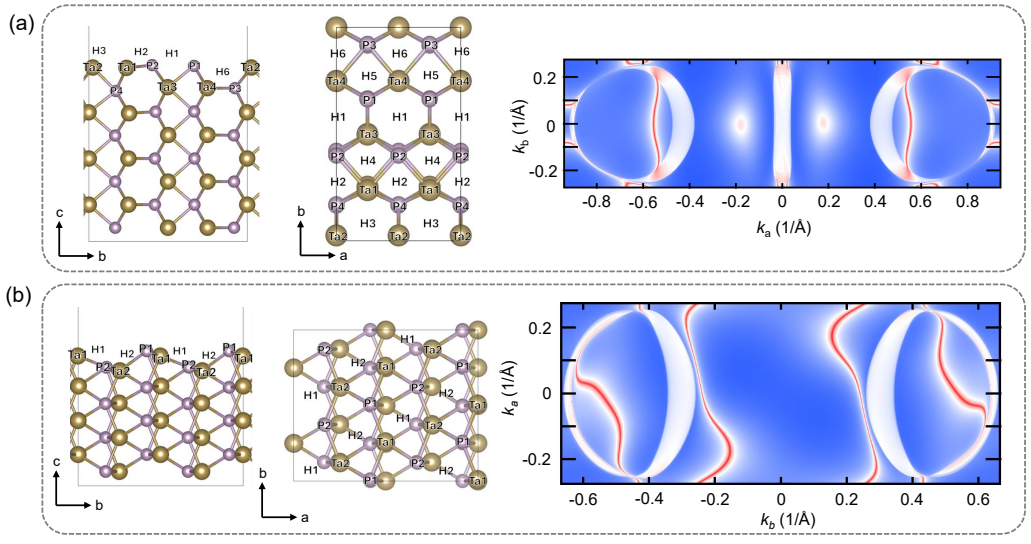

Figure S18: Top- and side-view of the slab structures, together with first surface Brillouin zone of the examined equi-energy surface at E_F for (a) TaP (100) and (b) TaP (110). The identified hydrogen absorption sites are indicated.

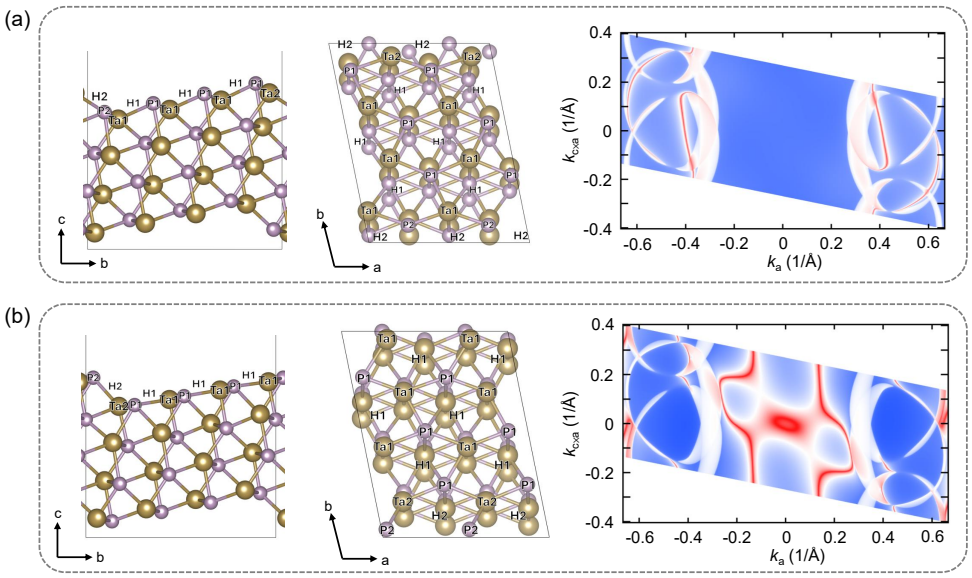

Figure S19: Top- and side-view of the slab structures, together with first surface Brillouin zone of the examined equi-energy surface at E_F for (a) TaP (111)-top and (b) TaP (111)-bottom. The identified hydrogen absorption sites are indicated.

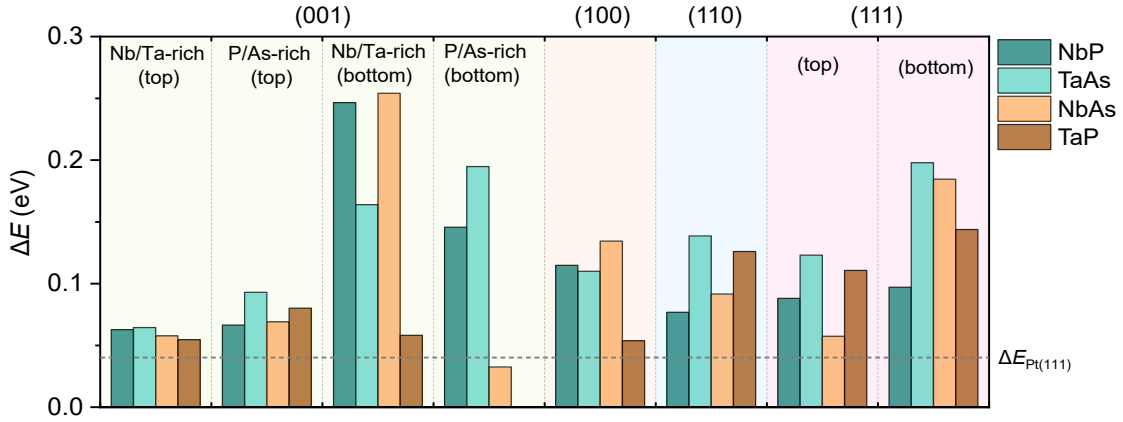

Figure S20: Energy variation induced by surface atom rearrangement upon hydrogen adsorption. The P-rich TaP (001) bottom facet exhibits a negative energy change, attributed to the formation of P–P bonds following hydrogen adsorption.

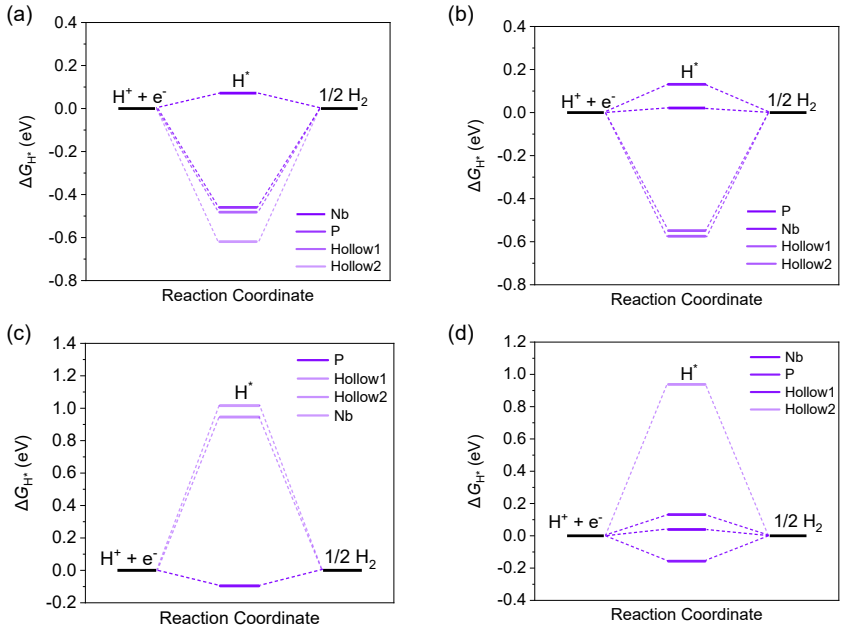

Figure S21: Gibbs free energy changes for H∗ adsorption $\Delta G_{\mathrm{H}*}$ on NbP: (a) Nb-rich (001)-top, (b) P-rich (001)-top, (c) Nb-rich (001)-bottom, and (d) P-rich (001)-bottom, at different hydrogen absorption sites.

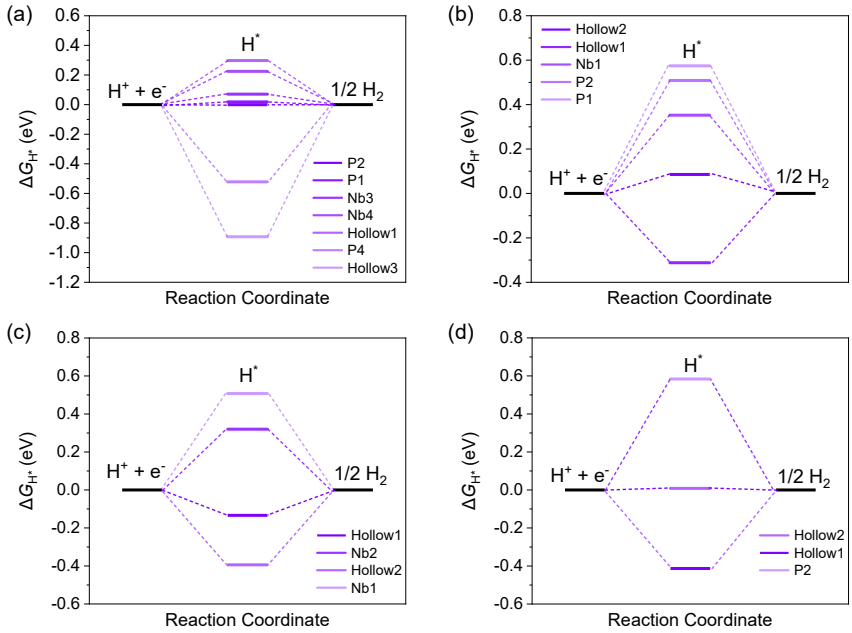

Figure S22: Gibbs free energy changes for H∗ adsorption $\Delta G_{\mathrm{H}*}$ on NbP: (a) (100), (b) (110), (c) (111)-top, and (d) (111)-bottom, at different hydrogen absorption sites.

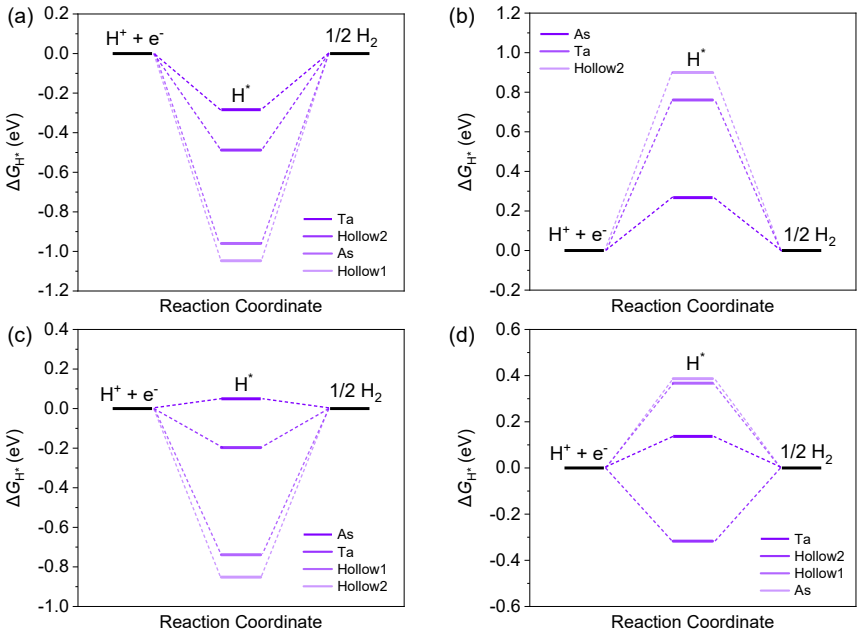

Figure S23: Gibbs free energy changes for H∗ adsorption $\Delta G_{\mathrm{H}*}$ on TaAs: (a) Ta-rich (001)-top, (b) As-rich (001)-top, (c) Ta-rich (001)-bottom, and (d) As-rich (001)-bottom, at different hydrogen absorption sites.

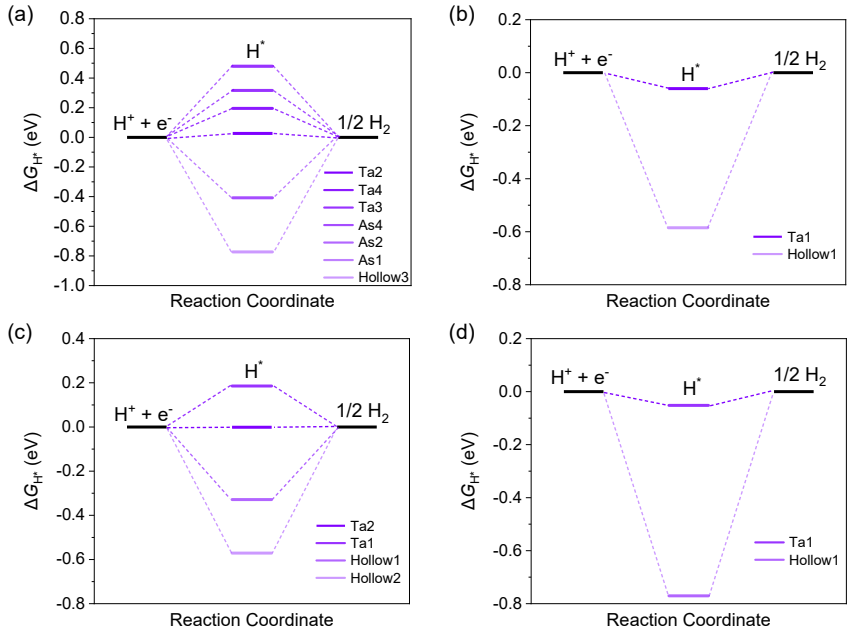

Figure S24: Gibbs free energy changes for H∗ adsorption $\Delta G_{\mathrm{H}*}$ on TaAs: (a) (100), (b) (110), (c) (111)-top, and (d) (111)-bottom, at different hydrogen absorption sites.

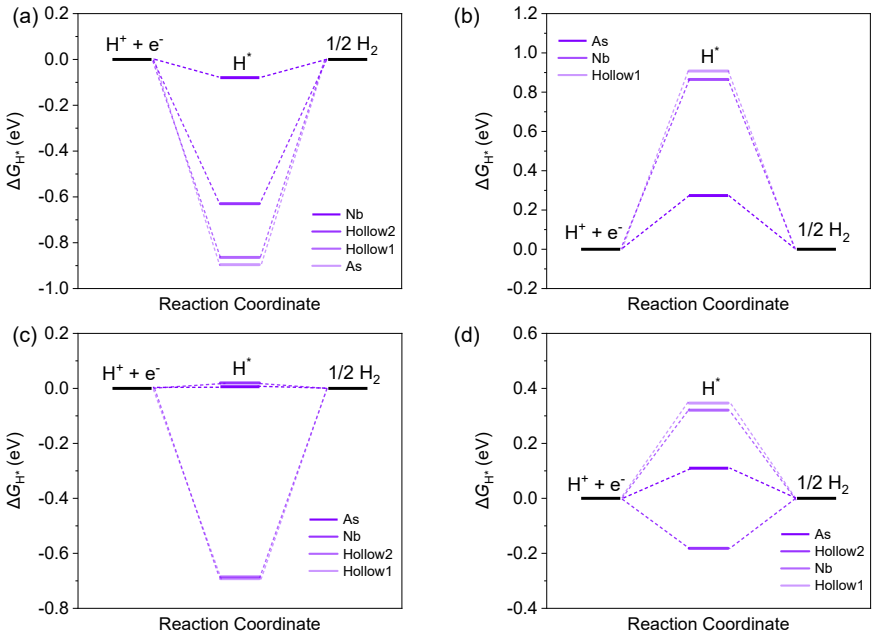

Figure S25: Gibbs free energy changes for H∗ adsorption $\Delta G_{\mathrm{H}*}$ on NbAs: (a) Nb-rich (001)-top, (b) As-rich (001)-top, (c) Nb-rich (001)-bottom, and (d) As-rich (001)-bottom, at different hydrogen absorption sites.

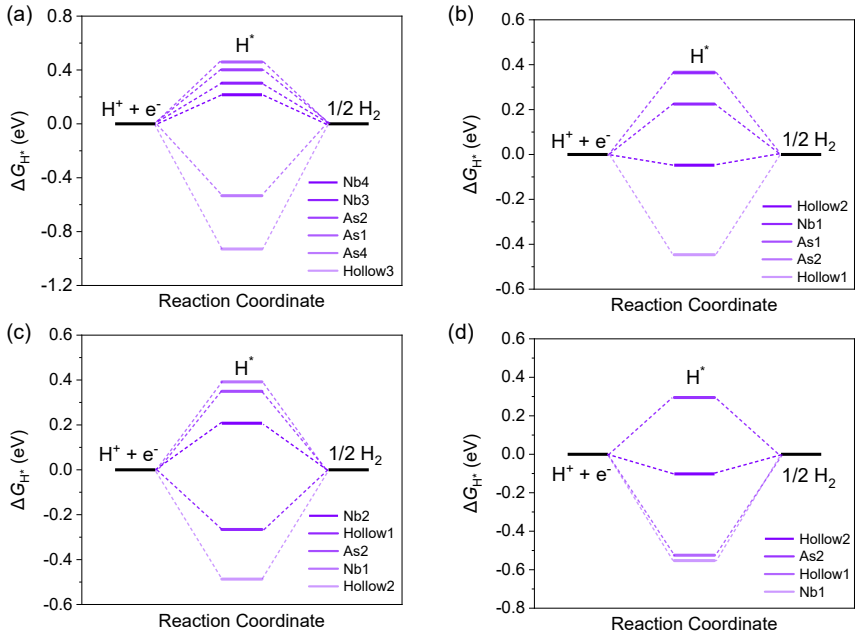

Figure S26: Gibbs free energy changes for H∗ adsorption $\Delta G_{\mathrm{H}*}$ on NbAs: (a) (100), (b) (110), (c) (111)-top, and (d) (111)-bottom, at different hydrogen absorption sites.

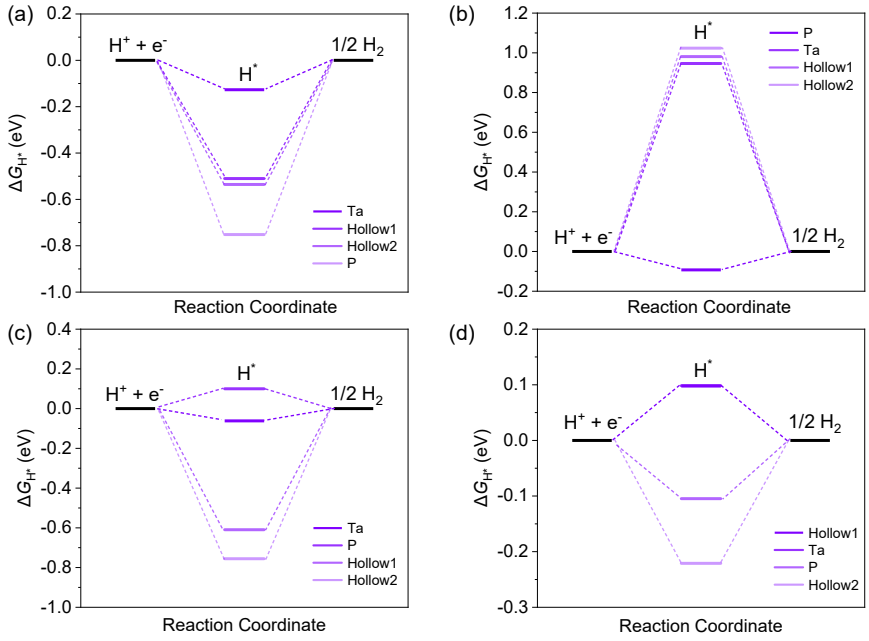

Figure S27: Gibbs free energy changes for H∗ adsorption $\Delta G_{\mathrm{H}*}$ on TaP: (a) Ta-rich (001)-top, (b) P-rich (001)-top, (c) Ta-rich (001)-bottom, and (d) P-rich (001)-bottom, at different hydrogen absorption sites.

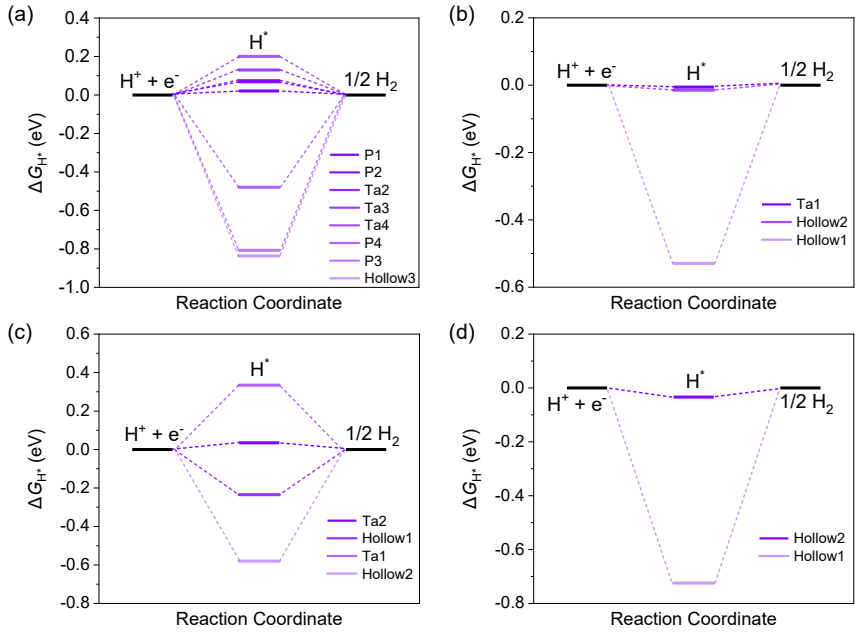

Figure S28: Gibbs free energy changes for H∗ adsorption $\Delta G_{\mathrm{H}*}$ on TaP: (a) (100), (b) (110), (c) (111)-top, and (d) (111)-bottom, at different hydrogen absorption sites.

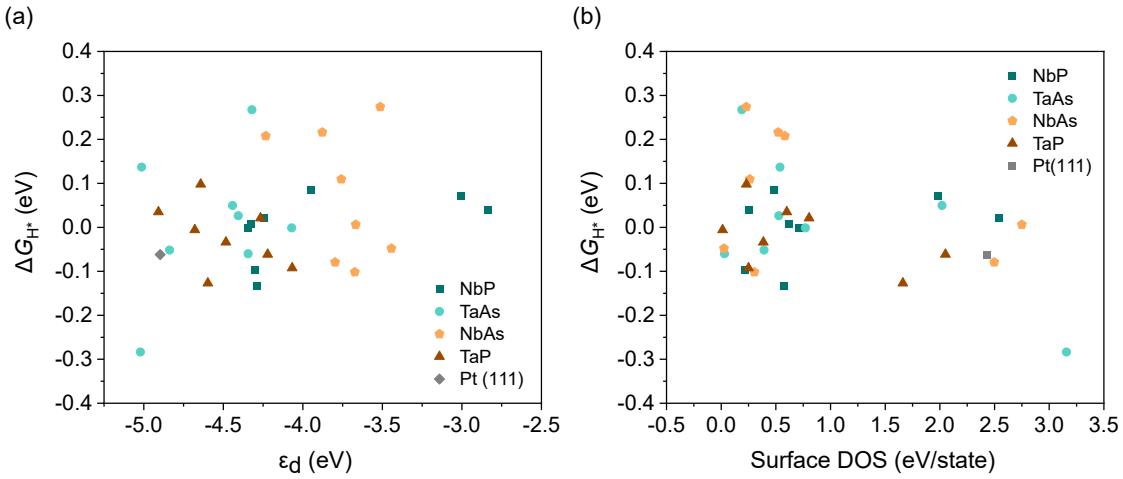

Figure S29: The relationship between Gibbs free energy change for hydrogen adsorption $\Delta G_{\mathrm{H}*}$ and (a) *d*-band centre, as well as (b) surface density of state at the Fermi level.

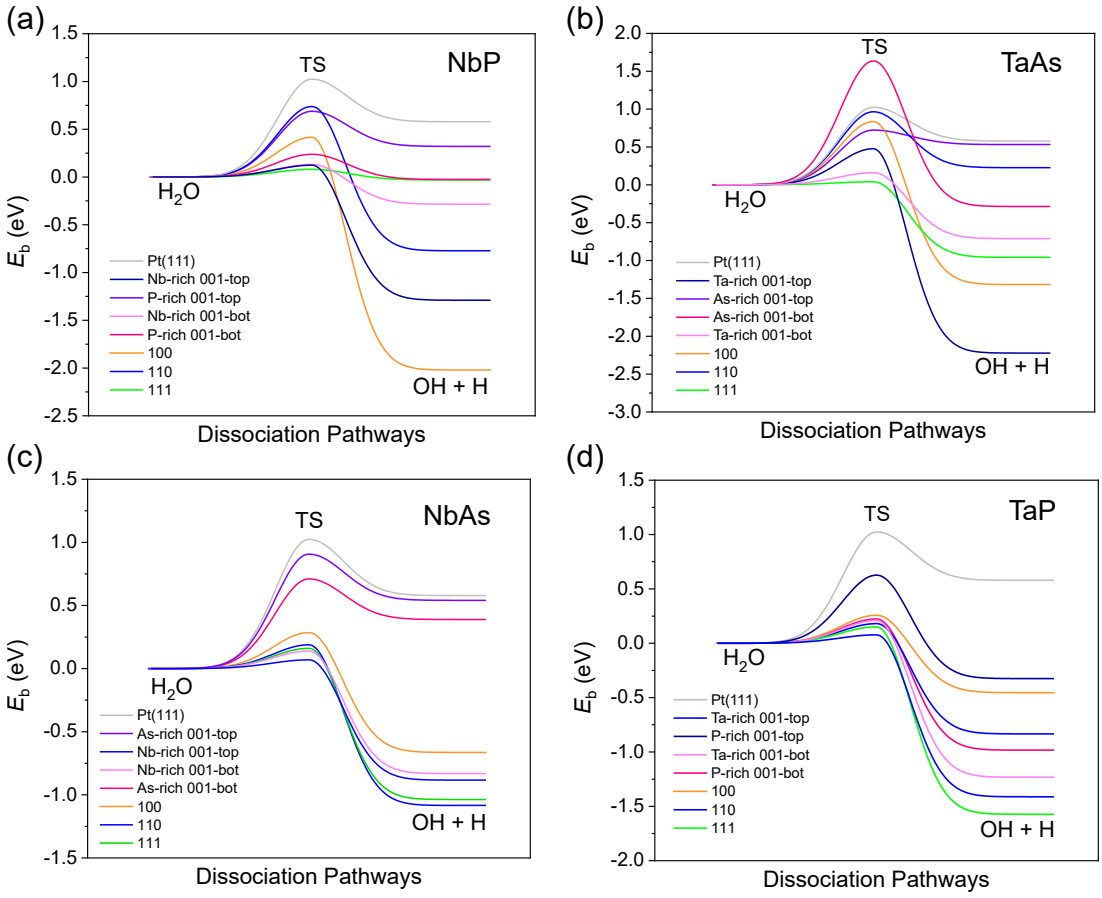

Figure S30: Energy barriers of water dissociation of (a) NbP, (b) TaAs, (c) NbAs and (d) TaP. The locations of hydrogen absorption position are considered at the most active absorption sites, and the hydroxides are located at the neighbouring absorption sites.

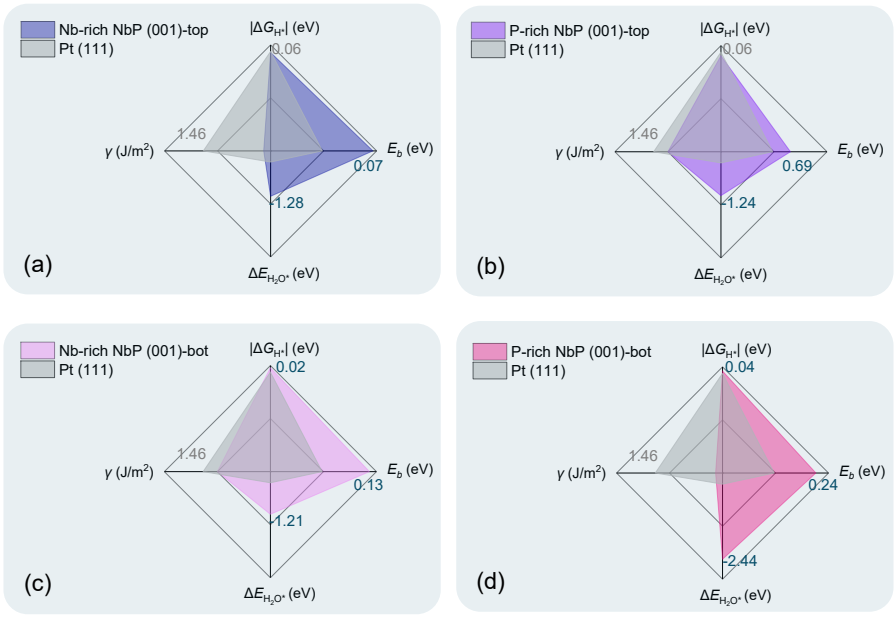

Figure S31: Rader charts of NbP with different facets: (a) Nb-rich NbP (001)-top, (b) P-rich NbP (001)-top, (c) Nb-rich NbP (001)-bottom and (d) P-rich NbP (001)-bottom, illustrating their predicted catalytic performance in HER.

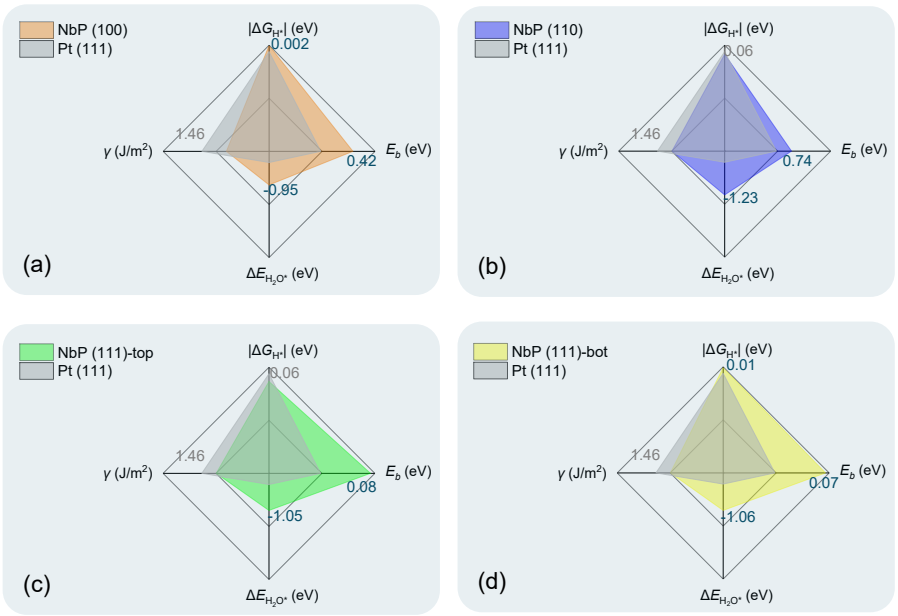

Figure S32: Rader charts of NbP with different facets: (a) NbP (100), (b) NbP (110), (c) NbP (111)-top and (d) NbP (111)-bottom, illustrating their predicted catalytic performance in HER.

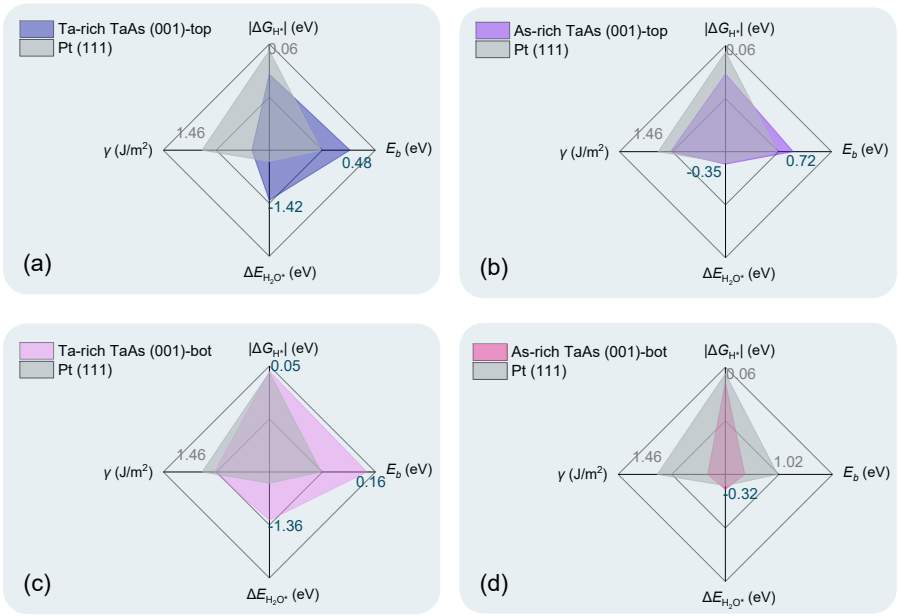

Figure S33: Rader charts of NbP with different facets: (a) Ta-rich TaAs (001)-top, (b) As-rich TaAs (001)-top, (c) Ta-rich TaAs (001)-bottom, and (d) As-rich TaAs (001)-bottom, illustrating their predicted catalytic performance in HER.

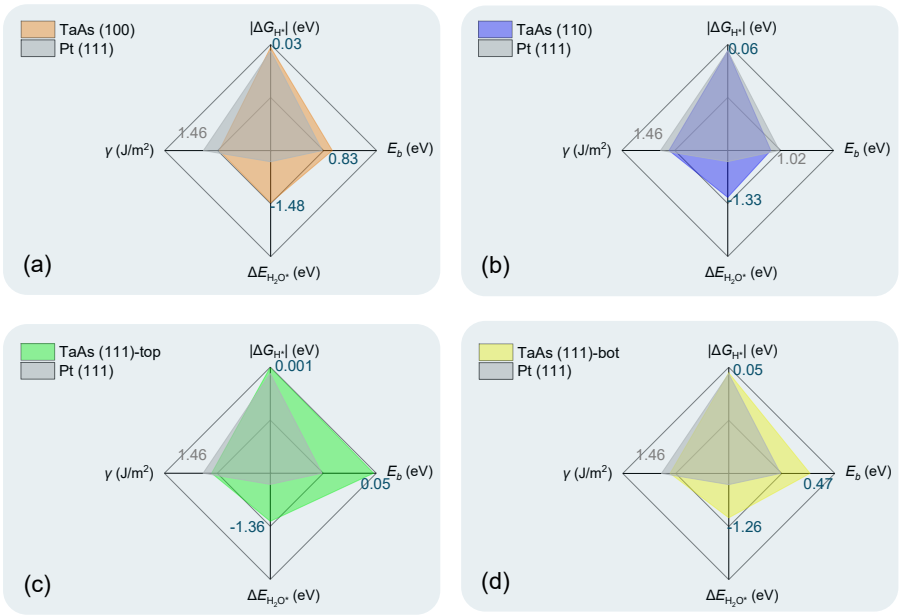

Figure S34: Rader charts of NbP with different facets: (a) TaAs (100), (b) TaAs (110), (c) TaAs (111)-top and (d) TaAs (111)-bottom, illustrating their predicted catalytic performance in HER.

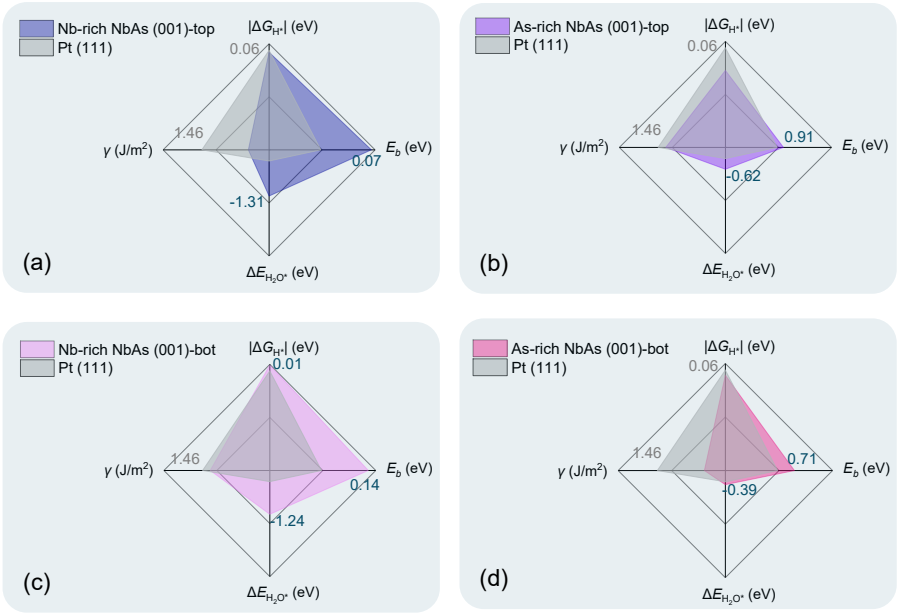

Figure S35: Rader charts of NbP with different facets: (a) Nb-rich NbAs (001)-top, (b) As-rich NbAs (001)-top, (c) Nb-rich NbAs (001)-bottom and (d) As-rich NbAs (001)-bottom, illustrating their predicted catalytic performance in HER.

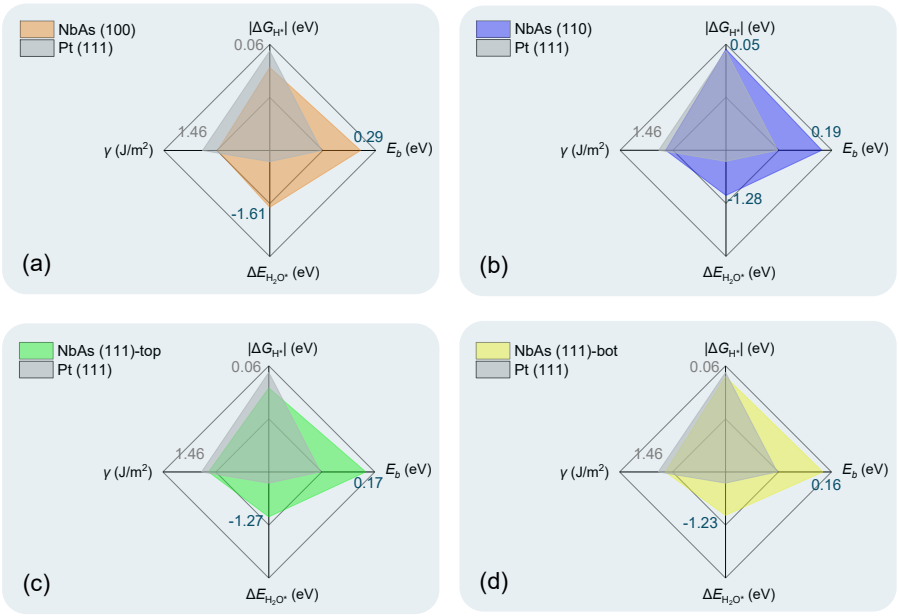

Figure S36: Rader charts of NbP with different facets: (a) NbAs (100), (b) NbAs (110), (c) NbAs (111)-top and (d) NbAs (111)-bottom, illustrating their predicted catalytic performance in HER.

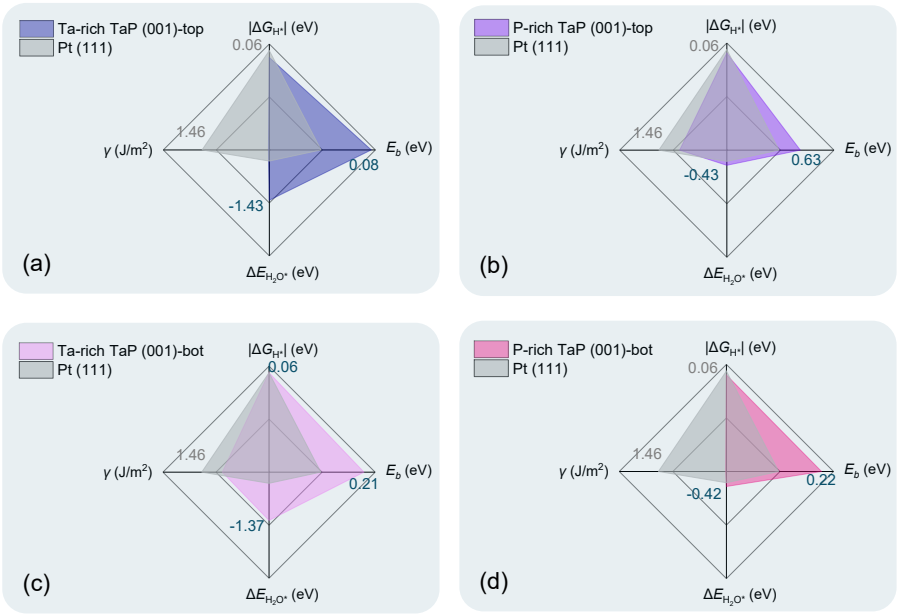

Figure S37: Rader charts of NbP with different facets: (a) Ta-rich TaP (001)-top, (b) P-rich TaP (001)-top, (c) Ta-rich TaP (001)-bottom and (d) P-rich TaP (001)-bottom, illustrating their predicted catalytic performance in HER.

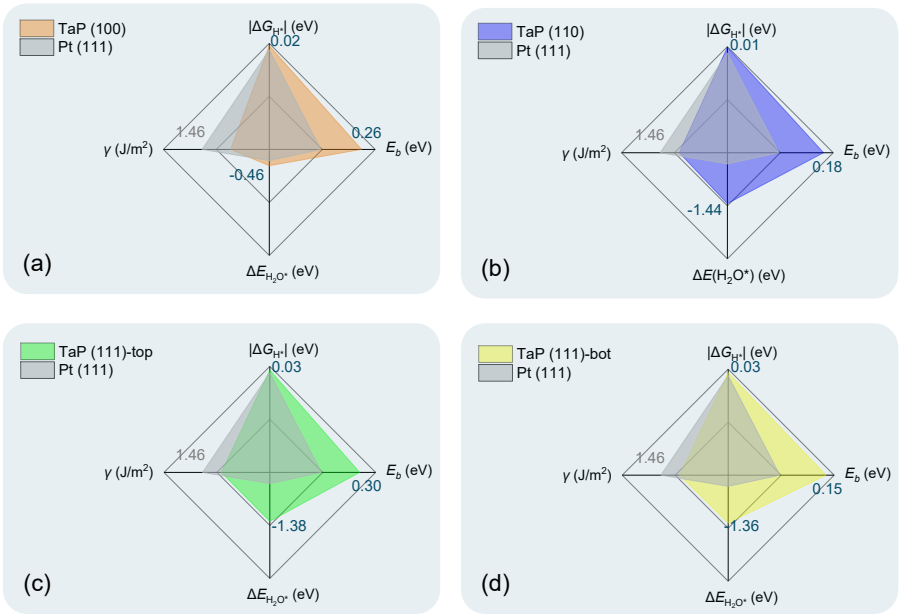

Figure S38: Rader charts of NbP with different facets: (a) TaP (100), (b) TaP (110), (c) TaP (111)-top and (d) TaP (111)-bot, illustrating their predicted catalytic performance in HER.

List of Publications

The publications during the PhD study. The names of the author are underlined, and the corresponding author is marked with an asterisk (*).

[1] T. W. Lau, Q. Lei*, and J. Yin*, Facet engineering of Weyl semimetals for efficient hydrogen evolution reaction, Mater. Today Catal. **8**, 100091 (2025).

[2] Z. Xu, T. W. Lau, P. Xiong, J. Li, M. M.-J. Li*, J. Yin*, and Y. Zhu*, Imaging Anisotropic Proton Intercalation in Photochromic MoO_3. Nano Lett. **24**, 9727 (2024).

[3] S. Xu, T. Naren, Y. Zhao, Q. Gu, T. W. Lau, C.-S. Lee, F.-R. Chen, J. Yin*, L. Chen*, and Q. Zhang*, Soluble Covalent Organic Frameworks as Efficient Lithiophilic Modulator for High-Performance Lithium Metal Batteries, Angew. Chem. **64**, e202422040 (2025).

[4] J. Liu, Y. He, L. Ding, H. Zhang, Q. Li, L. Jia, J. Yu, T. W. Lau, M. Li, Y. Qin, X. Gu, F. Zhang, Q. Li, Y. Yang, S. Zhao, X. Wu, J. Liu, T. Liu, Y. Gao, Y. Wang, X. Dong, H. Chen, P. Li, T. Zhou, M. Yang, X. Ru, F. Peng, S. Yin, M. Qu, D. Zhao, Z. Zhao, M. Li, P. Guo, H. Yan, C. Xiao, P. Xiao*, J. Yin*, X. Zhang*, Z. Li*, B. He*, and X. Xu*, Perovskite/silicon tandem solar cells with

bilayer interface passivation, Nature **635**, 596 (2024).

[5] Y. Yan, P. Li, Y. Wang, L. Bi, T. W. Lau, M. Miao, S. Yang, Q. Xiong, F. R. Lin, H.-L. Yip, J. Yin*, C. Zhi*, and A. K.-Y. Jen*, Molecular Engineering of N-heteroaromatic Organic Cathode for High-Voltage and Highly Stable Zinc Batteries, Adv. Funct. Mater. **35**, 2312332 (2025).

[6] Q. Wei, H. Ren, J. Liu, Q. Liu, C. Wang, T. W. Lau, L. Zhou, T. Bian, Y. Zhou, P. Wang, Q. Lei, O. F. Mohammed*, M. Li*, and J. Yin*, Long-Lived Hot Carriers in Two-Dimensional Perovskites: The Role of Alternating Cations in Interlayer Space, ACS Energy Lett. **8**, 4315 (2023).

References

[1] H. Zhang, P. An, W. Zhou, B. Y. Guan, P. Zhang, J. Dong, and X. W. D. Lou, Dynamic traction of lattice-confined platinum atoms into mesoporous carbon matrix for hydrogen evolution reaction, Sci. Adv. **4**, eaao6657 (2018).

[2] C. Zhang, Z. Xu, N. Han, Y. Tian, T. Kallio, C. Yu, and L. Jiang, Superaerophilic/superaerophobic cooperative electrode for efficient hydrogen evolution reaction via enhanced mass transfer, Sci. Adv. **9**, eadd6978 (2023).

[3] M. Li, Q. Ma, W. Zi, X. Liu, X. Zhu, and S. F. Liu, Pt monolayer coating on complex network substrate with high catalytic activity for the hydrogen evolution reaction, Sci. Adv. **1**, e1400268 (2015).

[4] G. Zhao, K. Rui, S. X. Dou, and W. Sun, Heterostructures for Electrochemical Hydrogen Evolution Reaction: A Review, Adv. Funct. Mater. **28**, 1803291 (2018).

[5] Z. Xu, S. Zhang, H. Chen, J. Yan, Y. Zhang, Q. Liang, and W. Huang, Interfacial engineering of CuCoLDH@GDY/NF heterostructure for bifunctional electrocatalysis in alkaline water splitting: Mechanistic insights and scalable synthesis, Int. J. Hydrogen Energy **155**, 150187 (2025).

[6] S. Skakri, A. El Attar, S. Benhaiba, B. Bouljoihel, A. Aaddane, A. Mouakkar, A. Rais, and M. El Rhazi, Facile synthesis of a Ni–Cu composite reinforced with a para-phenylenediamine layer for enhanced hydrogen evolution reaction, RSC Adv. **15**, 24256 (2025).

[7] D. Strmcnik, P. P. Lopes, B. Genorio, V. R. Stamenkovic, and N. M. Markovic, Design principles for hydrogen evolution reaction catalyst materials, Nano Energy **29**, 29 (2016).

[8] F. Sun, Q. Tang, and D.-e. Jiang, Theoretical Advances in Understanding and Designing the Active Sites for Hydrogen Evolution Reaction, ACS Catal. **12**, 8404 (2022).

[9] X. Xu, Y. Chen, W. Zhou, Z. Zhu, C. Su, M. Liu, and Z. Shao, A Perovskite Electrocatalyst for Efficient Hydrogen Evolution Reaction, Adv. Mater. **28**, 6442 (2016).

[10] J. Mahmood, F. Li, S.-M. Jung, M. S. Okyay, I. Ahmad, S.-J. Kim, N. Park, H. Y. Jeong, and J.-B. Baek, An efficient and pH-universal ruthenium-based catalyst for the hydrogen evolution reaction, Nat. Nanotechnol. **12**, 441 (2017).

[11] W. Zhang, F. Li, Y. Li, A. Song, K. Yang, D. Wu, W. Shang, Z. Yao, W. Gao, T. Deng, *et al.*, The role of surface substitution in the atomic disorder-to-order phase transition in multi-component core–shell structures, Nat. Commun. **15**, 9762 (2024).

[12] B. Hammer and J. Nørskov, Electronic factors determining the reactivity of metal surfaces, Surf. Sci. **343**, 211 (1995).

[13] B. Cai, D. Shen, Y. Xie, H. Yan, Y. Wang, X. Chen, L. Wang, and H. Fu, Unlocking superior hydrogen oxidation and CO poisoning resistance on Pt enabled by tungsten nitride-mediated electronic modulation, J. Am. Chem. Soc. **146**, 33193 (2024).

[14] C. Wan, Z. Zhang, J. Dong, M. Xu, H. Pu, D. Baumann, Z. Lin, S. Wang, J. Huang, A. H. Shah, *et al.*, Amorphous nickel hydroxide shell tailors local chemical environment on platinum surface for alkaline hydrogen evolution reaction, Nat. Mater. **22**, 1022 (2023).

[15] Y. Zhu, M. Klingenhof, C. Gao, T. Koketsu, G. Weiser, Y. Pi, S. Liu, L. Sui, J. Hou, J. Li, *et al.*, Facilitating alkaline hydrogen evolution reaction on the hetero-interfaced Ru/RuO_2 through pt single atoms doping, Nat. Commun. **15**, 1447 (2024).

[16] Y. Li, X. Wan, Z. Chen, D. Ding, H. Li, N. Zhang, D. Liu, and Y. Cui, Activity enhancement of molybdenum carbide in alkaline hydrogen evolution reaction through oxidation-gradient modulation, ACS Catal. **14**, 16712 (2024).

[17] X.-L. Zhang, P.-C. Yu, X.-Z. Su, S.-J. Hu, L. Shi, Y.-H. Wang, P.-P. Yang, F.-Y. Gao, Z.-Z. Wu, L.-P. Chi, *et al.*, Efficient acidic hydrogen evolution in proton exchange membrane electrolyzers over a sulfur-doped marcasite-type electrocatalyst, Sci. Adv. **9**, eadh2885 (2023).

[18] J. D. Benck, T. R. Hellstern, J. Kibsgaard, P. Chakthranont, and T. F. Jaramillo, Catalyzing the hydrogen evolution reaction (HER) with molybdenum sulfide nanomaterials, ACS Catal. **4**, 3957 (2014).

[19] H. Li, C. Tsai, A. L. Koh, L. Cai, A. W. Contryman, A. H. Fragapane, J. Zhao, H. S. Han, H. C. Manoharan, F. Abild-Pedersen, *et al.*, Activating and optimizing MoS_2 basal planes for hydrogen evolution through the formation of strained sulphur vacancies, Nat. Mater. **15**, 48 (2016).

[20] N. Abidi, A. Bonduelle-Skrzypczak, and S. N. Steinmann, How stable are 2H-MoS_2 edges under hydrogen evolution reaction conditions?, J. Phys. Chem. C **125**, 17058 (2021).

[21] S. Guo, X. Zhou, J.-K. Lee, Q. Guo, X. Liu, Y. Wu, M. Ma, Z. Zhang, and Z. Liu, Nanoscale identification of local strain effect on tmd catalysis, J. Am. Chem. Soc. **146**, 31920 (2024).

[22] W. Feng, W. Pang, Y. Xu, A. Guo, X. Gao, X. Qiu, and W. Chen, Transition metal selenides for electrocatalytic hydrogen evolution reaction, ChemElectroChem **7**, 31 (2020).

[23] K. S. Bhat and H. Nagaraja, Nickel selenide nanostructures as an electrocatalyst for hydrogen evolution reaction, Int. J. Hydrog. Energy **43**, 19851 (2018).

[24] L. Zhai, T. W. Benedict Lo, Z.-L. Xu, J. Potter, J. Mo, X. Guo, C. C. Tang, S. C. Edman Tsang, and S. P. Lau, In situ phase transformation on nickel-based selenides for enhanced hydrogen evolution reaction in alkaline medium, ACS Energy Lett. **5**, 2483 (2020).

[25] E. J. Popczun, C. G. Read, C. W. Roske, N. S. Lewis, and R. E. Schaak, Highly active electrocatalysis of the hydrogen evolution reaction by cobalt phosphide nanoparticles, Angew. Chem. **53**, 5427 (2014).

[26] A. R. Kucernak and V. N. N. Sundaram, Nickel phosphide: the effect of phosphorus content on hydrogen evolution activity and corrosion resistance in acidic medium, J. Mater. Chem. A **2**, 17435 (2014).

[27] S. Qin, S. Banerjee, M. G. Sensoy, and A. M. Rappe, Unveiling the electrocatalytic hydrogen evolution reaction pathway on RuP_2 through ab initio grand canonical Monte Carlo, ACS Catal. **14**, 17253 (2024).

[28] J. F. Callejas, C. G. Read, C. W. Roske, N. S. Lewis, and R. E. Schaak, Synthesis, characterization, and properties of metal phosphide catalysts for the hydrogen-evolution reaction, Chem. Mater. **28**, 6017 (2016).

[29] Y. Abghoui and E. Skúlason, Hydrogen evolution reaction catalyzed by transition-metal nitrides, J. Phys. Chem. C **121**, 24036 (2017).

[30] M. Zeng and Y. Li, Recent advances in heterogeneous electrocatalysts for the hydrogen evolution reaction, J. Mater. Chem. A **3**, 14942 (2015).

[31] M. Kozejova, V. Latyshev, V. Kavecansky, H. You, S. Vorobiov, A. Kovalcikova, and V. Komanicky, Evaluation of hydrogen evolution reaction activity of molybdenum nitride thin films on their nitrogen content, Electrochim. Acta **315**, 9 (2019).

[32] S. Meyer, A. V. Nikiforov, I. M. Petrushina, K. Köhler, E. Christensen, J. O. Jensen, and N. J. Bjerrum, Transition metal carbides (WC, Mo2C, TaC, NbC) as potential electrocatalysts for the hydrogen evolution reaction (HER) at medium temperatures, Int. J. Hydrog. Energy **40**, 2905 (2015).

[33] M. Miao, J. Pan, T. He, Y. Yan, B. Y. Xia, and X. Wang, Molybdenum

carbide-based electrocatalysts for hydrogen evolution reaction, Chem. Eur. J. **23**, 10947 (2017).

[34] Y.-W. Cheng, J.-H. Dai, Y.-M. Zhang, and Y. Song, Two-dimensional, ordered, double transition metal carbides (MXenes): a new family of promising catalysts for the hydrogen evolution reaction, J. Phys. Chem. C **122**, 28113 (2018).

[35] C. Wan, Y. N. Regmi, and B. M. Leonard, Multiple phases of molybdenum carbide as electrocatalysts for the hydrogen evolution reaction, Angew. Chem. **126**, 6525 (2014).

[36] Y.-H. Wei, D.-S. Ma, H.-K. Yuan, X. Wang, and M.-Q. Kuang, Topological insulator path toward efficient hydrogen evolution catalysts in the Li_2Pt family, Phys. Rev. B **107**, 235414 (2023).

[37] D.-X. Liu, H. Hong, Q. Cao, D. Wang, and Y. Du, Spin Polarization of 2D Weyl Semimetal Fe2Sn Enabling High Hydrogen Evolution Reaction Activity, ChemPhysChem **25**, e202300942 (2024).

[38] L. M. Schoop, F. Pielnhofer, and B. V. Lotsch, Chemical principles of topological semimetals, Chem. Mater. **30**, 3155 (2018).

[39] M. V. Berry, Quantal phase factors accompanying adiabatic changes, Proc. R. Soc. Lond. A. Math. Phys. Sci. **392**, 45 (1984).

[40] J. Zak, Berry's phase for energy bands in solids, Phys. Rev. Lett. **62**, 2747 (1989).

[41] B. Simon, Holonomy, the Quantum Adiabatic Theorem, and Berry's Phase, Phys. Rev. Lett. **51**, 2167 (1983).

[42] M. Konig, S. Wiedmann, C. Brune, A. Roth, H. Buhmann, L. W. Molenkamp, X.-L. Qi, and S.-C. Zhang, Quantum spin Hall insulator state in HgTe quantum wells, Science **318**, 766 (2007).

[43] K. Landsteiner, Anomalous transport of Weyl fermions in Weyl semimetals, Phys. Rev. B **89**, 075124 (2014).

[44] B. Fu and S.-Q. Shen, Z_2 topological invariants and the half quantized Hall effect, Commun. Phys. **8**, 2 (2025).

[45] L. Lu, J. D. Joannopoulos, and M. Soljačić, Topological photonics, Nat. Photon. **8**, 821 (2014).

[46] W. Witczak-Krempa, M. Knap, and D. Abanin, Interacting Weyl Semimetals: Characterization via the Topological Hamiltonian and its Breakdown, Phys. Rev. Lett. **113**, 136402 (2014).

[47] D. Xiao, M.-C. Chang, and Q. Niu, Berry phase effects on electronic properties, Rev. Mod. Phys. **82**, 1959 (2010).

[48] T. Zhang, Y. Jiang, Z. Song, H. Huang, Y. He, Z. Fang, H. Weng, and C. Fang, Catalogue of topological electronic materials, Nature **566**, 475 (2019).

[49] Y. Li and Z.-A. Xu, Exploring Topological Superconductivity in Topological Materials, Adv. Quantum Technol. **2**, 1800112 (2019).

[50] M. Mandal, N. C. Drucker, P. Siriviboon, T. Nguyen, A. Boonkird, T. N.

Lamichhane, R. Okabe, A. Chotrattanapituk, and M. Li, Topological superconductors from a materials perspective, Chem. Mater. **35**, 6184 (2023).

[51] D. Hsieh, Y. Xia, D. Qian, L. Wray, J. H. Dil, F. Meier, J. Osterwalder, L. Patthey, J. G. Checkelsky, N. P. Ong, *et al.*, A tunable topological insulator in the spin helical Dirac transport regime, Nature **460**, 1101 (2009).

[52] Q. L. He, T. L. Hughes, N. P. Armitage, Y. Tokura, and K. L. Wang, Topological spintronics and magnetoelectronics, Nat. Mater. **21**, 15 (2022).

[53] L. Šmejkal, Y. Mokrousov, B. Yan, and A. H. MacDonald, Topological antiferromagnetic spintronics, Nat. Phys. **14**, 242 (2018).

[54] D. Pesin and A. H. MacDonald, Spintronics and pseudospintronics in graphene and topological insulators, Nat. Mater. **11**, 409 (2012).

[55] M. Nadeem and X. Wang, Spin gapless quantum materials and devices, Adv. Mater. **36**, 2402503 (2024).

[56] S. Raghu and F. D. M. Haldane, Analogs of quantum-Hall-effect edge states in photonic crystals, Phys. Rev. A **78**, 033834 (2008).

[57] L. Lu, J. D. Joannopoulos, and M. Soljačić, Topological states in photonic systems, Nat. Phys. **12**, 626 (2016).

[58] M. Xiao, Q. Lin, and S. Fan, Hyperbolic Weyl Point in Reciprocal Chiral Metamaterials, Phys. Rev. Lett. **117**, 057401 (2016).

[59] T. W. Lau, Y.-l. Zhang, and K. H. Fung, Zak phases of chiral photonic crystals designed via transformation optics, Phys. Rev. B **104**, 064312 (2021).

[60] N. P. Armitage, E. J. Mele, and A. Vishwanath, Weyl and Dirac semimetals in three-dimensional solids, Rev. Mod. Phys. **90**, 015001 (2018).

[61] P. Roushan, J. Seo, C. V. Parker, Y. S. Hor, D. Hsieh, D. Qian, A. Richardella, M. Z. Hasan, R. J. Cava, and A. Yazdani, Topological surface states protected from backscattering by chiral spin texture, Nature **460**, 1106 (2009).

[62] Z. Wang, Y. Chong, J. D. Joannopoulos, and M. Soljačić, Observation of unidirectional backscattering-immune topological electromagnetic states, Nature **461**, 772 (2009).

[63] C. A. Rosiek, G. Arregui, A. Vladimirova, M. Albrechtsen, B. Vosoughi Lahijani, R. E. Christiansen, and S. Stobbe, Observation of strong backscattering in valley-Hall photonic topological interface modes, Nat. Photon. **17**, 386 (2023).

[64] W. Cheng, K. Qian, N. Cheng, N. Boechler, X. Mao, and K. Sun, Backscattering-free edge states below all bands in two-dimensional auxetic media, Nat. Commun. **16**, 2373 (2025).

[65] L. Wang, Y. Yang, J. Wang, W. Liu, Y. Liu, J. Gong, G. Liu, X. Wang, Z. Cheng, and X. Zhang, Excellent catalytic performance toward the hydrogen evolution reaction in topological semimetals, EcoMat **5**, e12316 (2023).

[66] X. Zhang, L. Wang, M. Li, W. Meng, Y. Liu, X. Dai, G. Liu, Y. Gu, J. Liu, and L. Kou, Topological surface state: Universal catalytic descriptor in topological catalysis, Mater. Today **67**, 23 (2023).

[67] C. R. Rajamathi, U. Gupta, N. Kumar, H. Yang, Y. Sun, V. Süß, C. Shekhar, M. Schmidt, H. Blumtritt, P. Werner, B. Yan, S. Parkin, C. Felser, and C. N. R.

Rao, Weyl Semimetals as Hydrogen Evolution Catalysts, Adv. Mater. **29**, 1606202 (2017).

[68] R. Xie, T. Zhang, H. Weng, and G.-L. Chai, Progress, advantages, and challenges of topological material catalysts, Small Sci. **2**, 2100106 (2022).

[69] M. Samanta, H. Tan, S. Laha, H. A. Vignolo-González, L. Grunenberg, S. Bette, V. Duppel, P. Schützendübe, A. Gouder, B. Yan, *et al.*, The Weyl Semimetals MIrTe4 (M= Nb, Ta) as Efficient Catalysts for Dye-Sensitized Hydrogen Evolution, Adv. Energy Mater. **13**, 2300503 (2023).

[70] W. Liu, X. Zhang, W. Meng, Y. Liu, X. Dai, and G. Liu, Theoretical realization of hybrid Weyl state and associated high catalytic performance for hydrogen evolution in NiSi, iScience **25** (2022).

[71] G. Li, C. Fu, W. Shi, L. Jiao, J. Wu, Q. Yang, R. Saha, M. E. Kamminga, A. K. Srivastava, E. Liu, *et al.*, Dirac nodal arc semimetal PtSn4: an ideal platform for understanding surface properties and catalysis for hydrogen evolution, Angew. Chem. **131**, 13241 (2019).

[72] G. Li, Y. Sun, J. Rao, J. Wu, A. Kumar, Q. N. Xu, C. Fu, E. Liu, G. R. Blake, P. Werner, *et al.*, Carbon-tailored semimetal MoP as an efficient hydrogen evolution electrocatalyst in both alkaline and acid media, Adv. Energy Mater. **8**, 1801258 (2018).

[73] Q. Yang, C. Le, G. Li, T. Heine, C. Felser, and Y. Sun, Enhancement of basal plane electrocatalytic hydrogen evolution activity via joint utilization of trivial and non-trivial surface states, Appl. Mater. Today **22**, 100921 (2021).

[74] J. Li, H. Ma, Q. Xie, S. Feng, S. Ullah, R. Li, J. Dong, D. Li, Y. Li, and X.-Q. Chen, Topological quantum catalyst: Dirac nodal line states and a potential electrocatalyst of hydrogen evolution in the TiSi family, Sci. China Mater. **61**, 23 (2018).

[75] X. Wang, L. Wang, C. Xie, Y. Liu, G. Liu, W. Wang, Z. Cheng, G. Zhang, and X. Zhang, Double dual-nodal-line semimetals with large surface density of states: Topological quantum catalysts for the hydrogen-evolution reaction, Phys. Rev. Appl. **20**, 044042 (2023).

[76] Z. Li, Z. He, L. Wang, W. Meng, X. Dai, G. Liu, Y. Liu, and X. Zhang, High-performance hydrogen evolution reaction in quadratic nodal line semimetal Na_2CdSn, iScience **27** (2024).

[77] L. Wang, M. Zhao, J. Wang, Y. Liu, G. Liu, X. Wang, G. Zhang, and X. Zhang, High-performance hydrogen evolution reaction catalysts in two-dimensional nodal line semimetals, ACS Appl. Mater. Interfaces **15**, 51225 (2023).

[78] E. Santos, A. Lundin, K. Pötting, P. Quaino, and W. Schmickler, Model for the electrocatalysis of hydrogen evolution, Phys. Rev. B **79**, 235436 (2009).

[79] E. Skúlason, G. S. Karlberg, J. Rossmeisl, T. Bligaard, J. Greeley, H. Jónsson, and J. K. Nørskov, Density functional theory calculations for the hydrogen evolution reaction in an electrochemical double layer on the Pt (111) electrode, Phys. Chem. Chem. Phys. **9**, 3241 (2007).

[80] J. K. Nørskov, T. Bligaard, A. Logadottir, J. R. Kitchin, J. G. Chen, S. Pandelov, and U. Stimming, Trends in the Exchange Current for Hydrogen Evolution, J. Electrochem. Soc. **152**, J23 (2005).

[81] S. Bhattacharjee, U. V. Waghmare, and S.-C. Lee, An improved d-band model of the catalytic activity of magnetic transition metal surfaces, Sci. Rep. **6**, 35916 (2016).

[82] H. Xin, A. Vojvodic, J. Voss, J. K. Nørskov, and F. Abild-Pedersen, Effects of *d*-band shape on the surface reactivity of transition-metal alloys, Phys. Rev. B **89**, 115114 (2014).

[83] S. Wang and J. Jiang, Interpretable catalysis models using machine learning with spectroscopic descriptors, ACS Catal. **13**, 7428 (2023).

[84] B. Wang and F. Zhang, Main descriptors to correlate structures with the performances of electrocatalysts, Angew. Chem. **61**, e202111026 (2022).

[85] G. Cao, S. Yang, J.-C. Ren, and W. Liu, Electronic descriptors for designing high-entropy alloy electrocatalysts by leveraging local chemical environments, Nat. Commun. **16**, 1251 (2025).

[86] L.-H. Mou, T. Han, P. E. Smith, E. Sharman, and J. Jiang, Machine learning descriptors for data-driven catalysis study, Adv. Sci. **10**, 2301020 (2023).

[87] L. Qi, W. Gao, and Q. Jiang, Effective descriptor for designing high-performance catalysts for the hydrogen evolution reaction, J. Phys. Chem. C **124**, 23134 (2020).

[88] D. M. NEWNS, Self-Consistent Model of Hydrogen Chemisorption, Phys. Rev. **178**, 1123 (1969).

[89] H. Weyl, Gravitation and the electron, Proc. Natl. Acad. Sci. U.S.A. **15**, 323 (1929).

[90] S.-M. Huang, S.-Y. Xu, I. Belopolski, C.-C. Lee, G. Chang, B. Wang, N. Alidoust, G. Bian, M. Neupane, C. Zhang, *et al.*, A Weyl Fermion semimetal with surface Fermi arcs in the transition metal monopnictide TaAs class, Nat. Commun. **6**, 7373 (2015).

[91] S.-Y. Xu, I. Belopolski, N. Alidoust, M. Neupane, G. Bian, C. Zhang, R. Sankar, G. Chang, Z. Yuan, C.-C. Lee, *et al.*, Discovery of a Weyl fermion semimetal and topological Fermi arcs, Science **349**, 613 (2015).

[92] S.-Y. Xu, I. Belopolski, D. S. Sanchez, C. Zhang, G. Chang, C. Guo, G. Bian, Z. Yuan, H. Lu, T.-R. Chang, *et al.*, Experimental discovery of a topological Weyl semimetal state in TaP, Sci. Adv. **1**, e1501092 (2015).

[93] P. Hohenberg and W. Kohn, Inhomogeneous Electron Gas, Phys. Rev. **136**, B864 (1964).

[94] W. Kohn and L. J. Sham, Self-Consistent Equations Including Exchange and Correlation Effects, Phys. Rev. **140**, A1133 (1965).

[95] D. R. Hamann, M. Schlüter, and C. Chiang, Norm-Conserving Pseudopotentials, Phys. Rev. Lett. **43**, 1494 (1979).

[96] D. Vanderbilt, Soft self-consistent pseudopotentials in a generalized eigenvalue formalism, Phys. Rev. B **41**, 7892 (1990).

[97] G. Kresse and D. Joubert, From ultrasoft pseudopotentials to the projector augmented-wave method, Phys. Rev. B **59**, 1758 (1999).

[98] J. P. Perdew, K. Burke, and M. Ernzerhof, Generalized Gradient Approximation Made Simple, Phys. Rev. Lett. **77**, 3865 (1996).

[99] W. P. Su, J. R. Schrieffer, and A. J. Heeger, Solitons in Polyacetylene, Phys. Rev. Lett. **42**, 1698 (1979).

[100] G. Pizzi, V. Vitale, R. Arita, S. Blügel, F. Freimuth, G. Géranton, M. Gibertini, D. Gresch, C. Johnson, T. Koretsune, J. Ibañez-Azpiroz, H. Lee, J.-M. Lihm, D. Marchand, A. Marrazzo, Y. Mokrousov, J. I. Mustafa, Y. Nohara, Y. Nomura, L. Paulatto, S. Poncé, T. Ponweiser, J. Qiao, F. Thöle, S. S. Tsirkin, M. Wierzbowska, N. Marzari, D. Vanderbilt, I. Souza, A. A. Mostofi, and J. R. Yates, Wannier90 as a community code: new features and applications, J. Phys. Condens. Matter **32**, 165902 (2020).

[101] Q. Wu, S. Zhang, H.-F. Song, M. Troyer, and A. A. Soluyanov, Wanniertools: An open-source software package for novel topological materials, Comput. Phys. Commun. **224**, 405 (2018).

[102] J. J. Sakurai and J. Napolitano, *Modern Quantum Mechanics*, 3rd ed. (Cambridge University Press, 2020).